Electronic Theses and Dissertations

2009

Droplet Flows In Microchannels Using Lattice Boltzmann Method

Amit Gupta
University of Central Florida

DROPLET FLOWS IN MICROCHANNELS USING LATTICE BOLTZMANN METHOD

by

AMIT GUPTA
B.Tech. Indian Institute of Technology Delhi, 2004
M.S. University of Central Florida, Orlando 2007

A dissertation submitted in partial fulfillment of the requirements
for the degree of Doctor of Philosophy
in the Department of Mechanical, Materials and Aerospace Engineering
in the College of Engineering and Computer Science
at the University of Central Florida
Orlando, Florida

Spring Term
2009

Major Professor: Ranganathan Kumar

ABSTRACT

Microelectromechanical systems (MEMS) have widespread applications in medical, electronical and mechanical devices. These devices are characterized by the smallest dimension which is atleast one micrometer and utmost one millimeter. Rapid progress in the manufacture and utilization of these microdevices has been achieved in the last decade. Current manufacturing techniques of such devices and channels include surface silicon micromachining; bulk silicon micromachining; lithography; electrodeposition and plastic molding; and electrodischarge machining (EDM). In recent years, electrostatic, magnetic, electromagnetic and thermal actuators, valves, gears and diaphragms of dimensions of hundred microns or less have been fabricated successfully. Sensors have been manufactured that can detect pressure, temperature, flow rate and chemical composition in such channels. Physical effects such as electrokinetics, pressure gradient and capillarity become prominent for channels where the length scales are of the order of hundreds of micrometers. Also, at such length scales, the application of conventional numerical techniques that use macroscale equations to describe the phenomenon is questionable as the validity of the no-slip boundary condition depends on the ratio of the mean free path of the fluid molecules to the characteristic dimension of the problem (called the Knudsen number). Macroscale equations can only be applied if Knudsen number is of the order of 10^{-3} or less.

In recent years, the lattice Boltzmann method (LBM) has emerged as a powerful tool that has replaced conventional macroscopic techniques like Computational Fluid Dynamics (CFD) in many applications involving complex fluid flow. The LBM starts from meso- and microscopic

Boltzmann's kinetic equation and can be used to determine macroscopic fluid dynamics. The origins of LBM can be drawn back to lattice gas cellular automata (LGCA) which lacked Galilean invariance and created statistical noise in the system. LBM on the other hand possesses none of these drawbacks of LGCA, and is easy to implement in complex geometries and can be used to study detailed microscopic flow behavior in complex fluids/fluid mixtures. Nor does it have any of the drawbacks of the Navier-Stokes solvers of implementing the slip boundary condition on the surface of a solid. It has also been found to be computationally fast and an alternative to Navier-Stokes equations.

In this study, LBM is used to simulate two-fluid flows such as bubbles rising in a liquid, droplet impingement on a dry surface and creation of emulsions in microchannels. Simulation of disperse flows in a continuous medium using simple boundary condition methods lays the foundation of conducting complex simulations for the formation of droplets past a T-junction microchannel in the framework of this statistical method. Simulations in a T-junction illustrate the effect of the channel geometry, the viscosity of the liquids and the flow rates on the mechanism, volume and frequency of formation of these micron-sized droplets. Based on the interplay of viscous and surface tension forces, different shapes and sizes of droplets were found to form. The range of Capillary numbers simulated lies between $0.001 \leq Ca \leq 1.0$. Different flow regimes are observed that can be described based on the Capillary number of the flow. A flow regime map that lists where droplet or parallel flow may occur has been created based on the flow rate ratio and Capillary number for a purely laminar flow in the microchannel.

Dedicated to my parents, Uma and Banshi Dhar.

ACKNOWLEDGEMENTS

This work is an effort that would not be possible without the supervision and support of my teacher and guide Dr. Ranganathan Kumar. Words cannot express my gratitude and pleasure of having worked with him for the past four and a half years at UCF.

I would also like to thank the members on my dissertation committee, Dr. Louis Chow, Dr. Jayanta Kapat, Dr. Hyoung Cho and Dr. Bhimsen Shivamoggi, for reading and providing valuable comments and suggestions pertaining to my dissertation.

My appreciation extends to my past and present group members, particularly Parveen Sachdeva, Xin Gu, Navid Amini, Denitsa Milanova, Ehsan Tafti, Xuan Wu, Sohel Murshed, with whom I have had several mind stimulating discussions.

I will always treasure the good times shared with Piyush Nawathe, Swapnil Chogle, Nezamuddin, Albinder Dhindsa, Vinayak Dixit and Abhishek Das. They have wholeheartedly helped me during my stay in Orlando.

I am grateful to my parents Uma and Banshi Dhar, who have always provided me with the inspiration to pursue excellence and the road to hard work. They have led by example, and have been instrumental in motivating me to do my best. Nothing would have been possible without the support given by my brother Puneet, especially through his expertise in programming languages.

Lastly, I would like to thank my wife, Nanditha, for her belief in my ability and egging me on whenever I hit stagnation. This dissertation is a reflection the hard work she put in the last year, and I owe it to her love, dedication and selflessness.

TABLE OF CONTENTS

LIST OF FIGURES

LIST OF TABLES

LIST OF ABBREVIATIONS

a   acceleration

a index for velocity-space discretization

A surface tension parameter

c lattice unit length

Ca   Capillary number

c_s speed of sound

C_D drag coefficient

d diameter of the bubble

D diameter of the spherical cap

e_i   lattice speed of particles moving in direction i

Eo Eotvos number

f particle distribution function

F   force

g   acceleration due to gravity

g_{ij} interaction strength between components i and j

G Green's function

m molecular mass

M Mach number

Mo Morton number

n   normal vector

Oh	Ohnesorge number
p	pressure
p	momentum
q	color flux
r	radius of the bubble
R	radius of curvature
Re	Reynolds number
s	curvature of the stagnation point
S	number of phases/scale factor
t	time
u	velocity vector
U	velocity in the rise direction/average velocity
V	interaction potential
w	weight along the link 'i'
We	Weber number
β	anti-diffusion parameter
θ	polar angle
κ	curvature
λ	viscosity ratio
μ	dynamic viscosity
ξ	spreading factor
ρ	density/phase-field

σ	surface tension/phase index
ν	kinematic viscosity
τ	relaxation time
Γ	height to channel width ratio
Λ	dispersed channel width to continuous channel width
Φ	potential
Δ	fractional distance
Ω	collision operator
$\delta_{\alpha\beta}$	Kronecker delta
Ψ	effective mass function
ε	permittivity
b	bubble
B	blue
e	effective
ext	external
i	index
int	internal
L	liquid
R	red
sph	sphere
$*$	non-dimensional quantities
eq	equilibrium

CHAPTER ONE: INTRODUCTION

In his lecture titled "There is Plenty of Room at the Bottom" delivered in 1959, Richard Feynman postulated the fabrication of micro-devices that 'might not be of any use for mankind but would be fun to create and work with'. Not many in that room would have realized that less than half a century later, miniaturization would be the order of the day. Microelectromechanical systems (MEMS as they are commonly referred to), are devices that are characterized by the smallest dimension which is atleast one micrometer and utmost one millimeter. Rapid progress in the manufacture and utilization of these microdevices has lead to the widespread use of these devices for both scientific and the industrial community in a variety of applications. These devices are currently being manufactured using techniques such as surface silicon micromachining, bulk silicon micromachining, lithography, electrodeposition and plastic molding, and electrodischarge machining (EDM). In recent years, electrostatic, magnetic, electromagnetic and thermal actuators, valves, gears and diaphragms of dimensions of hundred microns or less have been fabricated successfully. Sensors have been manufactured that can detect pressure, temperature, flow rate and chemical composition in micron-sized channels.

Many of these microdevices, for instance microducts, micronozzles, micropumps, and microturbines, involve or operate on the basis of fluid(s) flowing through narrow crevices. Depending on the application, these devices can either have liquid or gas as the working fluid. According to Kandlikar (2002), who has classified thin channels based on their hydraulic diameters, microchannels (10 μm to 200 μm) are employed in inkjet printers and many Micro-

Elecro-Mechanical Systems (MEMS); minichannels (200 μm to 3 mm) in compact plate-fin evaporators; and conventional channels (>3 mm) in steam tube boilers, evaporator tubes, etc. This classification is evolving with rapid advances made in this field.

In the past, flows of gas-liquid or liquid-liquid mixtures have been studied both experimentally and numerically for many macroscopic systems. For instance, in two-fluid mixtures, the commonly used parameters that characterize the flow are the Reynolds number ($\text{Re} = U_b d_e / \upsilon$), the Eotvos ($Eo = g \Delta \rho d_e^2 / \sigma$), Morton number ($Mo = g \rho_L^2 \Delta \rho \upsilon^4 / \sigma^3$), and Weber number ($We = \text{Re}^2 Mo^{1/2} / Eo^{1/2}$). As the size of the physical system changes, the set comprising the parameters is subject to change, often in a dramatic way (Trimmer (1989); Madou (1997)). Understanding scaling laws guides our understanding of how to design micro-electro-mechanical systems. If 'S' is the scale factor that denotes the scaling down of the dimensions of any mechanical drawing of an object that is to be built on a scale much smaller than what is apparent, then according to Trimmer and Stroud (2002), some of the important forces scale down as follows.

$$F = \begin{bmatrix} S^1 \\ S^2 \\ S^3 \\ S^4 \end{bmatrix} = \begin{bmatrix} \text{Surface tension} \\ \text{Electrostatic, Pressure, Biological, Magnetic } (J = S^{-1}) \\ \text{Magnetic } (J = S^{-0.5}) \\ \text{Gravitational, Magnetic } (J = S^0) \end{bmatrix} \qquad (1.1)$$

It is quite apparent that the surface tension forces become more important than hydrodynamic pressure and gravitational forces as the physical scale of a device is lowered. Thus, the solution of these non-linear equations to analyze flows in microscale geometries could lead to erroneous interpretation of real physical phenomenon if surface tension is ignored as is frequently done while solving the Navier-Stokes equations. According to a recent review article regarding multiphase flows in microchannels (Stone et al (2004)):

> *When discussing multiphase flows in microdevices there are likewise a myriad of questions that arise in even simple configurations. For example, it is frequently of interest to determine the size of droplets of the dispersed phase or the speed at which the dispersed phase moves relative to the continuous phase. Also, when two different phases are injected as adjacent streams in one channel, the flow can be stable but, alternatively, one phase can preferentially wet the boundaries and encapsulate the second fluid, either as a continuous stream or discrete drops. Two phase flows in microdevices can also be used to focus columnar liquid samples for flow cytometry.*

The above quoted paragraph indicates the need to study microscopic physics of flows in microchannels because of the length and breadth of applications that are encapsulated in the realm of MEMS devices at present and future applications. As an example, if we look at multiphase flows in microchannels, it has been observed that nucleating bubbles grow in size and quickly span the width of the channel, due to which the slug and churn-turbulent regimes are dominant in microchannels. This increases the pressure gradient and the heat transfer coefficient

3

of these thin channels compared to large channels. The existing correlations in literature are applicable for macroscopic channels, and not for thin channels. These correlations could have been proposed for situations where the gravity and vapor shear forces play a dominant role. However, in thin geometries, the surface tension effects are significant. It is still not clear whether there is a critical channel size at which the surface tension effect begins to dominate. Only a detailed numerical study, with an appropriately chosen numerical technique, could lead to possible explanations of fluid behavior that is so unfamiliar to that observed in macroscopic channels.

1.1 Numerical Techniques

One of the other issues with microchannels is the geometric shape. It is known that flow in rectangular channels is more complex and less well understood than in circular geometries. The behavior of bubbles and slugs in a confined space between two walls has been observed to be different from that in a circular geometry. Thus, the number of flow and geometric variables, for instance, the shape and flow passage, system pressure, mass flux and fluid properties, increases and it becomes even more important to focus on the fundamental understanding of two-phase flow behavior in thin geometries and rely less on empirical correlations.

Figure 1 shows the currently used fluid modeling techniques commonly used by researchers in the past few decades. In multiphase flows, the standard method has been to use continuum based techniques; either the fluid-mixture or the two-fluid model. Each fluid is modeled by a modified Navier-Stokes (NS) equation, with extra source terms accounting for interfacial effects and

forces. But these models ignore the molecular nature of fluid-fluid interactions that become prominent at the length scales of microchannels, and it is difficult to handle the interface in continuum models as they can fail to capture an interface that rapidly evolves with time. Molecular based models, on the other hand, work with a bunch of individual fluid atoms/molecules and are used to determine their position, velocity and temperature at all times, and the macroscopic properties can then be derived by a suitable statistical averaging technique (for example, the Green-Kubo method to determine the thermal conductivity). This way of simulating fluid-fluid mixtures can be computationally expensive, especially if a microchannel is to be filled up with the molecules whose size is of the order of 1 Å ($=10^{-10}$ m). Statistical methods of modeling these fluids, on the other hand, deal with the probability density function at a given location as the sole variable. The lattice Boltzmann method (LBM) is one such statistical method that is widely used by researchers lately to study two-fluid mixtures. For dilute flows near equilibrium, these statistical methods can be shown to lead to the familiar Navier-Stokes equations using the Chapman-Enskog expansion.

Table 1 below lists some of the methods used in modeling multiphase flows with the achievable spatial resolution as given by Tomiyama (1998). For flows in microchannels, the conventional no-slip boundary condition does not remain valid any longer if the Knudsen number (Kn) is greater than 0.001. The Knudsen number is the ratio of the mean free path of the atoms/molecules of the gas/liquid and the characteristic length of the flow domain. The continuum equations (Navier-Stokes, Euler) are found to be valid as long as Kn<0.1, albeit with modified boundary conditions. As we move to sub-micrometer dimensions the assumptions used

in the continuum models do not hold, thereby inhibiting the applicability of such techniques to model the systems with sub-micrometer length scales. At this scale, Monte Carlo (MC) method or lattice Boltzmann Method offer advantages in terms of computationally cheaper and reliable forms of numerical techniques that can be used to accurately simulate the fluid flow and heat transfer behavior. As we move to nanometer length scales, MC and LBM can not be used to simulate the physics of the atomic scale system. At these scales, there is a need to use a numerical technique which can deal with individual atoms. Molecular dynamics (MD) based simulation is the appropriate method to simulate such atomic scale phenomenon. As the length scale decreases further and reaches levels where we deal with electrons and nuclei, Quantum Chemistry (QC) based methods, for example, Quantum Molecular Dynamics or Density Functional Theory (DFT), should be used to model the systems. Figure 2 depicts these length scales and the regime where each of the above-discussed simulation techniques is used.

According to Tomiyama (1998), applicability of LBM to practical problems is considered to be low. This has changed over the past decade with the advent of new models that can handle complex multiphase behavior like phase separation and modeling of liquid droplets and bubbles in the presence of another medium. One of the many interesting advantages of LBM over other conventional multiphase methods, like the level-set and volume-of-fluid methods, is that the interface is no longer a mathematical boundary in the former, nor does it need to be tracked unlike these latter techniques. Rather, it is a post-processed quantity that can be detected by monitoring the variation in fluid properties.

Table 1 : Numerical Methods for Computational Bubble Dynamics after Tomiyama (1998)

Spatial Resolution	Method	Fundamental Equations	Applicability to practical problems
Low ($\Delta x \gg d$)	Averaging methods (homogenous, drift-flux, two fluid models)	Averaged field equation + constitutive equation	high
Intermediate	Bubble tracking method (one-way, two-way methods)	Equation of bubble motion + constitutive equations	Intermediate
High ($\Delta x < d$)	Interface tracking method (front-tracking, volume tracking, level set).	Navier-Stokes equation + Surface tension	Low
High ($\Delta x \ll d$)	Microscopic method (Lattice Gas, lattice Boltzmann method).	Translation and Collision and Pseudo molecules	Low

Δx: cell size, d: Bubble diameter.
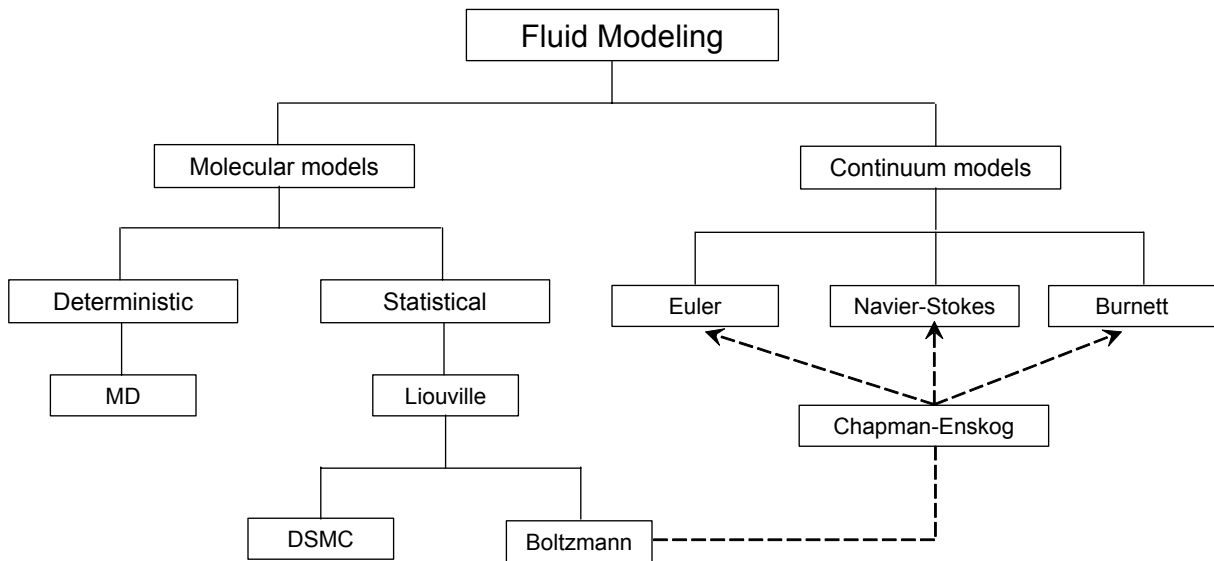
Figure 1: Molecular and continuum flow models (from Gad-el-Hak (1999)).
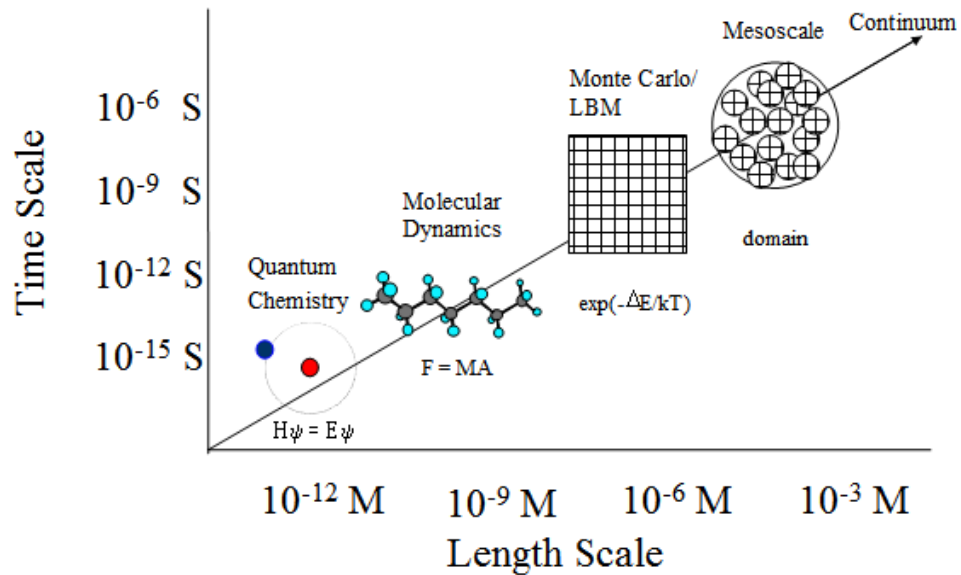
Figure 2: An overview of the different simulation techniques with the length and time-scales for which they are applied (after Smith (1999)).

1.2 Motivation

In the literature, many applications can be found that involve the formation of droplets or bubbles using dissimilar fluids in a novel microchannel arrangement. The three primary methods of separating drops at regular and periodic intervals are described by Christopher and Anna (2007). These are droplet formation using (i) co-flowing streams, (ii) using cross-flowing streams, and (iii) using elongational stresses. Droplets produced through any of these methods can be collected or utilized in situ for applications such as drug delivery, microanalysis, tumor destruction, as ultrasound agents, in chemical reactions at the micron level, protein crystallization, DNA analysis and in synthesis of nanoparticles.

In addition, many applications can be thought of where microreactors or microlaboratories could include immiscible liquid-liquid and gas-liquid systems. Some of these include miniature distillation units, bubble generators, multiphase separation units and chemical processes. Gas bubbles could be used as spacers for samples in a channel or to act as a piston to produce pressure-driven flow on top of the electrokinetic flow. Flow valves and pumps that employ air-bubbles, like those in the ink reservoirs of ink-jet printers are already being tested for microchannels. Drug-delivery and diagnostic devices including colloids, molecules and biological cells are also active areas of research (see Chang (2002)).

Buoyed by the tremendous potential microfluidic droplet generators have exhibited in the open literature, and the lack of theoretical treatment for an accurate control and prediction of the flow regimes possible in such geometries, it is proposed to develop a numerical framework which

would shed light and enhance our understanding of the fluid mechanics at the micron level in such devices.

1.3 Proposed Problem Description

In the present work, three-dimensional simulation of fluid flow consisting of two dissimilar liquids through a T-junction microchannel has been selected due to the non-trivial nature of the flow physics that emanates from this complex geometry. The two fluid streams are laminar in nature, and the dynamic interface is handled through a three-dimensional numerical model that can model the stress boundary condition and satisfies the continuity of velocity for the incompressible fluids. The two fluids are modeled through an incompressible form of the lattice Boltzmann formulation (He and Luo (1997)), that enables an accurate prescription of the pressure boundary conditions at the inlet and exit of the microchannel. Due to the length scales involved in the problem, that range from 50 microns to 300 microns, a continuum description of the fluids is found to be valid. This enables application of the (i) no-slip boundary condition, and (ii) a continuum model of wetting (Dupin et al (2006)) at the walls of the channel. The rest of the thesis is divided as follows. In Chapter 2, an overview of the available literature on formation of droplets and emulsions using the three microfluidic arrangements is presented. In Chapter 3, a foundation for LBM is laid out, followed by description of exisiting theoretical models on handling multiphase flows in LBM. The numerical methodology adopted to simulate three-dimensional fluid two-phase flows is outlined. This is followed by Chapter 4 in which LBM is tested and shown to be accurate in predicting simple single-phase flows. Results are presented for validation of some of the common benchmark problems that have been solved using the

simulation technique. Chapter 5 discusses the method of simulating two-phase flows, such as single and multiple bubbles rising due to buoyancy in a quiescent fluid and droplet impingement behavior on a smooth dry surface, followed by results and key findings using a pseudo-potential variant of the multiphase model in the framework of LBM. In Chapter 6, results are compiled and presented for simulation of droplet formation in a T-junction microfluidic device for a range of Capillary numbers, flow rate ratios, different viscosities and varying channel geometries. Chapter 7 outlines the conclusions and key findings of this work, which is followed by a brief summary and ideas for future work on the current topic in Chapter 8.

CHAPTER TWO: LITERATURE REVIEW

2.1 Introduction

In this chapter, an overview of the existing literature, both experimental and theoretical, on creation of droplets and dispersions by suitable selection of microchannel arrangement is presented. Three basic ideas pertaining to droplet generation are discussed. These are: (a) co-flowing fluids, (b) formation at a T-junction, and (c) formation due to elongational stresses. Through suitable arguments, the importance of pursuing a theoretical study to understand the fundamental behavior of the interfacial phenomenon responsible for creation of micron-sized droplets is established.

2.2 Experimental Investigations in Microchannels

Many applications are found that involve multiphase transport through thin capillaries and microchannels. For instance, miniature evaporative and distillation units and bubble generators, flow cytometers and emulsions all use transport of two dissimilar fluids through a microchannel. For such cases, a large pressure drop is required to drive the fluid mixture through a length of the channel.

One of the important and upcoming areas of research in microfluidics is mixing and dispersion of reagents. These reagents can be large or small molecules, particles, and drops or bubbles. One such application requires control of axial dispersion of plugs of a solute which is to be

transported to a detector, as shown in figure 3. At least three applications of such small droplets (or bubbles) can be identified (Stone et al (2004)) and are given as follows:

1) drops as actuators for pumping a primary flow or driving mixing flows,

2) drops as individual 'chemical reactors', and

3) emulsion formation with a controlled drop size and size distribution.

Many different forms of microdevices have been designed, fabricated and tested for the formation of flow dispersions with emphasis mostly on creating a dispersed phase in a continuous medium that is transported downstream and can be received and processed at some detector at regular intervals of time. There is a need to isolate discrete nanoliter droplets in many applications, especially those that concern biomedical and drug manufacturing industries. A system that can control the size of these droplets at a minimum work, and at the same time maximize the production rate is very much needed.

Researchers have shown various ways of using internal flows in drops to accomplish 'chemical reactions' in droplets of nanoliter sizes. Kataoka and Troian (1999) demonstrate a simple technique, and an alternative to the use of electric field to achieve bubble/droplet movement, that utilizes temperature gradients to direct microscopic flow on a selectively patterned surface. This surface consisted of alternating stripes of bare and coated Silica. The liquid was manipulated by applying a shear stress at the air-liquid interface and a variable surface energy pattern at the liquid-solid interface. The authors showed that this novel idea can be used to direct microscale flow along prescribed lanes. Sugiura et al (2001), in their method of droplet formation, passed

13

the dispersed phase through a channel, then inflated it on a terrace in a disk-like shape, and subsequently the droplets that were formed were cut off spontaneously on the terrace into spherical droplets by interfacial tension. Ward and Humsy (2001) demonstrate the use of AC electric fields to enhance the mixing inside droplets in a microchannel. These electric fields produce Marangoni stresses that drive motion in such geometries. Song et al (2003) show the use of a curved channel to enhance the mixing inside drops that is used to generate time dependent internal flows. Their system could be used to transport solutions with rapid mixing and no dispersions. Since pair of co- and counter-rotating vortices both generate chaos in periodic time dependent flows, they induced such a flow in plugs by replacing the conventional straight channel with a winding channel. Work has also been carried out in the fabrication of nanojets that can deliver a stream or discrete droplets depending upon the driving pressure of the dispersed phase. Naik et al (2007) demonstrate the use of a microfluidic system for the generation and characterization of liquid and gaseous micro- and nanojets. Their approach allows for important three-dimensional features of nozzle, channel and fluidic reservoir that are defined by design and do not depend on fabrication constraints, thereby a fully developed flow could be achieved.

2.2.1 Formation of Droplets in a Co-flowing Geometry

In one of the earliest reported experiments on a droplet formation of this kind, Umbanhowar et al (2000) show the formation of highly monodisperse droplets of the dispersed phase in a surfactant-laden continuous phase via a converging capillary. Droplet formation was described to be the result of a competing nature of the drag force, experienced by the expanding dispersed

14

phase due to the co-flowing outer liquid, exceeding the interfacial force that holds the droplet on the tip of the capillary. Cramer et al (2004) have demonstrated the use of a co-flowing arrangement to form droplets at the tip of the dispersed phase channel. They have outlined the two forms of flow patterns that emanate for such geometry. These are dripping and jetting flows, as shown in figure 4. Their experiments were focused on studying the dripping mode of droplet formation by varying the flow rates, viscosities and interfacial tension in the context of the droplet sizes and possible formation of satellite droplets.

Guillot et al (2007) have studied the stability of a jet in a confined two-fluid flow in a cylindrical capillary. The droplet regimes that they observe can be classified in terms of the shape and size of the droplet formed. These are (a) droplets smaller than the capillary, (b) droplets in the form of plugs, (c) wavelike jets, (d) straight jets and (e) thin jets that break into droplets. They obtained a regime map in which for a fixed flow rate of the external liquid, when the inner fluid flow rate was increased, the flow regime changed progressively from (a) to (d). At very high flow rates of the external flow rate, as the internal fluid flow rate was increased, wavelike jets were followed by formation of thin jets that formed droplets at a fixed location downstream of the channel. The authors found that this data was found to agree well with a linear stability analysis based on lubrication theory considerations.
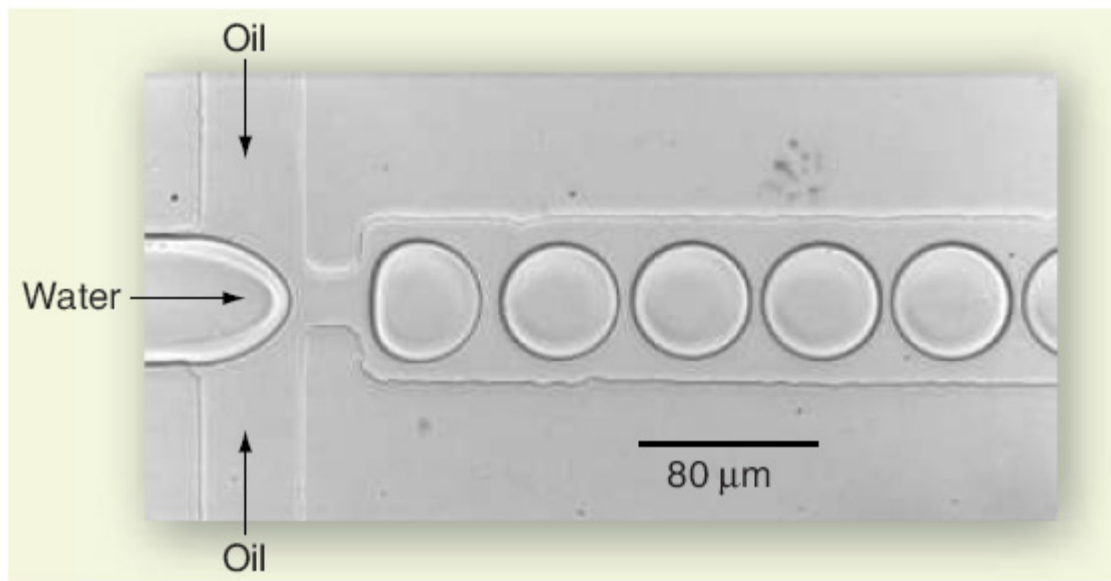
Figure 3: An illustration of formation of water droplets in oil in a microchannel (after Joanicot and Ajdari (2005)).

(a)   (b)
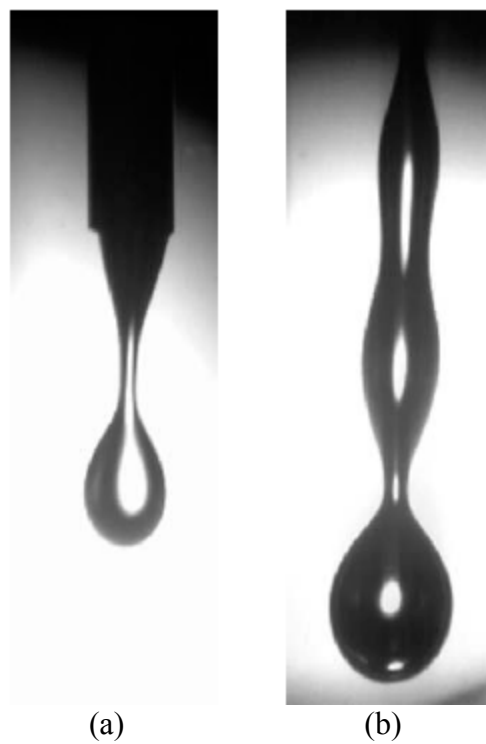
Figure 4: Drop formation in a co-flowing arrangement. The two modes of (a) dripping and (b) jetting are shown (from Cramer et al (2004)).

2.2.2 Formation of Droplets in a T-junction Microchannel

In one of the earliest studies carried out on a microfluidic T-junction, Thorsen et al (2001) demonstrate how such a device could be designed to produce reverse micelles that could generate ordered or complex patterns based on the flow rates of the two liquids. They mention that since most microfluidic devices operate at low Reynolds number conditions, the Navier-Stokes equations for fluid flows become linear and the observed flow is laminar. Through their pioneering work, it was demonstrated how the interaction between two immiscible fluids can be used to introduce non-linearity and instability in a microfluidic device. In their study, emulsions were formed by colliding an oil stream and a water stream at a T-shaped junction. Droplet formation was achieved by high shear forces that are generated at the leading edge of the water side of the channel that is perpendicular to the oil flow (see figure 5). This shear causes the formation of picoliter scale droplets and creating a nonlinear system because of the boundary. The ensuing instability drove the formation of the water drops which results from the imbalance between the surface tension and shear forces.

Link et al (2004), on the other hand, demonstrate two methods for passively breaking larger drops into precisely controlled daughter drops under pressure-driven flow in different configurations. They chose a T-junction, and flow past isolated objects to break up larger drops into smaller drops at high dispersed phase volume fractions. Their method of breakup with the T-junction configuration works on exploiting the extensional flow in the neighborhood of the stagnation point of the junction to break bigger drops into smaller ones. They found out that for

17

any ratio of the drop length to the channel width, there is a critical flow rate above which the drop will always break into two daughter droplets (see figure 6). This kind of a passive breakup technique could also be used to facilitate asymmetric breakup of droplets by adjusting the lengths of the side channels. An alternative breakup configuration was also fabricated in their work which uses the principle of flow past an obstacle to effect "controllable" changes in drop size (figure 7). Huh et al (2002) have described a disposable flow cytometer that use a two-phase air-liquid microfluidic system to produce highly focused high speed liquid sample stream of particles and cells. By controlling the flow rates and suitable surface chemistries on the channel walls, thin and partially bounded sample streams of thickness ranging in 15-100 microns were produced and found applicable for rapid cell analysis. Okushima et al (2004) have reported a method for preparation of double emulsions using a two-step T-junction arrangement, as shown in figure 8. They show that emulsions such as water-in-oil-in-water can be formed by changing the flow conditions at the points of formation and carefully controlling the breakup rates at the two T-junctions.

Cristobal et al (2006) have experimentally demonstrated the design of a microfluidic device that can allow for equal and periodic distribution of droplets as they are collected at the two outlets of a T-junction. Tice et al (2004) have shown that the formation of droplets and plugs can be accomplished in a T-junction microfluidic device using both viscous and non-viscous aqueous solutions. In their experiments, plugs were found to form dominantly for Ca<0.01, and for higher Capillary numbers but at low values of the flow rate ratios. They also show that mixing in droplets can be enhanced by combining viscous and non-viscous reagents and moving them

18

through straight microchannels. Xu et al (2006a) have shown the formation of air microbubbles surrounded by aqueous phase that was accomplished with less than 2% polydispersity in sizes of the bubbles produced. They show that increasing the continuous phase viscosity at a fixed flow rate of the dispersed and continuous fluids results in lower volumes of the droplets formed at the T-junction, a result that they believe is consistent with other experimental observations. In a separate study, Xu et al (2006b) showed that as the continuous flow rate is increased at a constant flow rate of the dispersed phase, the volume of the droplets formed decreases rapidly. These recorded droplet volumes were also found to be a function of the viscosity of the continuous phase. At the same fixed value of the dispersed fluid flow rate, it was observed that the volume of the droplets decreases as the viscosity of the continuous fluid increased.

Engl et al (2005) report that a train of confined droplets flowing through a T-junction channel can be distributed or collected into the shortest channel for low Capillary number flows. They have attributed this behavior to a 'hydrodynamic feedback' that occurs as the droplets approach different outlets. One of the more comprehensive studies on the droplet formation process for T-junction microfluidic channels has been carried out by Garstecki et al (2006). In this work, droplet formation has been studied for low Capillary number flows and for channels where $\Lambda = w_d / w_c$ lies between 0.25 and 1. According to their experimental data, the lengths of the drops formed at low Capillary numbers and for the range of channel widths given earlier can be written as

$$L / w_c = 1 + \alpha Q \tag{2.1}$$

where

$$\alpha = d / w_c \tag{2.2}$$

is a fitting parameter based on the characteristic width of the neck ('d'). They noticed that the prediction of this fitting parameter is difficult as the speed at which the neck collapses on the sharper downstream edge of the dispersed phase channel and the speed of the continuous fluid are not the same. Hence, this parameter was fitted to their experimental data and was found to be of order one. They also noted that the limiting case of droplet lengths correspond to $L \sim w_c$, suggesting that the continuous channel width plays a major role in the formation of the droplets. Although equation 2.1 was found to match well with their experimental results, the authors noticed that the applicability is questionable for channel geometries where $\Lambda = w_d / w_c < 1/2$.

Guillot and Colin (2005) have focused on the stability of parallel flows in a microfluidic T-junction. Based on their experiments, a regime map was created that describes the three modes of flow that are commonly encountered in T-junctions, i.e. droplets formed at the T-junction (DTJ), droplets formed in the channel (DC) and parallel flow (PF). The geometry of the microchannel chosen was different from the conventional T-junction microchannels, and the droplet formation was a consequence of the competing nature of two fluid streams colliding head-on, and subsequently guided through a funnel into the main channel. Their experimental findings reveal that the stability of parallel flows in a funneled T-junction is linked to the flow rates, wetting behavior, viscosity contrast and aspect ratio of the inlet channel for the two liquids.
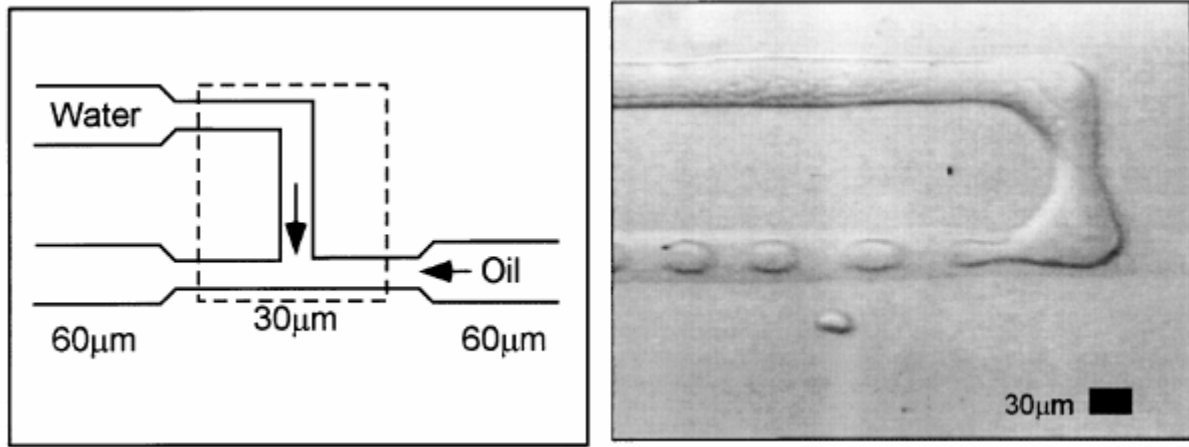
Figure 5: The T-junction geometry and emulsion formation of water in oil (from Thorsen et al (2001).
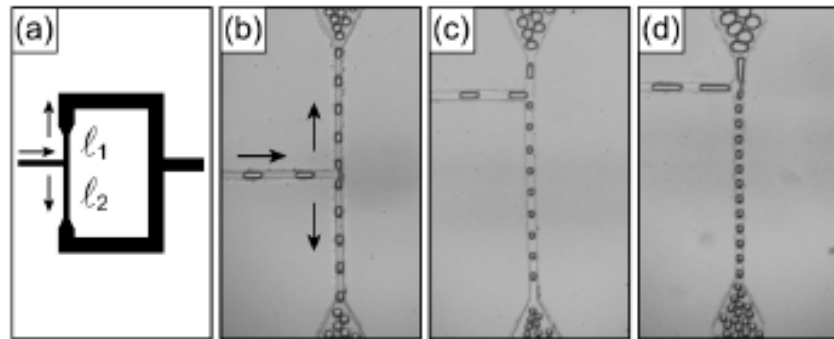
Figure 6: Passive breakup at T-junctions depending upon the flow resistances which are fixed by varying the lengths of the flow channels at the T-junction. Different lengths yield different droplet sizes at different frequencies (from Link et al (2004).
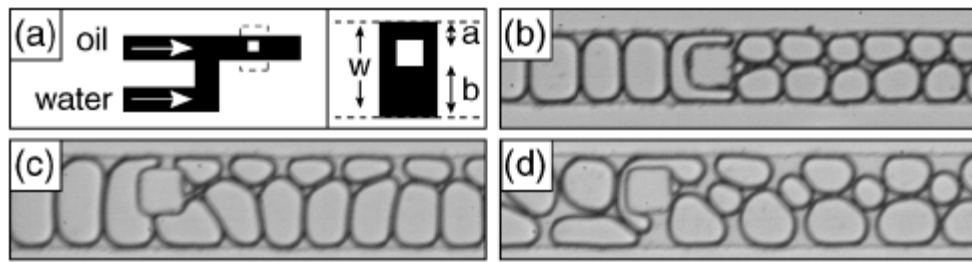
Figure 7: Obstruction induced passive breakup as shown by Link et al (2004).
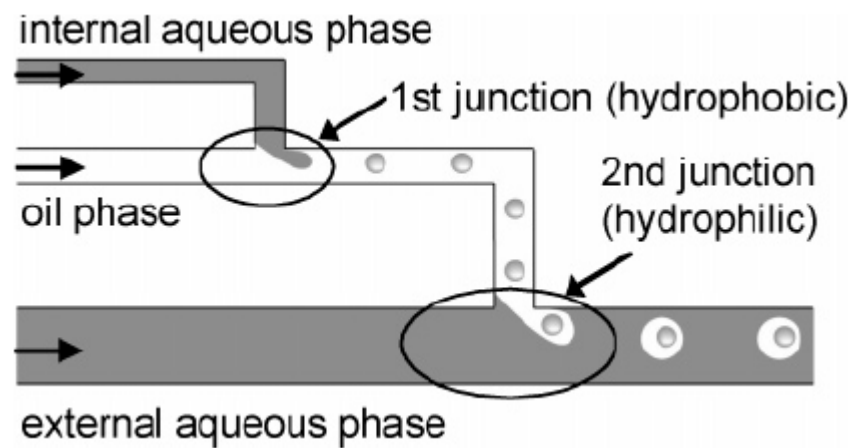
Figure 8: The concept for preparation of double emulsions (water-in-oil-in-water) using T-shaped microchannels as proposed by Okushima et al (2004) (from Okushima et al (2004)).

Xu et al (2008) have analyzed the formation of droplets in a T-junction microchannel and classified the flow regimes based on the Capillary number of the continuous phase. These are: squeezing ($Ca < 0.002$), transient ($0.002 < Ca < 0.01$) and dripping ($0.01 < Ca < 0.3$). Based on the flow regime prevalent at a particular Capillary number, correlations have been proposed to calculate the effective diameter of a spherical drop for Ca>0.01, and the length of the plugs formed for Ca<0.002. In the dripping regime, droplets of sizes comparable to the channel dimensions could be formed. This blocks the flow of the continuous phase, thereby increasing its velocity as it passes through a narrow constriction past the expanding droplet. Applying continuity based on the average velocities of the flow before and at this narrow gap,

$$U_c^g \left(w_c h - \frac{\pi}{4} d_D^2 \right) = U_c w_c h \tag{2.3}$$

where d_D is the diameter of the droplet. The Capillary number, based on the average velocity of the continuous phase in the narrow gap, was used to estimate the droplet diameter as

$$\frac{d_D}{d_i} \approx \frac{1}{Ca^g} = \frac{1}{Ca} \frac{w_c h - 0.785 d_D^2}{w_c h} \tag{2.4}$$

where d_i is the characteristic cross-section dimension of the main channel.

Christopher et al (2008) have proposed a scaling mechanism by which the size of the droplets formed at a microfluidic T-junction can be written in terms of the Capillary number of the flow. According to this analysis, droplet formation occurs when the interfacial force resisting the detachment of the expanding droplet cannot hold against the sum of the viscous drag acting due to the flow of the continuous phase and the pressure force that is generated due to a blockage of

the passage for the continuous phase to flow because of the protruding dispersed phase (see figure 9). The interfacial, shear and pressure forces in the original work were written as

$$F_{stension} \approx \sigma h \tag{2.5a}$$

$$F_{shear} \approx \frac{\mu_c Q_c b}{\left(w_c - b\right)^2} \tag{2.5b}$$

$$F_p \approx \frac{\mu_c Q_c b^2}{\left(w_c - b\right)^3} \tag{2.5c}$$

From a force balance, $F_{stension} = F_{shear} + F_p$, one can write this in terms of the non-dimensional length of the droplet $\bar{b}$ as

$$\left(1 - \bar{b}\right)^3 = \bar{b}Ca \tag{2.6}$$

The roots of this cubic polynomial were used to estimate the dimensionless volume of the droplet formed as

$$\bar{V} = \frac{V}{w_c^2 h} \approx \bar{b}^2 + \Lambda Q \tag{2.7}$$

They compared their experimental data with the theoretically derived equation 2.7, and found their results to be in reasonable agreement. Although they contend that due to an approximate form of the forces and simplistic assumptions that have been made to predict the dynamics of droplet formation in their model, discrepancies can arise when comparing other experimental data with their formulation of the same problem. A more robust and accurate model is required that can be used universally for such class of geometries.
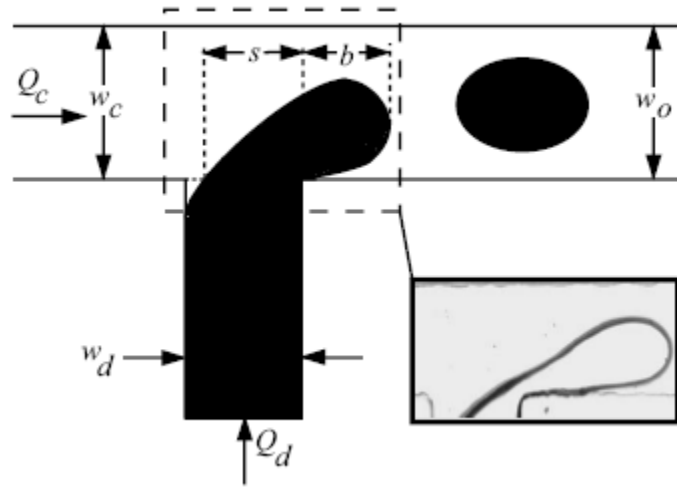
Figure 9: Schematic diagram showing the expanding droplet in the main channel, and (inset) experimental image of the droplet expansion (after Christopher et al (2008)).
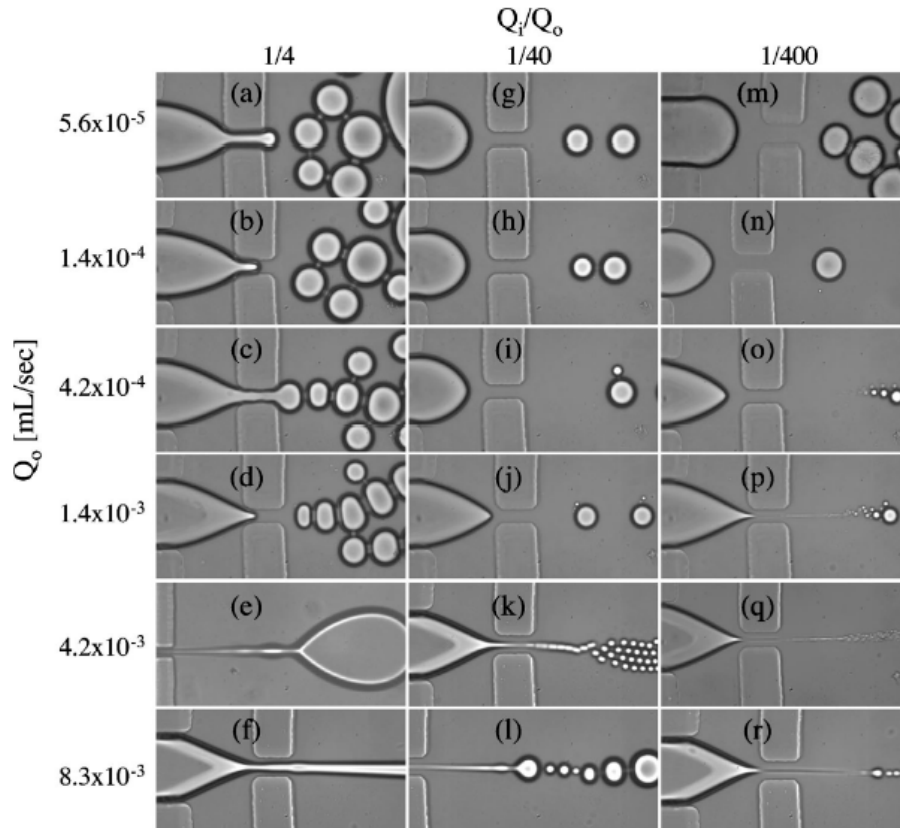
Figure 10: Phase diagram for a drop formation in flow focusing taken from Anna et al (2003). Each image represents the drop sizes and drop patterns that form at the specified value of Q_o and Q_i/Q_o.

Murshed et al (2008) have experimentally studied the effect of temperature on the droplet formation mechanism in a T-junction microchannel. In their experiments, TiO$_2$ nanoparticles of size 15 nm were dispersed in water and this nanofluid was used as the dispersed phase in a channel with $\Lambda = w_d / w_c = 1/3$. As the surface tension and viscosities reduce with an increase in temperature of the system, their findings reveal that droplets of a relatively larger size are formed as compared to droplets formed by using deionized water as the dispersed phase at the same temperature. In a separate study, Murshed et al (2009) describe the role of the nanoparticle shape on the droplet volumes for a range of temperatures in an oil-water system. Their work was carried out for two nanoparticle sizes of TiO$_2$ corresponding to spherical particles of size 15 nm and cylindrical particles of size 10 nm by 40 nm. It was found that cylindrical particles yield droplets of size larger than those observed for spherical particles. They attributed the role played by nanoparticles in the aqueous phase to the alteration in the interfacial slip due to the presence of the nanoparticles in the pure liquid.

2.2.3 Formation of Droplets using Elongational Stresses

Another innovative emulsification arrangement involves a configuration as shown in figure 10. Two dissimilar fluids flow in from the left hand channels, and are diverted through a thin orifice into a bigger channel. Depending upon the ratio of the flow rates of the two fluids, droplets of different sizes may form downstream that can be transported or used for analysis as in cytometers, or can be used to create emulsions that are mono- or polydisperse depending upon the coalescence/breakup of the dispersed phase. Droplets of one fluid in a second immiscible fluid are useful in a wide range of applications, particularly when the droplet size and the size

distribution can be prescribed on a micro- and nanoscale (Anna et al, 2003). Much of recent work on flow dispersions has centered on formation of emulsions in which the drop size and size distribution could be controlled. Anna et al (2003), using a flow focusing geometry, studied drop formation in liquid-liquid systems. They constructed a phase diagram that illustrates the drop size as a function of flow rates and flow rate ratios of the two liquids, as shown in figure 10. The technique was found to be successful in producing monodisperse and polydisperse emulsions that can be used in personal care products, foods, delivery of drugs and for organizing liquid-crystal droplets into optical devices (Hamouda et al, 1999).

Huang et al (2006) have shown experimental results of flow pattern arising as a consequence of two fluids passed through a thin orifice to produce single and double emulsions in a planar 3D flow focusing device. Their device could form monodisperse droplets ranging from 50 to 300 microns in diameter, with a coefficient of variance <4% in measured sizes. In another study, Takeuchi et al (2005) conducted experiments on an axisymmetric flow focusing device that produced droplets with significantly reduced polydispersity. They found that the size of the droplets formed in a vertically oriented arrangement was smaller than those formed at the same flow rates when the device was kept horizontal.

Garstecki et al (2004) describe a method of producing gas bubbles of sizes between 100 and 1000 microns in a heavier liquid through a flow focusing device. Their analysis showed that the volume of the bubbles formed could be written in terms of the flow rate and viscosity of the liquid, and the pressure of the gas stream as

$$V_b \propto \frac{p}{\mu q} \tag{2.8}$$

which was found to be consistent with experimental findings and suggests that the volume of the bubbles decreases as the product μq increases. On the other hand, Yobas et al (2006) describe a flow focusing geometry which can produce water-in-oil droplets at a frequency as high as 10 kHz, thereby showing an improved performance over other similar geometries described in the literature. Although, due to a weak dependence of the frequency on the flow rate of the dispersed phase (water), their results can only be explained on the basis of significant numerical modeling to delineate the effect of the geometry on the formation of droplets.

Anna and Mayer (2006) studied the droplet formation in a microfluidic flow focusing device using moderate concentrations of characterized surfactants in one of the liquid streams. They observed that the presence of surfactants influences the droplet formation mechanism. Their observation on the formation of droplets resembles the physical phenomenon which is similar to the formation of a tip on the exposed side of the interface that lies upstream of the narrow orifice of the flow-focusing geometry. Presence of surfactants in such concentrations was found to create droplets of size of the order of nanometers.

Nie et al (2008) report emulsification in a microfluidic device and study the effect of the viscosity on the droplet formation for a flow-focusing geometry. They found that the dominant mechanism of droplet formation is controlled by the flow rates for low viscosities of the dissimilar fluids. It was also inferred that the size of the droplets cannot be described based on

the Capillary number only. Other parameters, such as the physical properties of the fluids, and the flow rates play an important role as well.

2.3 Theoretical Work on Creation of Droplets in Microchannels

In the literature, two of the most frequently used approaches to model multiphase flows are the interface tracking (sharp interface) and the interface capturing (diffuse interface) methods. Interface tracking methods, though are accurate in predicting complex phenomena, suffer from numerical singularities that arise in the transitional zone when the interface is rapidly evolving (Cristini and Tan (2004)). This class of simulation technique includes the boundary integral method and finite-element based modeling of multiphase flows. On the other hand, techniques such as lattice Boltzmann, level-set, volume-of-fluid (VOF) and phase-field method are grouped into the interface capturing or diffuse interface methods. In these simulation techniques, the interface is spread over a finite thickness of the grid spacing(s), hence resulting in the terminology 'diffuse'. Fluid discontinuities that would generally appear in sharp-interface methods are smoothed out due to a gradual change across the interface. According to review of Anderson et al (1998):

> *...developments in modern computing technology have simulated a recent resurgence in the use of the diffuse interface models for the computation of flows associated with complex interface morphologies and topological changes, such as droplet breakup and coalescence...*

Diffuse interface techniques have found widespread acceptance in the research community for simulating flows with complex interfacial dynamics, and have been proven to be highly successful methods as well. A brief review on the existing work on simulation of droplet formation in the three most frequently used microfluidic geometries is described here in the context of sharp- and diffuse-interface methods.

2.3.1 Numerical Simulation for Co-flowing Fluids

In addition to the experimental studies carried out on formation of droplets in microchannels, theoretical work has gained attention in the past few years as well. Earliest theoretical work available on the formation of droplets has been on co-flowing geometries using the boundary integral method for the solution of the Stokes flow equations. Through their study, Zhang and Stone (1997) have studied the process with particular emphasis to understand the effect of viscosity on the size of the droplets formed. The range of parameters chosen for their study were given in terms of the Capillary number ($0.01 < Ca < 1$), viscosity ratio ($0.01 < \lambda < 1$) and the Bond number ($0.1 < Bo < 5$), where $Bo = \dfrac{\Delta \rho g R_0^2}{\sigma}$. Their simulations show that at a fixed Bo, the volume of the droplet increased as the Capillary number increased. Viscosity ratio variations did not result in a significant difference in the volume of the drops at low Capillary numbers in their simulations. Although it was found that for a fixed Ca, an increase in the viscosity ratio resulted in longer breaking times of the drops. Suryo and Basaran (2006) conducted simulations in a microfluidic device working on the co-flowing principle by solving the Stokes equation using the finite element method. They found that increasing the flow rate ratio $Q = Q_2 / Q_1$, where

Q_1 and Q_2 are the flow rates of the inner and outer fluids respectively, results in reduced volume of the drops formed at the tip of the concentric capillary. When this ratio was small, droplets were formed that almost occupied the whole width of the outer capillary and had a shape that resembled a cylinder with a hemispherical rear end. At higher values of the flow rate ratio, the drops became more spherical, with the radius of such a drop measured to be of the order of the inner radius of the capillary. Beyond a critical flow rate ratio, droplet formation occurred through the mechanism of tip streaming, in which the shape of the front interface of the expanding drop changed into a cone with a thin fluid jet, which had a radius at least an order of magnitude smaller than the inner capillary radius, that emanate from the tip of this cone.

2.3.2 Numerical Simulation in T-junction Microchannels

In a recent study by De Menech (2006), the phase-field method was applied to model the breakup of confined droplets at a symmetric T-shaped junction for low Reynolds number flows. The critical Capillary number at which the drop can be broken into daughter droplets was found to be a function of the viscosity contrast between the two liquids. Van der Graaf et al (2006) investigate the formation of droplets in a T-junction device using LBM. In their simulations, the widths of the continuous and dispersed phase channels were kept equal (i.e. $\Lambda = 1$), and simulations were conducted for $0.0033 \leq Ca \leq 0.065$ and flow rate ratios of $0.05 \leq Q \leq 1$ and a fixed viscosity ratio of $\lambda = 3.44$. Through LBM simulations, they proposed that the radius of the drops at pinch-off follows a relationship given by

$$\frac{r}{w_c} \sim Ca^{-1/4} \tag{2.9}$$

In a similar study with the same ratio for the widths of the channel widths by de Menech et al (2008), volume measurements of droplets formed at the T-junction were compared with existing experimental data and correlations. In this study, the viscosity ratios simulated were in the range $0.125 \leq \lambda \leq 1$. Two important inferences from this study for the formation of droplets in the squeezing regime were made. Firstly, the size of the droplets was not found to depend on the physical properties, such as viscosities and the interfacial tension of the two fluids. Secondly, the breakup for such low Capillary numbers was not driven by shear stresses that are typically exerted on the emerging droplets. In this squeezing regime, the time it took for the droplet to block the main channel and then pinch-off because of pressure build-up on the upstream continuous liquid, $\tau_{squeeze}$, was found to depend on the velocity of the continuous liquid only for the range of viscosities chosen in their study. On the other hand, in the dripping regime ($Ca \geq 0.02$), the normalized radius of the drops formed was found to obey a relationship given by

$$R = \frac{r}{w_c} = \frac{1}{\left(Ca\dot{\varepsilon}_d\right)^{0.4}} \tag{2.10}$$

where

$$\dot{\varepsilon}_d = \dot{\varepsilon} w_c / U_c \tag{2.11a}$$

and

$$\dot{\varepsilon} = \frac{U_g}{L_g} \qquad\qquad\qquad (2.11b)$$

is the shear strain in the narrow gap. It is worth noting that Thorsen et al (2001) had estimated the radius of the drops to be given by a balance of the interfacial and shear stress exerted by the accelerated continuous liquid as it moved through the narrow gap. Accordingly, the radius was written as

$$R = \frac{r}{w_c} \sim \frac{1}{Ca\dot{\varepsilon}_d} \qquad\qquad\qquad (2.12)$$

2.3.3 Numerical Simulation of Flow-Focusing

Jensen et al (2006) presented a numerical study of creation of gas bubbles in an axisymmetric flow focusing device, where the motion of the liquid phase is simulated through the governing equation for Stokes flow. In another study, Harvie et al (2006) simulated the motion of a Newtonian droplet as they passed through an axisymmetric contraction, similar to the flow focusing method of droplet generation. They used a transient form of the VOF method using the finite volume approach to model the behavior of the two liquids. Using numerical simulations, they created a phase chart of possible outcomes depending on the Capillary and Weber number of the flow. Under certain conditions, the spherical drop broke up into smaller drops as it passed through the contraction. Their results also reveal that for high Capillary number flows ($Ca \gg 0.01$), the thread that is formed inside the contraction, as the spherical droplet passes through it, exhibits a wavelike pattern, the wavelength of which decreased as the Weber number was increased.

Yu et al (2007) have used the lattice Boltzmann method to model the formation of droplets and bubbles in a flow-focusing cross-junction and converging channels. The dissimilar phases were modeled using a pseudo-potential model of LBM, given by Shan and Chen (1993), and the results were compared with in-house experiments conducted on the same geometries. The pseudo-potential method suffers from high spurious velocities at the interface. Thus it becomes questionable to use this method when the flow velocities are very small (i.e. for $Re \ll 1$). In a separate study, Wu et al (2008) have used a continuum surface force (CSF) description of the surface tension to simulate droplet formation in a cross-junction microchannel. This model is more robust and does not suffer from high spurious velocities as the Shan-Chen model. Their simulations, which were conducted for the range of Capillary numbers given by $0.00014 < Ca < 0.084$, show that the droplet size decreases as Ca increases. Their numerical results were found to be in good match with experimental data collected for the same geometry and flow conditions.

In another study, Zhou et al (2006) have used finite element based simulations in the framework of diffuse interface methods to study and characterize breakup of simple and compound droplets in an axisymmetric flow focusing microfluidic device. They observed that dripping is the mechanism for droplet formation at low flow rates. At higher flow rates, jetting becomes dominant. In addition, their work has focused on exploring the influence of a non-Newtonian liquid on the formation of droplets. More so, it was shown that the size of the droplets formed depends on the diameter of the downstream collection tube, thereby indicating the role of the device geometry on the mechanism as well.

2.4 Summary

In this chapter, an overview of the rich literature on droplet generation using passive microfluidic methods was provided. Although a vast array of studies have concentrated on fabrication and experiments on these devices, theoretical work has been rather limited. Theoretical work on understanding the role of the channel geometry, the flow rates and the physical properties of the two liquids in a T-junction microfluidic device has been limited to simplistic geometries, low viscosity ratios, and Capillary number less than 0.1. Keeping these issues in mind, as well as the difficulty encountered with numerical simulation of multiphase flows in complex geometries, there is a growing need to study the fundamental behavior in such two-fluid flow devices. To accomplish this, the lattice Boltzmann method is proposed as a tool to model the fluids and the interfacial phenomenon that arises through the dynamic movement of the interface separating the two liquids. In the following chapter, a foundation is laid that describes the path to model simple fluid flows using the discretized Boltzmann's equation. Thereafter, illustrations of the applicability of this novel technique are shown for some simple single and two-phase flows.

CHAPTER THREE: METHODOLOGY

3.1 Introduction

In the following sections, the lattice Boltzmann equation (LBE) has been derived from the Boltzmann's kinetic equation. The collision operator in the traditional Boltzmann's equation for the particle distribution function f_i is written in terms of a local Maxwellian distribution. This leads to a linear differential equation for the particle distribution function. In addition, three important features of LBM distinguish it from other numerical methods. These are:

1) The convection operator in velocity (phase) space is linear, which has been brought from kinetic theory and is in stark contrast with the non-linear convection terms in other approaches like the Navier-Stokes equations.

2) The incompressible form of the Navier-Stokes equations can be obtained in the nearly incompressible limit of LBM.

3) In the Maxwell-Boltzmann equilibrium distribution, the phase space is a complete functional space, due to which the averaging involves the whole velocity (phase) space. In LBM, only a few moving directions are used and thus the transformation that relates the microscopic properties is simplified.

To show that the LBE bridges the gap from microscopic physics to the real world fluid phenomenon, the Navier-Stokes equations have been derived starting from the Bhatnagar-Gross-Krook (BGK) form of the collision operator (Bhatnagar et al (1954)) using the zeroth and first order moments of the particle distribution functions, and for the special form of the equilibrium

distribution function in section 3.3. The numerical implementation of the LBGK has been described in section 3.4. Since LBM deals with the distribution function as the dependent variable, applying macroscopic boundary conditions in terms of velocity of pressure becomes a non-trivial process. Some of the available methods to accomplish this task are discussed in section 3.5. The multiphase models used in the current study for simulating two immiscible phases have been described in section 3.6. The advantages and disadvantages of these models are explained in addition to a discussion on existing models for simulation of two-phase flows in the context of LBM.

3.2 Lattice BGK from Boltzmann's Equation

In LBM, the evolution equation for the particle distribution function is very similar to the kinetic equation in lattice gas automata, given by

$$f_i\left(\mathbf{x}+\mathbf{e_i}\Delta t, t+\Delta t\right)=f_i\left(\mathbf{x},t\right)+\Omega_i\left[f_i\left(\mathbf{x},t\right)\right]$$
where $i=0,1,....,M$

$\qquad$ (3.1)

Ω_i is the collision operator and takes into account the collision of the fluid particles and satisfies the relationships given by,

$$\sum_i \Omega_i = 0 \quad \& \quad \sum_i \Omega_i \mathbf{e}_i = 0$$

$\qquad$ (3.2)

at each lattice location.

If equation (3.1) is expanded in a Taylor series about ε, a small parameter and proportional to the Knudsen number, i.e.

$$\left|\Delta\mathbf{x}\right|, \Delta t \approx O\left(\varepsilon\right)$$

$\qquad$ (3.3)

Then on expansion, we get

$$f_i\left(\mathbf{x}+\mathbf{e}_i\Delta t,t+\Delta t\right)=f_i\left(\mathbf{x},t\right)+\varepsilon\frac{\partial f_i}{\partial t}+\varepsilon\mathbf{e}_i.\nabla f_i+\frac{\varepsilon^2}{2}\frac{\partial^2 f_i}{\partial t^2}+\frac{\varepsilon^2}{2}\left(\mathbf{e}_i.\nabla f_i\right)^2+\frac{\varepsilon^2}{2}\left(\mathbf{e}_i.\nabla\right)\frac{\partial f_i}{\partial t}+O\left(\varepsilon^3\right)$$

$$=f_i\left(\mathbf{x},t\right)+\Omega_i \tag{3.4a}$$

$$\Rightarrow\frac{\partial f_i}{\partial t}+\mathbf{e}_i.\nabla f_i+\varepsilon\left[\frac{1}{2}\frac{\partial^2 f_i}{\partial t^2}+\frac{1}{2}\left(\mathbf{e}_i\mathbf{e}_i:\nabla\nabla f_i\right)+\frac{1}{2}\left(\mathbf{e}_i.\nabla\right)\frac{\partial f_i}{\partial t}\right]+O\left(\varepsilon^2\right)=\frac{\Omega_i}{\varepsilon} \tag{3.4b}$$

Using the Chapman-Enskog expansion, where we use

$$\frac{\partial}{\partial t}=\varepsilon\frac{\partial}{\partial t_1}+\varepsilon^2\frac{\partial}{\partial t_2}\quad;\quad\frac{\partial}{\partial x}=\varepsilon\frac{\partial}{\partial x_1} \tag{3.5}$$

where t_1 is the convection time scale and t_2 is the diffusion time scale such that $t_1\gg t_2$. Further,

the particle distribution functions can be expanded as

$$f_i=f_i^{eq}+\varepsilon f_i^{neq}\quad\&\quad\sum_i f_i^{eq}=0\,,\,\sum_i f_i^{eq}\mathbf{e}_i=\mathbf{0} \tag{3.6a}$$

$$f_i^{neq}=f_i^{(1)}+\varepsilon f_i^{(2)}+O\left(\varepsilon^2\right) \tag{3.6b}$$

and $\quad\sum_i f_i^{1,2}=0\quad;\quad\sum_i f_i^{1,2}\mathbf{e}_i=\mathbf{0} \tag{3.6c}$

Thus the collision operator up to third order is given by

$$\Omega_i\left(f\right)=\Omega_i\left(f^{eq}\right)+\varepsilon\frac{\partial\Omega_i\left(f^{eq}\right)}{\partial f_j}f_j^{(1)}+\varepsilon^2\left(\frac{\partial\Omega_i\left(f^{eq}\right)}{\partial f_j}f_j^{(2)}+\frac{\partial^2\Omega_i\left(f^{eq}\right)}{\partial f_j\partial f_k}f_j^{(1)}f_k^{(1)}\right)+O(\varepsilon^3) \tag{3.7}$$

For small ε, $\lim_{\varepsilon\to0}\Omega_i\left(f^{eq}\right)=0$. Thus the above equation would reduce to

$$\frac{\Omega_i\left(f\right)}{\varepsilon}=\frac{\partial\Omega_i\left(f^{eq}\right)}{\partial f_j}f_j^{(1)}+\varepsilon\frac{\partial\Omega_i\left(f^{eq}\right)}{\partial f_j}f_j^{(2)}+O\left(\varepsilon^2\right) \tag{3.8a}$$

$$= \frac{\partial \Omega_i \left(f^{eq} \right)}{\partial f_j} \left[f_j^{(1)} + \varepsilon f_j^{(2)} \right] = \frac{\partial \Omega_i \left(f^{eq} \right)}{\partial f_j} \left[f_j^{neq} \right]$$

$$= \frac{1}{\varepsilon} \frac{\partial \Omega_i \left(f^{eq} \right)}{\partial f_j} \left(f_j - f_j^{eq} \right) \tag{3.8b}$$

$$= \frac{M_{ij}}{\varepsilon} \left(f_j - f_j^{eq} \right)$$

where M_{ij} is the collision matrix (Higuera and Jiminez (1989)). Further assuming that the local

particle distribution function relaxes to an equilibrium state at a single rate 'τ', so that

$$M_{ij} = -\frac{1}{\tau} \delta_{ij} \tag{3.9}$$

we arrive at the lattice BGK collision term,

$$\frac{\Omega_i}{\varepsilon} = -\frac{f_i^{neq}}{\tau} = -\frac{\left(f_i - f_i^{eq} \right)}{\varepsilon \tau} \tag{3.10}$$

This form of the collision operator with the single time relaxation approximation is also known

as the lattice BGK (Bhatnagar-Gross-Krook) operator. This form of the collision operator

reduces (3.1) to a differential equation of the form

$$\frac{\partial f_i}{\partial t} + \mathbf{e}_i \cdot \nabla f_i = -\frac{\left(f_i - f_i^{eq} \right)}{\tau} + \Phi_i \tag{3.11}$$

where Φ_i is the potential as a consequence of any external force applied on the fluid. Equation

3.11 can be discretized in time and discrete-velocity space. There are two commonly used

discretization methods for this differential equation that are widely cited and used. The most

commonly used is the 'explicit' formulation in which the collision operator is written in terms of

the distribution functions calculated on the previous time step. This results in

$$\frac{f_i\left(\mathbf{x}+\mathbf{e}_i\delta t,t+\delta t\right)-f_i\left(\mathbf{x}+\mathbf{e}_i\delta t,t\right)}{\delta t}+$$

$$\frac{f_i\left(\mathbf{x}+\mathbf{e}_i\delta t,t\right)-f_i\left(\mathbf{x},t\right)}{\delta x}=-\frac{\left(f_i\left(\mathbf{x},t\right)-f_i^{eq}\left(\mathbf{x},t\right)\right)}{\tau}+\Phi_i \qquad (3.12)$$

Assuming $\delta x = \delta t = 1$, equation 3.12 simplifies to the most commonly used 'explicit' lattice Boltmann equation (LBE), given as

$$f_i\left(\mathbf{x}+\mathbf{e}_i\delta t,t+\delta t\right)-f_i\left(\mathbf{x},t\right)=-\frac{\left(f_i\left(\mathbf{x},t\right)-f_i^{eq}\left(\mathbf{x},t\right)\right)}{\tau}+\Phi_i \qquad (3.13a)$$

This is the 'explicit' lattice BGK equation (LBE). Recently, Sankaranarayanan et al (2002) have suggested a 'Crank-Nicolson' way of discretizing the collision operator that according to them is a more stable scheme and is much more suitable for simulating low viscosity fluids. In this formulation, equation 3.11 is discretized based on 'one-half' contribution from the current time step, and the other half from the previous time step. This would reduce the differential equation to

$$f_i^{AC}\left(\mathbf{x},t+\delta t\right)-f_i\left(\mathbf{x},t\right)=$$

$$-\left[\frac{f_i^{AC}\left(\mathbf{x},t+\delta t\right)-f_i^{eq,AC}\left(\mathbf{x},t+\delta t\right)}{2\tau}+\frac{f_i\left(\mathbf{x},t\right)-f_i^{eq}\left(\mathbf{x},t\right)}{2\tau}\right]+\Phi_i \qquad (3.13b)$$

where 'AC' denotes the quantities after the collision step. Due to its implicit nature, this equation is no longer a time-marching algorithm and needs multiple iterations at each time step for the solution to converge. Subsequent to finding the converged solution, these after-collision distributions are streamed to the neighboring lattice nodes.

3.2.1 Original Lattice Boltzmann Equation

The density per node and the macroscopic momentum flux in the weakly compressible formulations as defined in equation (3.13a,b) is given by

$$\rho = \sum_i f_i \;\; ; \;\; \rho\mathbf{u} = \sum_i f_i \mathbf{e}_i \tag{3.14}$$

The equilibrium distribution functions depend only on local density and velocity and for a three-dimensional lattice (D3Q19) can be expressed in the following form:

$$f_i^{eq} = \begin{cases} \dfrac{\rho}{3}\left(1 - \dfrac{\mathbf{u}.\mathbf{u}}{2c_s^2}\right) & , i = 0 \\[3mm] \dfrac{\rho}{18}\left(1 + \dfrac{\mathbf{e}_i.\mathbf{u}}{c_s^2} + \dfrac{(\mathbf{e}_i.\mathbf{u})^2}{2c_s^4} - \dfrac{\mathbf{u}.\mathbf{u}}{2c_s^2}\right) & ,1 \le i \le 6 \\[3mm] \dfrac{\rho}{36}\left(1 + \dfrac{\mathbf{e}_i.\mathbf{u}}{c_s^2} + \dfrac{(\mathbf{e}_i.\mathbf{u})^2}{2c_s^4} - \dfrac{\mathbf{u}.\mathbf{u}}{2c_s^2}\right) & ,7 \le i \le 18 \end{cases} \tag{3.15}$$

where f_i^{eq} is the equilibrium distribution of particles moving in direction 'i'. For the 'explicit scheme' the leading truncation error of a velocity-space discretization is taken into account in a way scuh that to ensure that the viscosity in the NS equation derived from equation 3.11 becomes

$$v = \left(\tau - \dfrac{1}{2}\right)c_s^2 \delta t \tag{3.16a}$$

where the positivity of the viscosity requires that $\tau > 1/2$. For the 'Crank-Nicolson' scheme of discretizing the collision operator, the kinematic viscosity has the form

$$\nu = \tau c_s^2 \delta t \tag{3.16b}$$

Since the 'implicit' scheme does not have any requirement on the minimum viscosity that can be simulated (except $\tau > 0$), the scheme may present a more viable option for simulating flows where the viscosity of the fluid is needed to be kept small, with a slight disadvantage as the solution procedure is iterative as compared to the explicit formulation of the LBE.

3.2.2 Incompressible Lattice Boltzmann Equation

In the original LBE, derivation of the incompressible form of the Navier-Stokes equation is possible through the Chapman-Enskog expansion, assuming that the density fluctuation in the main flow is of $O(M^2)$, where M is the Mach number. Due to the nature of the moment equations, given by equation (3.14), numerical artifacts and rounding-off errors may introduce compressibility in the density of the fluid. More so, as the pressure is tied to the local density and hence is not an independent variable in the LBE, flows with moderate to large pressure gradients result in substantial changes in the density of the supposedly 'incompressible' fluid. Through an incompressible formulation of the original Boltzmann's equation, density fluctuations can be minimized, but at the cost of temporal variation of the fluid flow. A definite advantage of this method over the original LBE is the ease and accurate specification of pressure boundary conditions. The only modifications made to the original formulation are in the form of the equilibrium distribution function, as well as the fact that the zeroth order moment yields the pressure (and not the density) of the fluid as a function of space and time. The equilibrium functions are written as (He and Luo (1997)):

$$
f_i^{eq} = \begin{cases} \dfrac{1}{3}\left(\rho - \dfrac{\mathbf{u.u}}{2c_s^2}\right) & , i = 0 \\[2.5em] \dfrac{1}{18}\left(\rho + \dfrac{\mathbf{e}_i.\mathbf{u}}{c_s^2} + \dfrac{(\mathbf{e}_i.\mathbf{u})^2}{2c_s^4} - \dfrac{\mathbf{u.u}}{2c_s^2}\right) & ,1 \leq i \leq 6 \\[2.5em] \dfrac{1}{36}\left(\rho + \dfrac{\mathbf{e}_i.\mathbf{u}}{c_s^2} + \dfrac{(\mathbf{e}_i.\mathbf{u})^2}{2c_s^4} - \dfrac{\mathbf{u.u}}{2c_s^2}\right) & ,7 \leq i \leq 18 \end{cases} \tag{3.17}
$$

such that

$$
\sum_i f_i = \rho = \frac{p}{\rho_0 c_s^2} \tag{3.18a}
$$

$$
\sum_i f_i \mathbf{e}_i = \mathbf{u} \tag{3.18b}
$$

where ρ_0 is the density of the fluid and is a constant parameter. Although this formulation of the LBE recovers the steady incompressible Navier-Stokes equation, the scheme is not conducive for high Reynolds number flows as is the case with the original formulation.

3.3 Navier-Stokes from LBE

The particular form of the collision operator with the single time relaxation approximation, also known as the lattice BGK (Bhatnagar-Gross-Krook) operator leads to a differential equation of the form given by equation 3.11 for the Boltzmann's kinetic equation. In the low frequency, long wavelength limit and under zero external forces, the Chapman-Enskog expansion can be used under the assumption that $\delta x \approx \delta t \approx \varepsilon$, where ε is a small parameter as compared to the macroscopic scales and is proportional to the Knudsen number. Thus, the particle distribution functions can be expanded in a Taylor series about ε,

43

$$f_i = f_i^{eq} + \varepsilon f_i^{(1)} + \varepsilon^2 f_i^{(2)} + O(\varepsilon^3) \tag{3.19}$$

Similarly, the time and space derivatives can be expanded as

$$\frac{\partial}{\partial t} = \varepsilon \frac{\partial}{\partial t_1} + \varepsilon^2 \frac{\partial}{\partial t_2} \quad , \quad \frac{\partial}{\partial x} = \varepsilon \frac{\partial}{\partial x_1} \tag{3.20}$$

To recover the Navier-Stokes equations from the BGK form of the LBE, we need to substitute equation 3.19 and 3.20 into 3.11. This would give

$$\left(\frac{\partial f_i^{eq}}{\partial t_1} + \mathbf{e}_i \cdot \nabla_1 f_i^{eq} + \frac{1}{\tau} f_i^{(1)} \right) \varepsilon^0 + \left(\frac{\partial f_i^{eq}}{\partial t_2} + \left(1 - \frac{1}{2\tau} \right) \left(\frac{\partial f_i^{(1)}}{\partial t_1} + \mathbf{e}_i \cdot \nabla_1 f_i^{(1)} \right) + \frac{1}{\tau} f_i^{(2)} \right) \varepsilon^1$$

$$+ O(\varepsilon^2) = 0$$

$$\tag{3.21}$$

where higher order terms have been grouped together. Filtering out $O(\varepsilon^0)$ and $O(\varepsilon^1)$ terms leads to

$$\frac{\partial f_i^{eq}}{\partial t_1} + \mathbf{e}_i \cdot \nabla_1 f_i^{eq} = -\frac{1}{\tau} f_i^{(1)} \tag{3.22a}$$

and

$$\frac{\partial f_i^{eq}}{\partial t_2} + \left(1 - \frac{1}{2\tau} \right) \left(\frac{\partial f_i^{(1)}}{\partial t_1} + \mathbf{e}_i \cdot \nabla_1 f_i^{(1)} \right) = -\frac{1}{\tau} f_i^{(2)} \tag{3.22b}$$

Using the condition that the zeroth and first order moments of the equilibrium particle distribution function give the macroscopic density and momentum flux respectively (equation 3.14), and the form of the equilibrium distribution function as given in equation 3.15 simplifies equation 3.22 to the governing equations that have the form given by,

$$\frac{\partial \rho}{\partial t} + \nabla.\rho\mathbf{u} = 0 \tag{3.23a}$$

$$\frac{\partial}{\partial t}(\rho\mathbf{u}) + \nabla.\left[\sum_i \mathbf{e}_i\mathbf{e}_i f_i^{eq} + \left(1 - \frac{1}{2\tau}\right)\sum_i \mathbf{e}_i\mathbf{e}_i f_i^{(1)}\right] = \mathbf{0} \tag{3.23b}$$

Chen and Doolen (1998) show that the two summations in equation 3.23b can be reduced to

$$\sum_i (\mathbf{e}_i)_\alpha (\mathbf{e}_i)_\beta f_i^{eq} = p\delta_{\alpha\beta} + \rho u_\alpha u_\beta$$

$$\left(1 - \frac{1}{2\tau}\right)\sum_i (\mathbf{e}_i)_\alpha (\mathbf{e}_i)_\beta f_i^{(1)} = \upsilon\left(\nabla_\alpha(\rho u_\beta) + \nabla_\beta(\rho u_\alpha)\right) \tag{3.24}$$

where $p = c_s^2\rho$ & $\upsilon = c_s^2(\tau - 1/2)$. The resulting momentum equation is

$$\rho\left(\frac{\partial \mathbf{u}}{\partial t} + \mathbf{u}.\nabla\mathbf{u}\right) = -\nabla p + \upsilon\nabla^2(\rho\mathbf{u}) + \upsilon\nabla\nabla.(\rho\mathbf{u}) \tag{3.25}$$

As is evident, the lattice Boltzmann equation is able to recover the weakly incompressible form of the Navier-Stokes equation in the low Mach number limit using the Chapman-Enskog expansion, and is second order accurate in space. Hence, the lattice Boltzmann's equation is a tool which can bridge the gap between the microscopic fluid interactions and the macroscopic world.
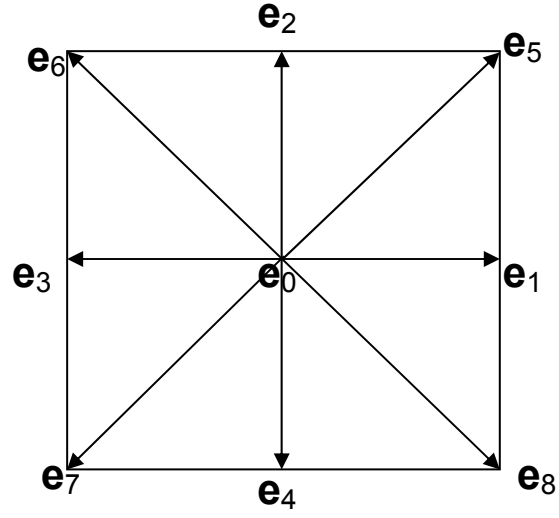
(a) D2Q9
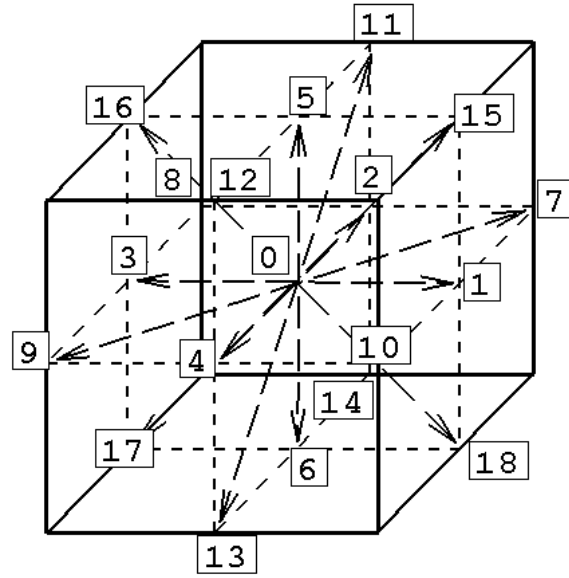
(b) D3Q19

Figure 11: Discrete velocity vectors for the (a) 2-D nine speed, and (b) 3-D 19 speed model.

3.4 Numerical Implementation

In this work, the D2Q9 and D3Q19 form of the discrete velocity space would be used that yield a square and cubic lattice for the space discretization, respectively. For such a model, the phase space velocities are shown in figure 11. The velocity vectors are given as:

$$\mathbf{e}_a = \begin{cases} (0,0), & a = 0; \\ (\pm 1,0)c,(0,\pm 1)c, & a = 1,2,3,4; \\ (\pm 1,\pm 1)c, & a = 5,6,7,8. \end{cases} \tag{3.26a}$$

for the D2Q9 lattice arrangement, and

$$\mathbf{e}_a = \begin{cases} (0,0,0), & a = 0; \\ (\pm 1,0,0)c,(0,\pm 1,0)c,(0,0,\pm 1)c & a = 1,2,..,6; \\ (\pm 1,\pm 1,0)c,(\pm 1,0,\pm 1)c,(0,\pm 1,\pm 1)c & a = 7,8,..,18. \end{cases} \tag{3.26b}$$

for the D3Q19 configuration, where 'c' is the lattice speed and is given by $c = \delta x / \delta t$. The other forms of the velocity discretization commonly used are D2Q7 (hexagonal lattice) and D3Q15 (15 velocity 3-D model).

Broadly, the 'explicit' lattice Boltzmann scheme consists of two computational steps,

collision step: $f^{AC}{}_i(\mathbf{x},t) - f_i(\mathbf{x},t) = -\dfrac{1}{\tau}\left[f_i(\mathbf{x},t) - f_i^{eq}(\mathbf{x},t) \right] + \Phi_i$ (3.27a)

streaming step: $f_i(\mathbf{x} + \mathbf{e}_i \delta t, t + \delta t) = f_i^{AC}(\mathbf{x},t)$ (3.27b)

where f_i and f_i^{AC} denote the pre- and post-collision state of the distribution function, respectively. This form of an implementation justifies the very reason why the LBE has been regarded as a preferred tool over the Navier-Stokes equations and solvers. As is evident from

47

equation 3.27, the LBE is a simple time-marching algorithm for the particle distribution function, whereas the NS involves non-linear advection terms that make the process iterative. Because of its explicit form, the LBE is easy to implement, and natural to parallelize as the collision step is completely local and the streaming step takes very little computational effort at every time step. However unlike the macroscopic solvers for which a no-slip boundary condition for the velocity u on the wall is easily satisfied, there is no similar form available for boundary condition for the particle distribution function(s). Several different ways and treatments have been proposed in literature to date, and have been summarized below.

3.5 Boundary Conditions in LBM

A lot of work has been done on creating newer and reliable boundary conditions in the Bhatnagar-Gross-Krook variant of the LBE. Some of the boundary conditions commonly encountered in fluid flows are related to stationary or moving wall, inlet or outlet velocity, and inlet/outlet pressure. Since the lattice Boltzmann method works with the particle distribution function as the dependent variable, specification of velocity or pressure boundary conditions becomes a highly complex process. In many scenarios, solving for the distribution function based on the macroscopic variables on the boundary could lead to a set of equations that may not have a closed form solution. With regard to such issues, simple rules have been formulated and proposed in literature through which a closure, which is physically harmonious to the problem at hand and at the same time is easy to implement with good accuracy, can be achieved.

The simplest form of wall boundary condition that has been quoted innumerably in literature is the pure wall bounceback proposed by Wolfram (1986) and Lavallée at al (1991). In this form, the particle distribution function streamed to the wall is scattered (reflected) along the same direction it came from, as shown in figure 12a. Accordingly, the unknown distributions going from the wall into the fluid nodes can be written as

$$f_2(\mathbf{x}) = f_4(\mathbf{x}),\, f_5(\mathbf{x}) = f_7(\mathbf{x}),\, f_6(\mathbf{x}) = f_8(\mathbf{x}) \tag{3.28}$$

Because of the local nature of the standard bounceback scheme, it was later found by many groups (Cornubert et al (1991), Ziegler (1993) and Guinzbourg and Adler (1994)) that the no-slip boundary condition described by equation 3.28 is only first order accurate. Since the LBE is second order accurate in space, use of the standard bounceback results in loss of accuracy near the walls. Skordos (1993) suggested that to eliminate this fallacy, velocity gradients should be included in the equilibrium distribution function at the wall nodes. It was also found that in certain situations, using wall bounceback resulted in a fictitious slip velocity near the wall nodes. Though it has disadvantages, because of its simplicity and ease of handling even in complex geometries and flow situations, the standard wall bounceback is the easiest of all no-slip boundary conditions that can be found in literature.

Ziegler (1993) in his work found that shifting the wall (boundary) half-mesh unit into the fluid, in other words applying the bounceback between the nodes, yields second order accuracy at the walls. This scheme is popularly known as the half-way bounceback method and is shown in figure 12b. The unknown distributions streamed into the fluid from the wall side are given as
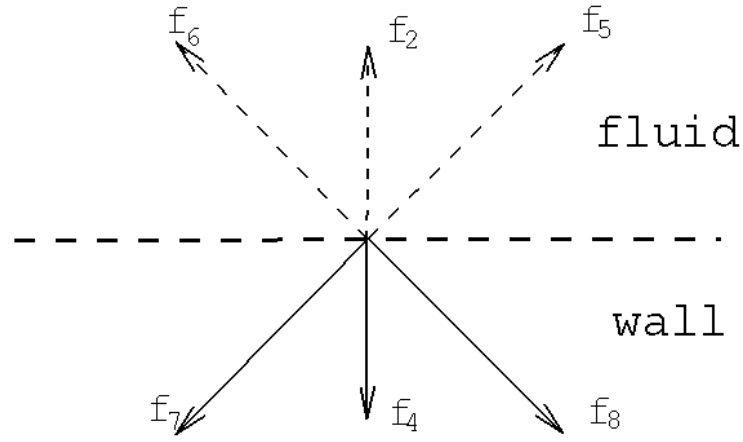
(a) Standard Bounceback
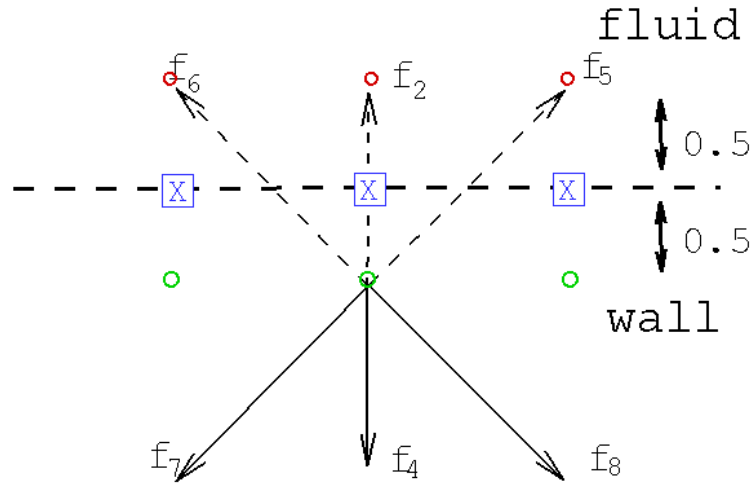
(b) Half-way Bounceback

Figure 12: Schematic to show the working of the standard and half-way bounceback schemes for enforcing zero velocity on the wall. The physical location of the wall is shown by dotted horizontal lines. The known (unknown) distributions are shown by solid (dashed) arrows.

$$f_2(\mathbf{x}) = f_4(\mathbf{x} + \mathbf{e}_4), f_5(\mathbf{x}) = f_7(\mathbf{x} + \mathbf{e}_7), f_6(\mathbf{x}) = f_6(\mathbf{x} + \mathbf{e}_6) \tag{3.29}$$

According to this closure of the wall boundary distributions, it can be observed that the fluid momenta carried by each of the distributions cancels off completely half-way between the wall (green) and fluid (red) nodes, and thereby making the boundary treatment second order accurate.

Other than the traditional bounceback schemes described earlier, other methods that deal with handling of the wall and inlet-outlet boundary conditions in context of LBM also exist. For instance, Inamuro et al (1995) proposed a new form of LBE in which a slip velocity was included to nullify the effect of the 'false' slip created at the boundary because of the use of bounceback. In their study, unknown distribution functions at the wall, which point towards the fluid region, were assumed to be equilibrium distribution functions with a counter slip velocity which was determined by setting the fluid velocity at the wall to the wall velocity. Although novel in its treatment, their method had shortcomings in dealing with corners. In a separate work, Noble et al (1995) proposed the use of hydrodynamic boundary conditions on no-slip walls by enforcing a pressure gradient. During each time step in the LBM procedure, the particle distribution at each node is modified by collision, forcing and streaming. The goal of the hydrodynamic approach was to prescribe this process in a way such that the desired velocity conditions are satisfied at the end of the time step. Maier at al (1996) in their work modified the bounceback condition to nullify net momentum tangent to the wall and preserve momentum normal to the wall. In their work, they proposed that for the case in 3-D lattices where the number of unknown particle distribution functions at the boundaries exceeds the number of equations to be solved, supplementary rules for the external links need to be enforced, which

employ extrapolation for density conditions and mass addition and redistribution for velocity conditions. Their methods were tested for standard benchmark problems like Poiseuille flow, Couette flow, and duct and pipe flow.

Chen at al (1996) adopted a staggered mesh discretization from the traditional finite difference methods and proposed using a second-order extrapolation scheme of distributions in the flow to obtain the unknown distribution functions. They proposed a simple extrapolation scheme in place of wall bounceback method (figure 13). They argued that the bounceback scheme works well only when $\tau = 1$. For other values of the relaxation parameter, the bounceback scheme does not yield results that match analytical solutions. It was also emphasized that since the relaxation parameter is a measure of the fluid viscosity, and since high velocities cannot be simulated in lattice Boltzmann method because of the inherent low Mach number restriction, simulating high Reynolds number flows can be a problem with conventional treatment of the wall which limit the minimum viscosity of the fluid. Their extrapolation employed one additional set of nodes beyond the boundary nodes which lie inside the wall. The distribution functions at this row of nodes were calculated using the particle distribution function values at the wall and the layer of one lattice nodes of fluid adjacent to the boundary nodes. Thus if f_i^{-1}, f_i^0 and f_i^1 are the distribution functions on the outside layer, the wall layer and the first layer inside the fluid respectively, then according to Chen et al (1996)

$$f_i^{-1} = 2f_i^0 - f_i^1 \tag{3.30}$$

Once f_i^{-1} is known, streaming of the distribution function is carried out. The collision step is the normal collision carried out for all fluid nodes, except the wall nodes where velocity or pressure boundary conditions are enforced using the equilibrium distribution function. The important thing to note about this method is that it does not require any assumptions about the incoming distribution functions as was the case with other schemes like that proposed by Zou and He (1997). This scheme was tested by the authors for Poiseuille flow, flow in a lid-driven cavity and flow over a column of cylinders among other standard problems with success.

In a separate paper, Mei et al (1999) developed a second accurate treatment of boundary conditions for curved boundaries. Until then, a standard way to deal with irregular boundaries was to treat the surface as a series of stairs, which invariably resulted in less accurate computations. In their formulation, as shown in figure 14, the location of the wall is recorded and used to calculate the fractional distance of the nearest fluid node from which distribution would be streamed to the corresponding wall node. Hence,

$$\Delta = \frac{\left| \mathbf{x}_f - \mathbf{x}_w \right|}{\left| \mathbf{x}_f - \mathbf{x}_b \right|} \tag{3.31}$$

According to the definition, $0 \leq \Delta \leq 1$. The unknown distribution functions that are to be streamed from the wall node to the fluid nodes are computed as

$$f_{\bar{\alpha}}\left(\mathbf{x}_f = \mathbf{x}_b + \mathbf{e}_{\bar{\alpha}}, t+1 \right) = \widetilde{f}_{\bar{\alpha}}\left(\mathbf{x}_b, t \right) \tag{3.32}$$

where

$$\widetilde{f_{\bar{\alpha}}}\left(\mathbf{x}_b, t\right) = \left(1 - \chi\right)\widetilde{f_\alpha}\left(\mathbf{x}_f, t\right) + \chi f_\alpha^{(*)}\left(\mathbf{x}_b, t\right) + 2 w_\alpha \rho \frac{3}{c^2}\mathbf{e}_{\bar{\alpha}} \cdot \mathbf{u}_w \qquad (3.33)$$

and $\mathbf{u}_w \equiv \mathbf{u}_w\left(\mathbf{x}_w, t\right)$ is the velocity of the wall node, χ is a weighing factor and $f_\alpha^{(*)}$ is a fictitious equilibrium distribution, given as

$$f_\alpha^{(*)}\left(\mathbf{x}_b, t\right) = w_\alpha \rho\left(\mathbf{x}_f, t\right)\left\{1 + \frac{3}{c^2}\mathbf{e}_\alpha.\mathbf{u}_{bf} + \frac{9}{2c^4}\left(\mathbf{e}_\alpha.\mathbf{u}_f\right)^2 - \frac{3}{2c^2}\mathbf{u}_f.\mathbf{u}_f\right\} \qquad (3.34)$$

In equation 3.34, $\mathbf{u}_{bf}$ is chosen according to the following criteria,

$$\mathbf{u}_{bf} = \frac{\left(\Delta - 1\right)}{\Delta}\mathbf{u}_f + \frac{1}{\Delta}\mathbf{u}_w \quad \text{and} \quad \chi = \frac{\left(2\Delta - 1\right)}{\tau} \quad \text{for } \Delta \geq 1/2 \qquad (3.35a)$$

$$\mathbf{u}_{bf} = \mathbf{u}_{ff} = \mathbf{u}_f\left(\mathbf{x}_f + \mathbf{e}_{\bar{\alpha}}, t\right) \quad \text{and} \quad \chi = \frac{\left(2\Delta - 1\right)}{\left(\tau - 2\right)} \quad \text{for } \Delta < 1/2 \qquad (3.35b)$$

This scheme was found to give better accuracy than standard bounceback. Also, flows at a lower value of the relaxation parameter could be solved without the system becoming unstable. In a later work, Mei et al (2000) extended the idea to deal with arbitrary curved 3-D solid geometry and found the method to possess good stability characteristics and second order accuracy

Other than these methods that have relied on specification of zero velocity on the boundary, Zou and He (1997) extended the wall bounceback of the non-equilibrium part of the particle distribution function. They used the macroscopic variables known at the boundary to determine the unknown distribution functions pointing into the fluid by using bounceback for the non-equilibrium part of the particle distribution function. According to this method shown in figure

15, the unknown distributions at the inlet and outlet can be prescribed based on the velocity (or pressure) boundary condition for the macroscopic variables. For example, if the velocity is known on the inlet nodes, such that $u_x(0, y) = u_{in}$ and $u_y(0, y) = 0$, then the unknown distributions given by f_1, f_5 and f_8 (in a D2Q9 system) can be found as

$$\sum_{i=0}^{8} f_i = \rho = f_0 + f_1 + f_2 + f_3 + f_4 + f_5 + f_6 + f_7 + f_8 \tag{3.36a}$$

$$\sum_{i=1}^{8} f_i e_{ix} = \rho u_{in}$$

$$\Rightarrow f_1 + f_5 + f_8 = \rho u_{in} + f_3 + f_6 + f_7$$

$$\Rightarrow \rho = \frac{1}{(1 - u_{in})} \left[f_0 + f_2 + f_4 + 2(f_3 + f_6 + f_7) \right] \tag{3.36b}$$

Also, from the bounceback of the non-equilibrium part of the distribution functions normal to the boundary,

$$f_1^{neq} = f_3^{neq}$$
$$\Rightarrow f_1 - f_1^{eq} = f_3 - f_3^{eq} \tag{3.37}$$

Thus solving equations 3.36 and 3.37, one can get

$$f_1 = f_3 + \frac{2}{3} \rho u_{in} \tag{3.38}$$

$$f_5 = f_7 + \frac{1}{2}(f_4 - f_2) + \frac{1}{6} \rho u_{in} \tag{3.39}$$

$$f_8 = f_6 - \frac{1}{2}(f_4 - f_2) + \frac{1}{6} \rho u_{in} \tag{3.40}$$

For the pressure boundary condition, a similar procedure is implied. Consider a node that lies on the right outlet. After streaming, the following distributions will be unknown: f_3, f_6 and f_7. Assuming that the density (pressure) at this boundary is known and the y-component of the velocity is zero (i.e. $\rho = \rho_{out}$ and $u_y(L_x, y) = 0$), the following equations can be written.

$$\sum_{i=0}^{8} f_i = \rho_{out} = f_0 + f_1 + f_2 + f_3 + f_4 + f_5 + f_6 + f_7 + f_8 \tag{3.41a}$$

$$\sum_{i=1}^{8} f_i e_{iy} = \rho_{out} u_y = 0 \tag{3.41b}$$
$$\Rightarrow f_6 - f_7 = f_4 + f_8 - (f_2 + f_5)$$

$$\sum_{i=1}^{8} f_i e_{ix} = \rho_{out} u_x$$
$$\Rightarrow f_3 + f_6 + f_7 = f_1 + f_5 + f_8 - \rho_{out} u_x$$

$$\Rightarrow u_x = -1 + \frac{f_0 + f_2 + f_4 + 2(f_1 + f_5 + f_8)}{\rho_{out}} \tag{3.41c}$$

Using the bounceback rule for the non-equilibrium part of the distribution function normal to the outlet,

$$f_3^{neq} = f_1^{neq} \tag{3.42}$$
$$\Rightarrow f_3 - f_3^{eq} = f_1 - f_1^{eq}$$

As done earlier, solving equations 3.41 and 3.42, one can get

$$f_3 = f_1 - \frac{2}{3} \rho_{out} u_x \tag{3.43}$$

$$f_6 = f_8 + \frac{1}{2}(f_4 - f_2) - \frac{1}{6} \rho_{out} u_x \tag{3.44}$$
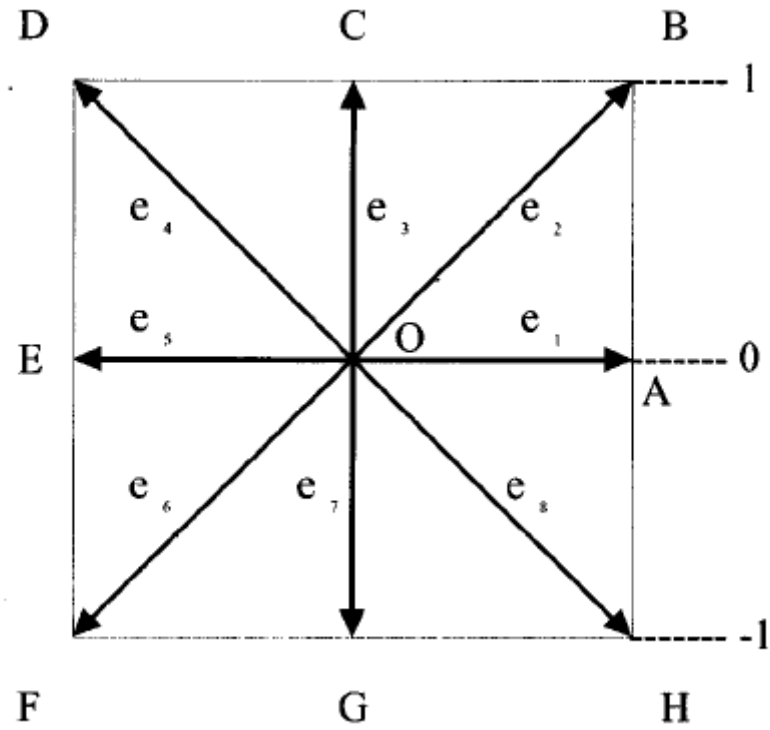
Figure 13: Basic cell for the '9 speed' lattice Boltzmann model. The center of the cell is occupied by the rest particle (after Chen et al (1996)).
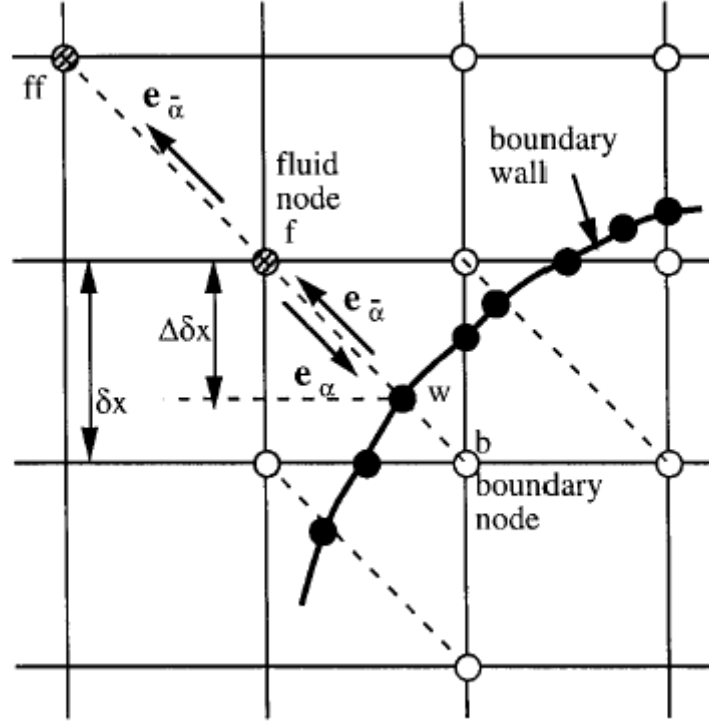
Figure 14: Layout for boundary conditions with curved boundaries (after Mei et al (1999)).
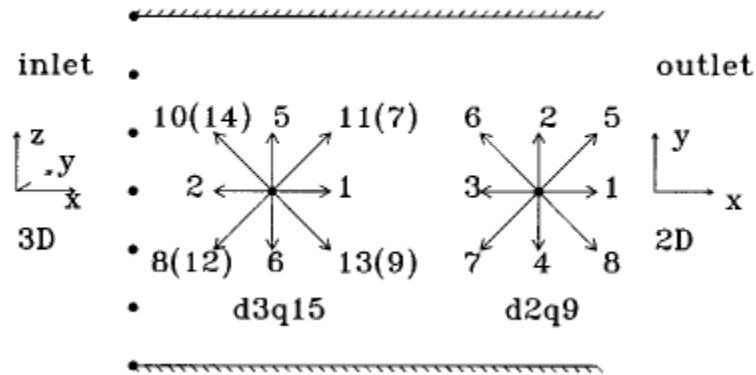
Figure 15: Schematic for velocity and pressure boundary conditions (after Zou and He (1997)).

$$f_7 = f_5 - \frac{1}{2}(f_4 - f_2) - \frac{1}{6}\rho_{out}u_x \qquad\qquad (3.45)$$

3.6 Multiphase Models in LBM

Numerous methods have been used by researchers over the past decade to conduct multiphase simulations using LBM. These include the model proposed by Rothman and Keller or better known as the R-K model (1988), where the two fluids are denoted by different colors. In this model, phase separation is produced by the repulsive interaction based on the color gradient. The R-K model was originally meant for lattice gas simulations (LGCA). Grunau et al (1993) introduced some free parameters in this model.

The lattice Boltzmann implementation was first introduced by Shan & Chen (1993). In Shan-Chen's (S-C) model, multiphase phases were simulated by introducing non-local interactions between particles at each lattice site, thereby making it hard to parallelize. Hou et al (1997) in one of the earliest works on multiphase LBM studied the chromodynamic (RK) and the pseudopotential (SC) models. Their simulations were done for a static bubble with the ideal equation of state and in a static medium. They showed that the pseudopotential model is a major improvement over the chromodynamic model. This static bubble test has since then been used as a benchmark for conducting multiphase simulations using LBM. Yang et al (2001) used the pseudopotential method for their LBM simulations and have qualitatively proved that results from LBM are very similar to experimental observations for saturated pool boiling. Sankaranarayanan et al (2002) proposed closures for drag and virtual mass terms that appear in two-fluid models through simulations performed using an implicit LBM. They also used the

pseudopotential method to model the liquid-vapor interaction. Gupta and Kumar (2008) have used the pseudo-potential method to conduct three-dimensional simulations of bubbles rising in a quiescent liquid, and calculate drag of a rising bubble for a range of Eotvos an Reynolds numbers.

Swift et al (1996) proposed the "free-energy" approach. In this model, unlike the S-C model, the local momentum conservation was satisfied. However, Swift's model suffered from the lack of Galilean invariance. Inamuro et al (2004b,c) used the projection method together with the free energy model to deal with immiscible fluids with large density ratios. In their work, they demonstrated the applicability of the algorithm developed for the case of droplet collisions surrounded by a lighter fluid. Takada et al (2001), in their work on bubble motion under gravity, developed a 3-D version of the binary fluid model that introduces a free energy function into the lattice Boltzmann equation (LBE). Their results showed that LBM is suitable for numerical analysis of bubble motion under gravity. Their simulations were conducted using a two-dimensional hexagonal lattice arrangement. They have also shown bubble migration towards the center of the channel for wall-driven shear flows. In more extended simulations, they demonstrate binary bubble coalescence and the stages involved in the process.

Recent work has been focused towards development of new methods that could simulate high density ratios for the liquid-vapor mixture. Inamuro et al (2004b) developed a multiphase model that could be used to simulate dissimilar fluids with large density difference and show its applicability by conducting droplet collision and bubbly flow simulations for a density ratio of

50. Although the large density contrast was an exciting development, the model suffers from time consuming iterations for solving the pressure field, which is given by a Poisson equation. In another work, Inamuro et al (2004a) conducted simulations for bubbly flows with large density ratios using the projection method. Kurtoglo and Lin (2006) used the phase-field method to assess its applicability to single bubble dynamics.

A more recent variant that modifies the R-K model and introduced an explicit specification of the surface tension parameter was given by Lishchuk et al (2003). This model enhanced the suitability of LBM as a tool to simulate multiphase flows due to its robust nature and reduction of spurious velocities, a phenomenon commonly encountered in the R-K and S-C model, by a great extent. Recently, Dupin et al (2006) have applied this method to simulate a flow-focusing microfluidic device, and show results that agree well with experimental results of Anna et al (2003). In the next sections, the S-C and Lishchuk's model are described, which have been used in this work to simulate and study bubbly flows, impingement of droplet on a dry surface, and formation of droplets in a microfluidic T-junction device.

3.6.1 S-C Model for Multiple Phases and Components

Shan & Chen (1993) in their work proposed a lattice Boltzmann based model that could simulate multiple phases and components. They incorporated non-local interactions amongst particles to simulate multiple component fluids. The interaction potential between components σ and $\bar{\sigma}$ was defined as

$$V(\mathbf{x}, \mathbf{x}') = G_{\sigma\bar{\sigma}}(\mathbf{x}, \mathbf{x}') \psi^{\sigma}(\mathbf{x}) \psi^{\bar{\sigma}}(\mathbf{x}') \qquad (3.46)$$

where $G_{\sigma\bar{\sigma}}(\mathbf{x},\mathbf{x}')$ is the Green's function. The quantity ψ^σ is the "effective mass". If only nearest neighbor interactions were considered, then

$$G_{\sigma\bar{\sigma}}(\mathbf{x},\mathbf{x}') = \begin{cases} 0 & ; \ |\mathbf{x}-\mathbf{x}'| > c \\ G_{\sigma\bar{\sigma}} & ; \ |\mathbf{x}-\mathbf{x}'| = c \end{cases} \tag{3.47}$$

The magnitude of $G_{\sigma\bar{\sigma}}$ controls the strength of the interaction between components σ and $\bar{\sigma}$, while its sign determines whether the interaction is attractive or repulsive.

This form of the potential gives the rate of net momentum change at each lattice site to be

$$\frac{d\mathbf{p}^\sigma}{dt}(\mathbf{x}) = -\psi^\sigma(\mathbf{x}) \sum_{\bar{\sigma}=1}^{S} G_{\sigma\bar{\sigma}} \sum_{a=0}^{b} \psi^{\bar{\sigma}}(\mathbf{x}+\mathbf{e}_a) \mathbf{e}_a \tag{3.48}$$

Therefore, this change in momentum is applied at each lattice site in the equilibrium distribution function before the collision, as shown by Buick and Greated (2000):

$$\rho^\sigma \mathbf{u}^\sigma = \rho^\sigma \mathbf{u} + \tau^\sigma \frac{d\mathbf{p}^\sigma}{dt}(\mathbf{x}) \tag{3.49a}$$

where

$$\rho^\sigma = m^\sigma f^\sigma(\mathbf{x}) \tag{3.49b}$$

is the mass density of the σth component and

$$\mathbf{u} = \frac{\displaystyle\sum_{\sigma}^{S} m^\sigma \sum_{a} f_a^\sigma \mathbf{e}_a / \tau^\sigma}{\displaystyle\sum_{\sigma}^{S} m^\sigma \sum_{a} f_a^\sigma / \tau^\sigma} \tag{3.49c}$$

and

$$f^{\sigma}(\mathbf{x}) = \sum_{a} f_{a}^{\sigma} \qquad \text{(3.49d)}$$

3.6.2 Lishchuk Model for Greatly Reduced Spurious Currents

In a recent and more robust scheme for the treatment of the interface, Lishchuk et al (2003) proposed an algorithm by which a two-fluid mixture is kept separated through a diffuse interface that spans a few lattice nodes. The location of the interface is controlled by a surface tension force which is incorporated such that the stress boundary condition and the continuity of velocity across the interfacial line are satisfied. This model begins with the elementary two-phase method of Gunstensen et al (1991). In the original method of Gunstensen, two particle distributions denote the two different fluids. Each fluid is assigned a 'color' (the use of the word 'color' is meant for identifying the fluid only) at all locations in the domain of interest. Each of these colored phases undergoes the collision and streaming operations, given as

$$f_i^{k,AC}(\mathbf{x},t) = f_i^{k}(\mathbf{x},t) - \frac{f_i^{k}(\mathbf{x},t) - f_i^{k,eq}(\mathbf{x},t)}{\tau^{k}} \qquad \text{(3.50)}$$

where k denotes the 'Red' or 'Blue' distribution. More so, the densities of each of the phases is given by

$$\rho_R = \sum_{i} f_i^{R}(\mathbf{x},t) \qquad \text{(3.51a)}$$

$$\rho_B = \sum_{i} f_i^{B}(\mathbf{x},t) \qquad \text{(3.51b)}$$

In addition to a collision operation given by the above mentioned equation, the particle distributions undergo a second collision (also known as the perturbation step),

$$f_i^{k}(\mathbf{x}+\mathbf{e}_i, t+1) = f_i^{k,AC}(\mathbf{x},t) + A|\mathbf{G}|\cos 2(\theta_i - \theta_f) \qquad \text{(3.52)}$$

63

where 'A' is a parameter related to the interfacial tension, θ_i is the polar angle of the lattice direction 'i', θ_f is the polar angle of the local color gradient **G**, which is calculated as

$$\mathbf{G}(\mathbf{x},t) = \sum_i w_i \mathbf{e}_i \left(\rho_R(\mathbf{x}+\mathbf{e}_i,t) - \rho_B(\mathbf{x}+\mathbf{e}_i,t) \right) \tag{3.53}$$

In order to prevent the numerical diffusion of the two fluids across the interface, a re-coloring step is required that enables to keep the interface sharp, and at the same time prevents mixing of the two fluids at the interface. The colored distributions are de-mixed by maximization of the work done by the color flux

$$\mathbf{q}(\mathbf{x},t) = \sum_i w_i \mathbf{e}_i \left(f_i^R(\mathbf{x},t) - f_i^B(\mathbf{x},t) \right) \tag{3.54}$$

The original model carries certain disadvantages which crucially underpins its applicability to study low Reynolds number flows. First, the re-coloring step is known to introduce lattice pinning, a phenomenon in which the interface can be stuck at a lattice node and is unable to conform to the physical motion of the dynamic interface, rendering the simulation ineffective. Secondly, the perturbation step has the side effect of introducing anisotropy and high spurious velocities at the interface, as shown by Wu et al (2008) and Lishchuk et al (2003).

The recent method of Lishchuk modified the original model to relieve the method of the perturbation step. In their work, this step is replaced with a direct forcing term at the sites where mixing of the two phases occurs. In order to impose the stress boundary condition and the continuity equation for the incompressible fluids, Lishchuk's model introduced a local pressure gradient throughout the interface, which is incorporated into the LBE at the collision step. This

force is defined such that it acts normal to the interface, centripetally and with a magnitude that is proportional to the gradient of the phase field, ρ^N, defined as

$$\rho^N(\mathbf{x},t) = \left(\frac{\rho^R(\mathbf{x},t) - \rho^B(\mathbf{x},t)}{\rho^R(\mathbf{x},t) + \rho^B(\mathbf{x},t)} \right) \tag{3.55}$$

Clearly, $-1 \leq \rho^N(\mathbf{x},t) \leq 1$. The local curvature at the 'mixed' locations on the interface is computed based on the normal vector computed at the particular lattice location. The normal vector, *n*, is defined as a function of the phase field, and is given by

$$\mathbf{n} = -\frac{\nabla \rho^N}{\left| \nabla \rho^N \right|} \tag{3.56}$$

Based on the local normal vector, the radius of curvature, *R*, of the interface is computed as

$$\kappa = \frac{1}{R} = -\nabla_S \cdot \mathbf{n} \tag{3.57}$$

where

κ is the curvature and

$$\nabla_S = (\mathbf{I} - \mathbf{nn}) \cdot \nabla \tag{3.58}$$

where *I* is the unit tensor and ∇_S is the surface gradient operator. In two-dimensions, the curvature can be simplified to

$$\kappa = n_x n_y \left(\frac{\partial n_y}{\partial x} + \frac{\partial n_x}{\partial y} \right) - n_x^2 \frac{\partial n_y}{\partial y} - n_y^2 \frac{\partial n_x}{\partial x} \tag{3.59a}$$

and in three-dimensions, the curvature is given as

$$\kappa = n_x n_y \left[\frac{\partial n_x}{\partial y} + \frac{\partial n_y}{\partial x} \right] + n_x n_z \left[\frac{\partial n_x}{\partial z} + \frac{\partial n_z}{\partial x} \right] + n_y n_z \left[\frac{\partial n_y}{\partial z} + \frac{\partial n_z}{\partial y} \right] - \left[n_y^2 + n_z^2 \right] \frac{\partial n_x}{\partial x}$$

$$- \left[n_x^2 + n_z^2 \right] \frac{\partial n_y}{\partial y} - \left[n_x^2 + n_y^2 \right] \frac{\partial n_z}{\partial z}$$

(3.59b)

Based on the curvature, the source term Φ_i is calculated such that it incorporates the surface tension force, and is given as

$$\Phi_i = \frac{w_i}{c_s^2} \mathbf{F}.\mathbf{e}_i$$

(3.60)

where

$$\mathbf{F}(\mathbf{x},t) = \frac{1}{2R} \sigma \nabla \rho^N$$

(3.61)

The partial derivatives of the components of the normal vector are computed based on a formulation for discretizing a general function ϕ on a regular lattice with contributions from the neighboring lattice sides,

$$\frac{\partial \phi}{\partial x} = \frac{1}{c_s^2} \sum_i \phi(\mathbf{x} + \mathbf{e}_i) e_{ix} w_i$$

(3.62a)

and

$$\frac{\partial \phi}{\partial y} = \frac{1}{c_s^2} \sum_i \phi(\mathbf{x} + \mathbf{e}_i) e_{iy} w_i$$

(3.62b)

3.7 Summary

In this chapter, the lattice Boltzmann equation was presented. The route from the discretized Boltzmann's equation to the incompressible form of the Navier-Stokes equation was also

illustrated. The key ideas regarding the numerical implementation of LBE and the methods of boundary conditions were laid out. This was followed by a discussion of the multiphase models of simulating two-phase flows in the existing literature, with their advantages and disadvantages listed as well. As a closing remark, two methodologies were presented that are the basis of further investigation of multiphase flows in the context of the present study.

CHAPTER FOUR: LBM FOR SINGLE-PHASE FLOWS

4.1 Introduction

Some of the test problems that were conducted to test the understanding of the lattice Boltzmann method are described in the next few sections of this Chapter. These include typical benchmark problems that have been solved using LBM for single-phase flows. These are: pressure driven flow in a channel (Poiseuille flow) using different treatments of the wall boundary conditions, for periodic and non-periodic boundary conditions, and flow in a lid-driven cavity using the extrapolation form of the wall boundary condition described in Chapter 3. Building on the foundation laid by these simulations, calibration of a three-dimensional T-junction microfluidic device is demonstrated with a single fluid passed through the two inlets and recording the pressure profiles along the length of the main channel.

4.2 Poiseuille Flow

Pressure driven flow in a rectangular channel is a problem that has an exact analytical solution. For a two-dimensional Poiseuille flow in between parallel plates separated by a distance 'h', the velocity profile at any location 'x' and along the vertical 'y' direction is given as

$$\mathbf{u} = \frac{h^2 \mathbf{G}}{2\upsilon} \frac{y}{h}\left(1 - \frac{y}{h}\right) \tag{4.1}$$

where G is the pressure gradient per unit density along the 'x' axis and 'h' is the height of the channel is lattice units.

In LBM, the described flow situation is simulated using various treatments for the wall boundary condition. A rectangular domain with grid points 101×51 was chosen. A pressure gradient of $G = 1 \times 10^{-5}$ (in non-dimensional units) was chosen as the driving force with a relaxation time of 1 ($\Rightarrow \upsilon = 1/6$) and periodic boundary conditions at the inlet and exit. Simulations were run for a time period until there was no appreciable change in the velocities at the outlet. Velocity profile obtained using the half-way bounceback boundary condition at the wall was compared and observed to match very well with the analytical solution derived for the same flow conditions, as is shown in figure 16. In addition to the half-way bounceback method, velocity profile was also calculated for the extrapolation scheme of Chen et al (1996), and the result is shown in figure 16. Clearly, the two methods of handling the zero velocity profile yield the same results and are in agreement with theory.

Simulations were also done to study a case in which the periodicity at the inlet and exit of the domain is replaced with finite pressure (density) values that would drive the same flow between the parallel plates. The pressure boundaries were enforced using the method proposed by Zou and He (1997). The results of such an exercise are shown and compared with the analytical profile in figure 17. For the sake of comparison, the velocity profile for a fully periodic boundary is also shown. The good agreement of a flow profile using a finite length of the plates (pressure boundary) as compared to an infinite long domain (periodic boundary) would be helpful in conducting simulations for creation of flow dispersions in a microchannel, to be discussed in Chapter 6.
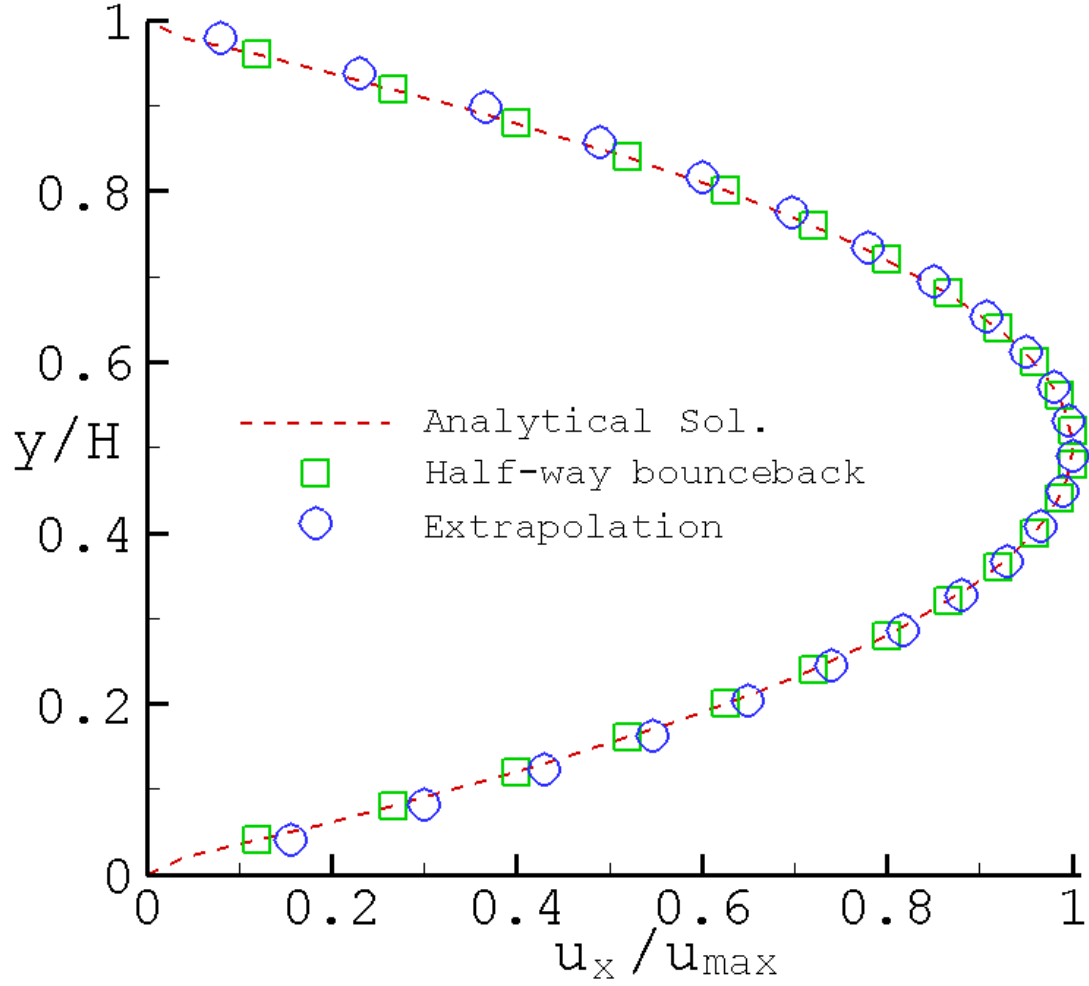
Figure 16: Poiseuille velocity profiles at the outlet computed using LBM for the half-way bounceback and extrapolation scheme compared with the analytical profile for $\dfrac{dp}{dx} = -1 \times 10^{-5}$ and τ=1.
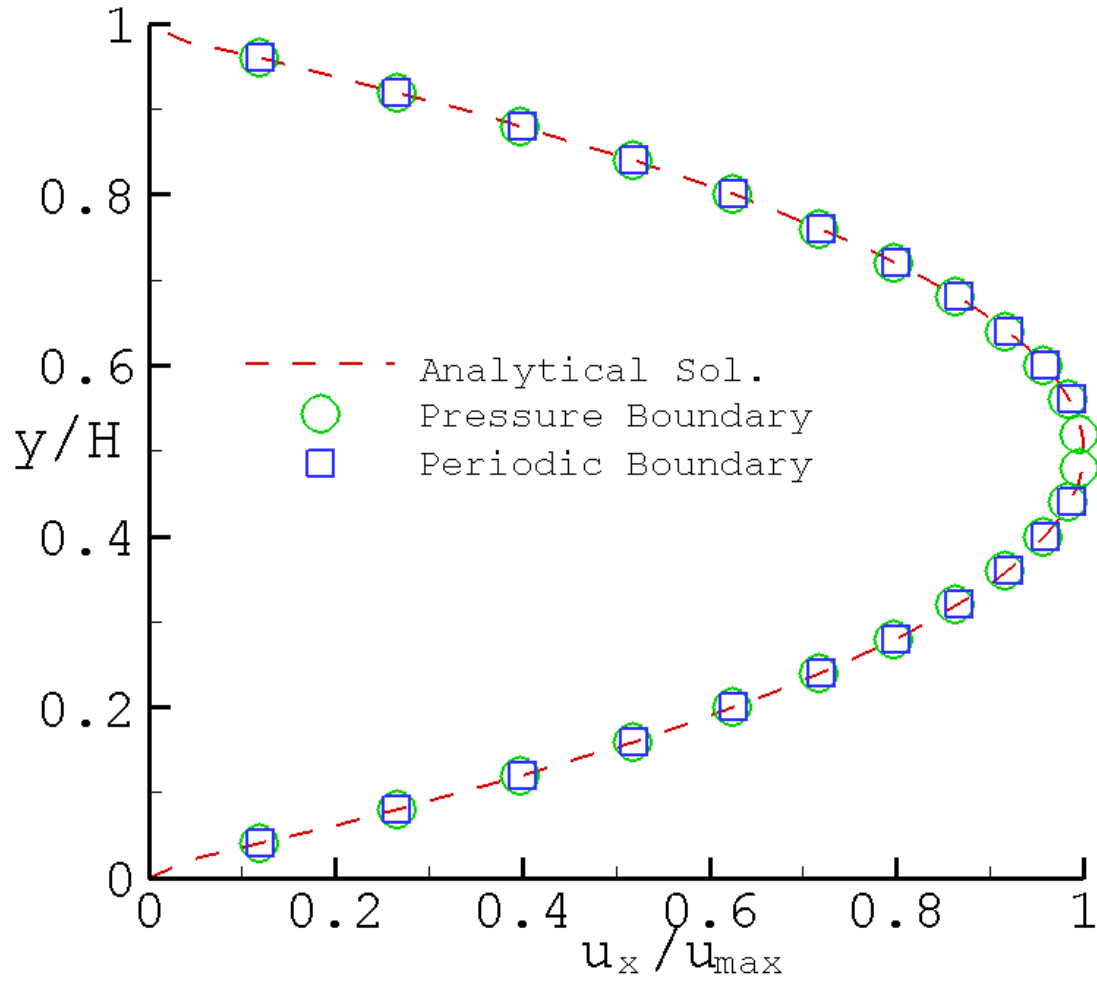
Figure 17: Comparison of horizontal velocity profiles using the periodic boundary and fixed pressure boundaries for $\dfrac{dp}{dx} = -1.0 \times 10^{-5}$ and $\tau = 1.0$.

4.3 Lid-Driven Cavity

To further check the applicability of LBM in simulations pertaining to incompressible single-phase flows, steady state simulations were done for a lid-driven cavity flow with the upper wall moving at a fixed velocity of U_w using the extrapolation method of enforcing stationary and moving walls. The extrapolation scheme proposed by Chen et al (1996) was used for all the walls (see section 2.3 for more details about this method) together with the explicit form of the LBE. This gave better accuracy for the flow field at smaller relaxation parameters as compared to the pure bounceback that yields accurate results only at relaxation time of close to 1. The Reynolds number of the cavity is defined as $\mathrm{Re} = \dfrac{U_w L}{\upsilon}$, where '$L$' is the characteristic dimension of the square cavity. A square grid of 167×167 nodes was used for the simulation that gives grid independent results. The driving lid was placed on top of the cavity and moves at a velocity of U_w=0.04 and 0.1 lattice units corresponding to $\mathrm{Re} = 100 \text{ and } 250$, respectively. The relaxation time was chosen to be 0.7 in order to simulate flow for both the Reynolds numbers. The streamlines inside the cavity at steady state are shown in figure 18 for (a) Re=100 and (b) Re=250. The flow behavior obtained is in good agreement with previous studies. The two recirculation zones (secondary vortices) at the bottom corners of the domain are captured very well with the present grid resolution, and are found to strengthen as Re increased from 100 to 250. In addition, the normalized horizontal velocities calculated at the vertical centerline of the cavity are compared for the Reynolds numbers simulated, and are compared in figure 19. The
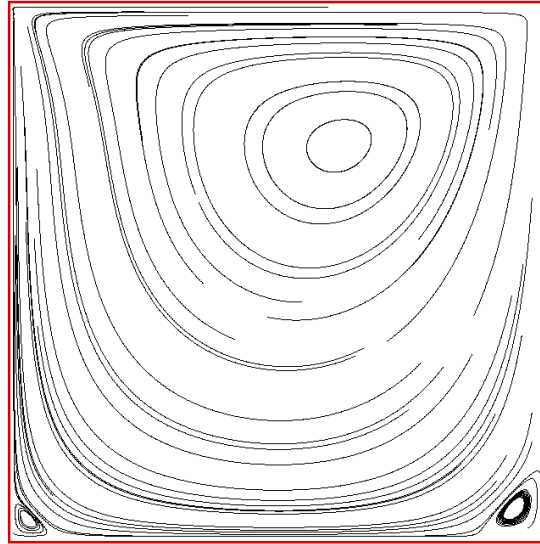
(a)
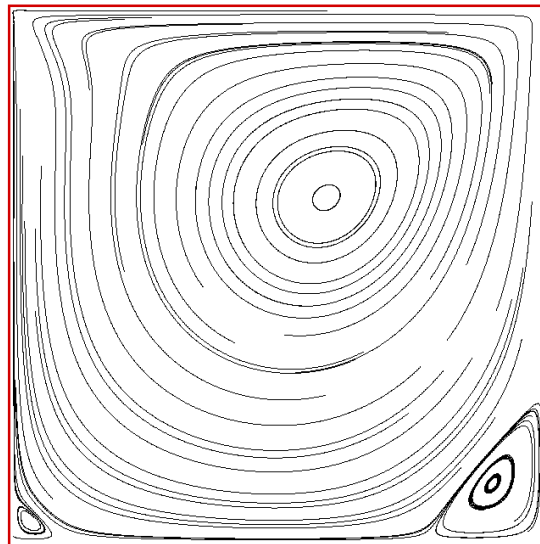
(b)

Figure 18: Streamlines for a 2-D lid-driven cavity simulation obtained using LBM at a Reynolds number of (a) 100 and (b) 250.
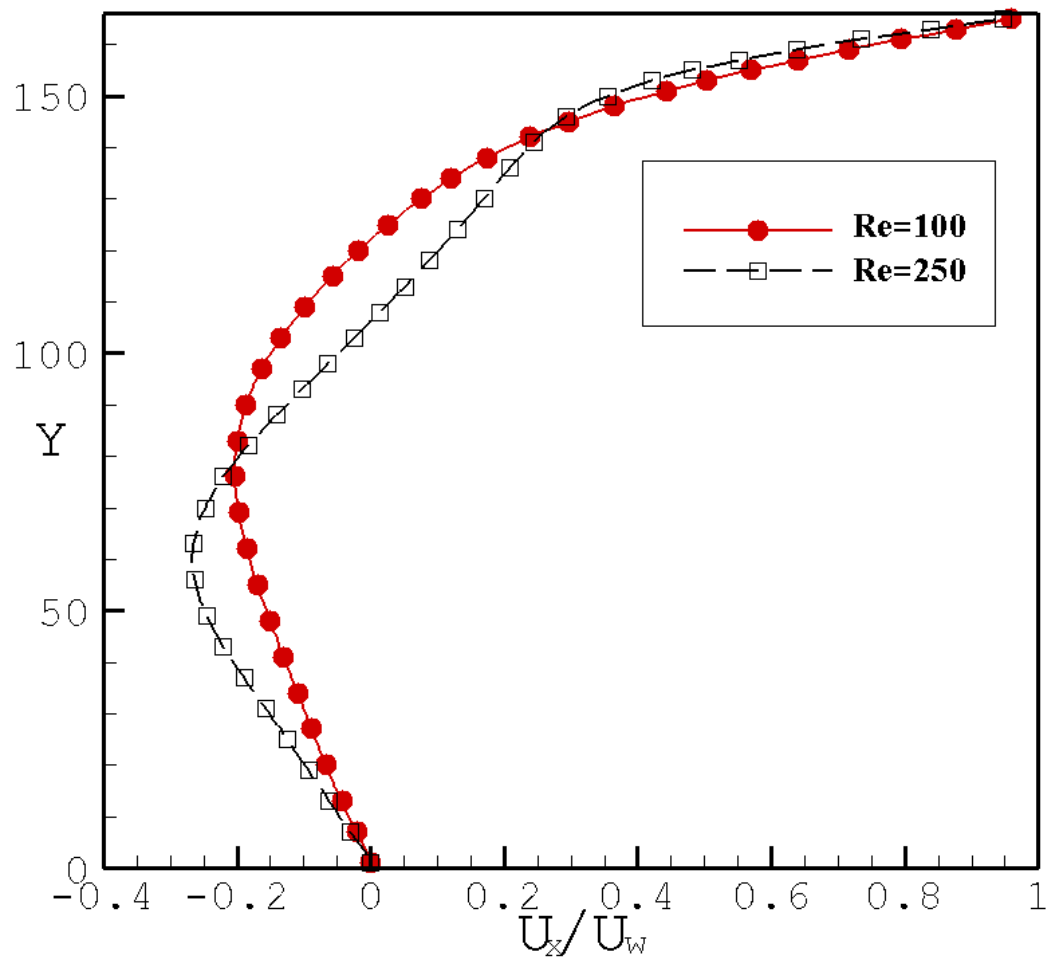
Figure 19: Normalized horizontal velocity as a function of the vertical coordinate for two different Re values plotted at the mid-plane corresponding to x=L/2.

simulation values are found to be in agreement with existing CFD simulations present in the literature.

4.4 Calibration of the T-junction

A sample T-junction channel was simulated for testing the geometry and the boundary conditions before proceeding with numerical experiments on a slightly more complex problem of the flow of dissimilar liquids in the proposed geometry. Figure 20 illustrates three-dimensional simulations of a single-phase fluid passing through the two inlets (denoted by Q_1 and Q_2) into the right side outlet. The channel number of grid points was chosen to be $201 \times 41 \times 11$ along the x, y and z axes, respectively. Fully developed velocity conditions were specified at both the inlets and the exit of the channel. The velocity profile imposed at each of these boundaries was specified based on the pressure gradient and the widths of the inlet section. The pressure at the right hand exit was kept fixed by imposing a particle distribution function based on the fully developed flow and constant density, i.e. $f_i^{out} = f_i^{eq}(\rho_0, \mathbf{u})$. The inlet pressure was allowed to build-up during the course of the simulation. At steady state, depending on the flow rate at the two inlets, the two inlet streams were found to mix and subsequently change the local pressure at the mouth of the T-junction, as shown by the velocity vectors in figure 20 for two different Reynolds numbers for face 2, keeping the Reynolds number for face 1 to be fixed at $\mathrm{Re}_1 = 0.16$. At steady state, the pressure profile along the horizontal center line passing through the mid-section of face 1 was recorded, and is shown in figure 21. For the two cases simulated, the inlet pressure at face 1 shows a higher jump when Re_2 was increased.

75

(a) $Re_2 = 0.1$

(b) $Re_2 = 0.26$
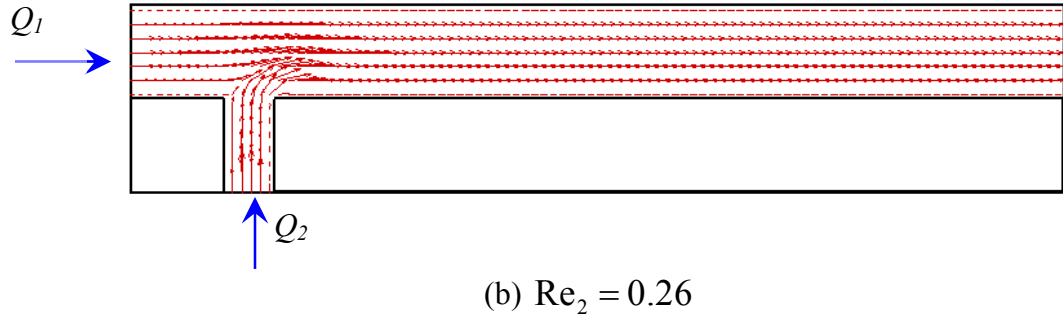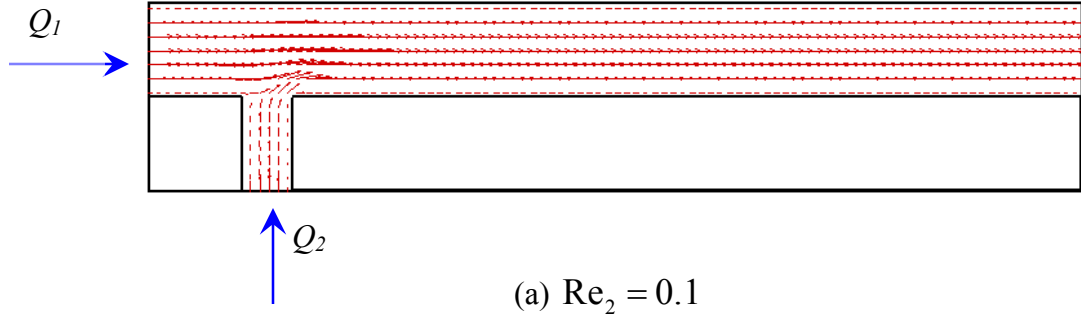
Figure 20: Velocity vectors for different flow rates of the bottom inlet channel. Reynolds number corresponding to Q_1 fixed at $Re_1 = 0.16$.
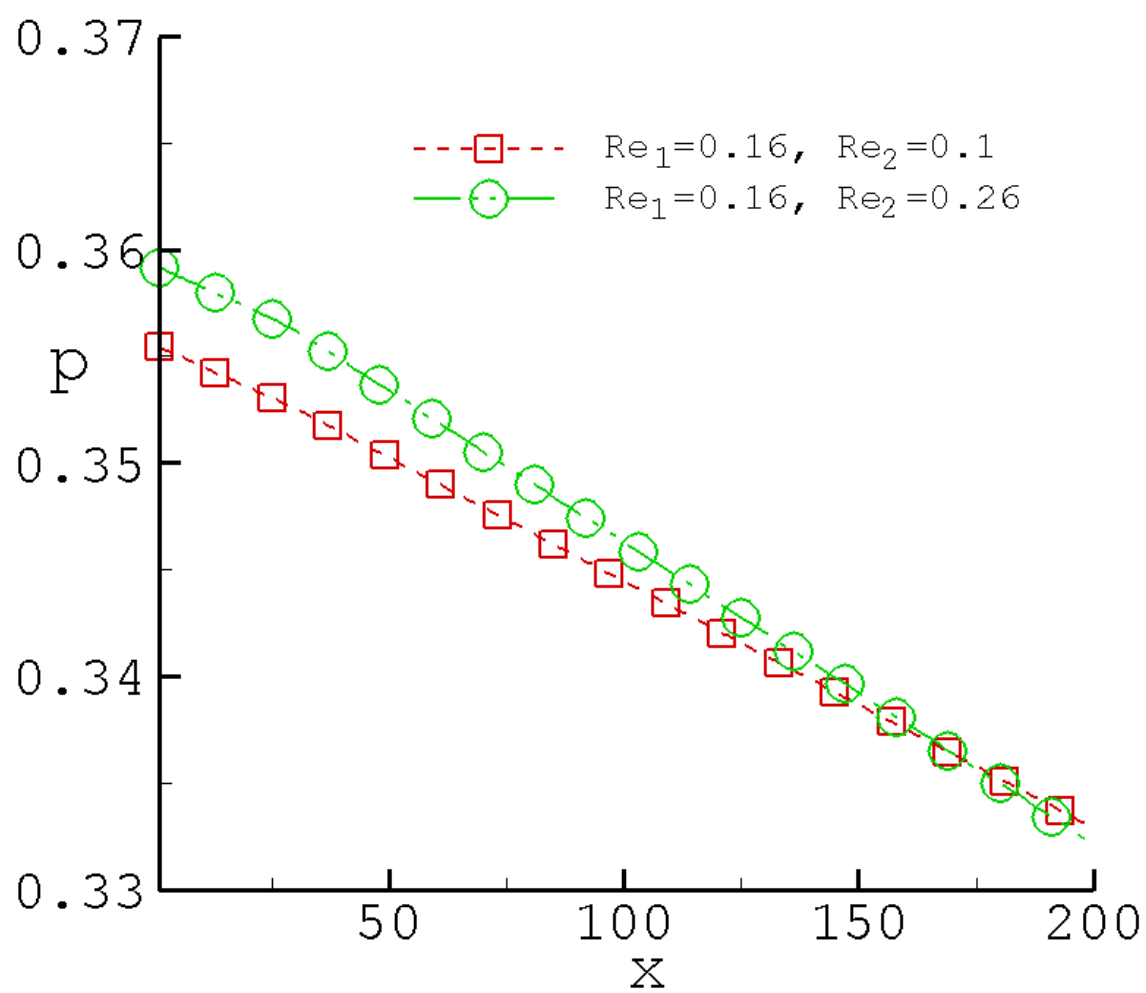
Figure 21: Pressure profile as a function of the grid location.

CHAPTER FIVE: LBM FOR TWO-PHASE FLOWS

5.1 Introduction

This chapter contains benchmark problems that have been solved using LBM for two-phase flows. These benchmark problems are: simulation of single and multiple bubbles in a periodic domain and droplet impingement on a dry surface. Computer codes were developed for all the problems and solved with appropriate form of boundary conditions.

5.2 Single Bubble Dynamics using LBM

Boiling and two-phase flow situations are of major importance in industrial applications. Micro- and mini-channels are very commonly used these days in residential air-conditioners and thin compact evaporators that are being used in automotive and aerospace industries. The flow topology in such channels needs to be understood well for development of mechanistic models. Although the two-fluid technology has progressed significantly, there is little precedence describing the interfacial forces, heat and mass transfer in difficult transition flow regimes. In the slug and churn-turbulent regimes, where all types of interfaces exist, it is difficult to develop continuum transport equations and closure models for each phase, in particular the vapor phase which exists in different forms and shapes. For example, a bubble can be spherical, distorted, confined and/or elongated. The behavior of bubbles and slugs in an infinite medium depends on several parameters such as Reynolds number ($\mathrm{Re} = U_b d_e / \upsilon$), Eotvos number ($Eo = g \Delta \rho d_e^2 / \sigma$), Morton number ($Mo = g \rho_L^2 \Delta \rho \upsilon^4 / \sigma^3$) and Weber number ($We = \rho_L^2 U_b^2 d_e / \sigma$). Fan and Tsuchiya

(1990) have described the importance and distinction between the Weber and the Reynolds number in a classical manner. The Weber number is a ratio of the dynamic pressure $\left(\sim \rho_L U_b^2\right)$ to the surface tension pressure $\left(\sim \sigma / d_e\right)$, whereas the Reynolds number is a ratio of the inertial force $\left(\sim \rho_L U_b^2 d_e^2\right)$ to the viscous force $\left(\sim \mu_L U_b d_e\right)$ from the surrounding liquid. The Weber number becomes even more important for $We \ll 1$, because for flows of this kind the bubbles maintain a spherical shape all throughout their life. These parameters have been used to record and observe bubble shapes and flow regimes. There are empirical correlations that exist for terminal velocity and drag coefficient in terms of these non-dimensional parameters, such as those given by Grace (1973), Bhaga and Weber (1981) and Kumar (2004).

In a previous study, Gupta (2007) conducted numerical simulations of bubbly flows to study the motion and dynamics of a single-isolated and multiple bubbles under buoyancy in fully periodic domains. Shan and Chen's (1993) model for multiphase flows was adopted as the simulations involve a mixture of fluids with a density ratio of $O(1)$, and the particular method is found to be computationally efficient for such cases. The gravitational force is directed in the negative vertical direction. Sanakaranarayanan et al (2002) have suggested that this external force can be introduced into the force equation using the expression

$$\mathbf{a}_{ext} = \mathbf{g}\left(1 - \frac{\langle \rho \rangle}{\rho}\right) \tag{5.1}$$

where ρ is the mixture number density at the node of interest and $\langle \rho \rangle$ is the average number density of the mixture in the entire domain. This choice ensures that the average value of the

external force is zero in the periodic domain, and hence the mass-average velocity of the mixture is constant. For all the liquid-vapor simulations described below, $\tau=1$. Figure 22 shows bubble snapshots at different instants of time as the bubble shape evolves under the influence of gravity. Liquid to vapor density ratio was 2.66. The interaction strengths for the gas-gas, liquid-liquid and liquid-gas interactions were taken to be $g_{11} = 0, g_{22} = -0.3, g_{12} = 0.15$ respectively. The simulation was done at $Eo = 10.7$ and $Mo = 2.38 \times 10^{-3}$. At this Eotvos number, the bubble shape changes from a sphere to an ellipse. The bubble forms an oblate ellipsoidal shape as has been discussed by Bhaga & Weber (1981), who conducted experiments to study wake behavior behind moving bubbles with hydrogen bubble tracer technique.

Figure 23 shows the well-known bubble shape regime map constructed by Grace (1973) using flow visualization of hydrogen gas bubbles. For various Re and Eo, the bubbles were characterized as spherical (s), oblate ellipsoid (oe), oblate ellipsoidal disk-like (oed), oblate ellipsoid cap (oec); spherical cap with closed wake (scc), and skirted (sks). Six representative results obtained using LBM are plotted along with Grace's (1973) regime map in figure 23. The comparison shows that the current numerical simulation using LBM yields excellent quantitative and qualitative results for single bubble simulations. In addition, it was shown that the drag coefficient for single bubbles rising in two- and three-dimensional periodic domains matches with the correlations of Bhaga and Weber (1981) and the theoretical solution of Joseph (2003).
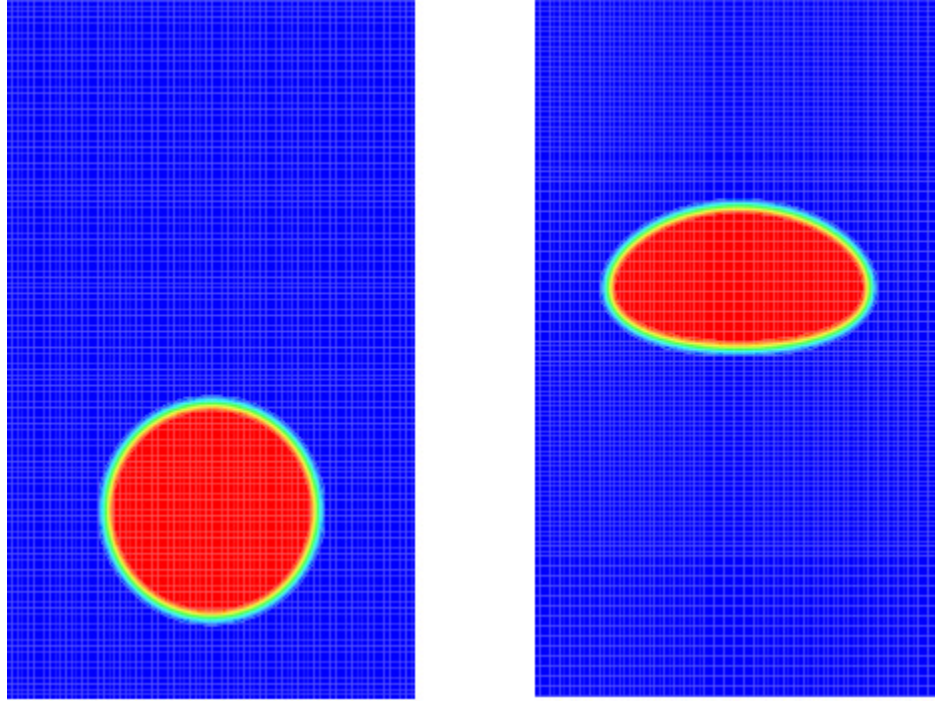
Figure 22: Bubble shape evolution under gravity at an Eotvos number of 10.7. The time instants are at (a) initial condition, and (b) time=3000 timesteps. Red depicts the lighter vapor and blue denotes the heavier liquid surrounding the bubble.
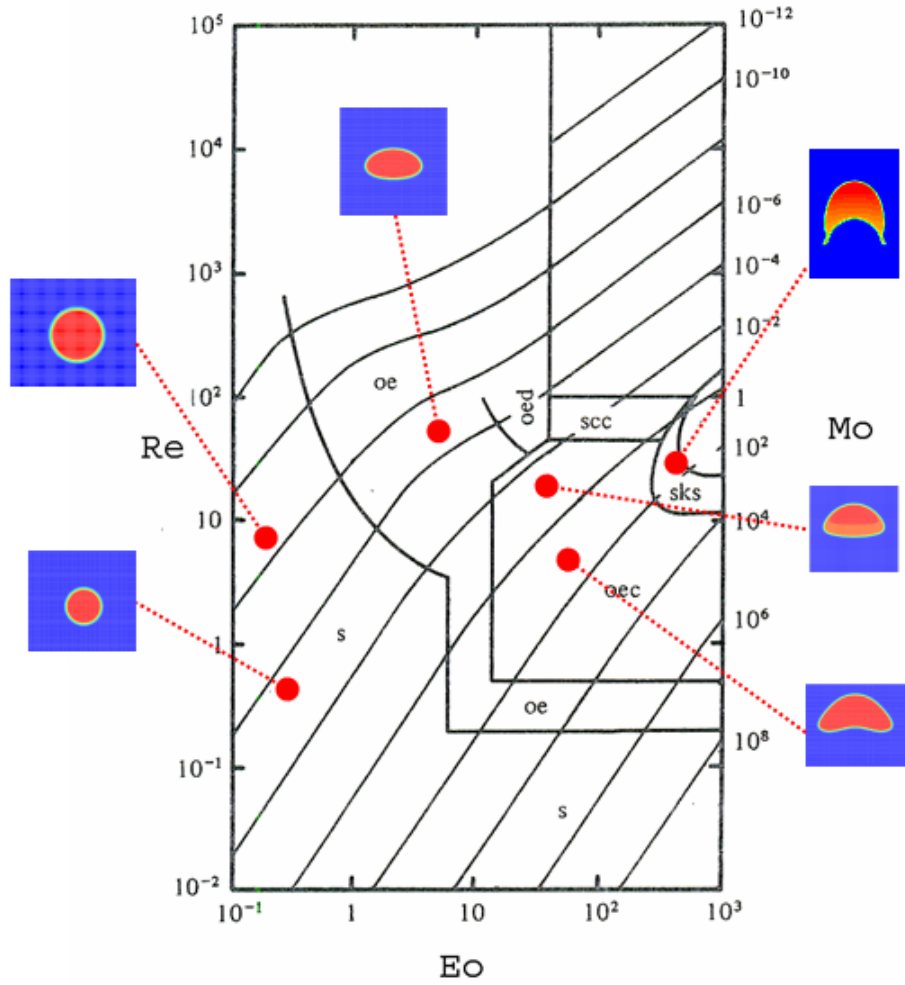
Figure 23: Shape regime map for isolated bubbles in liquids taken from Bhaga & Weber (1981). The pictures in the inset show the results of the numerical simulations using LBM; s, spherical; oe, oblate ellipsoidal; oed, oblate ellipsoidal disk-like and wobbling; oec, oblate ellipsoid cap; scc, spherical cap with closed wake,; sks, skirted with smooth steady wake.

5.3 Multiple Bubble Dynamics using LBM

Esmaeeli and Tryggvason (1998,1999) conducted two- and three-dimensional simulations of buoyant bubbles in periodic domains for a range of low to moderate Reynolds numbers using their hybrid method. They found that a regular array of (slightly perturbed) bubbles is an unstable configuration that eventually leads to an asymmetrical arrangement. Therefore, three-dimensional simulations were conducted for an inline arrangement of bubbles without any initial random perturbation in the lateral positions. Multiple bubbles were simulated in large periodic domains and bubble coalescence characteristics studied for different initial sizes of the bubbles. Figures 24 and 25 show two such cases in which the current methodology has been used to study bubble coalescence. Figure 24 shows the time variation of the Reynolds number, based on the initial diameter of the bubbles, for an Eo=4.26 and figure 25 is at Eo=35.93, where t^* is the non-dimensional time given by $t^* = t / \sqrt{d/g}$. The preliminary cases were run with two bubbles, whose line connecting the centers is parallel to the gravitational vector.

One of the objectives was to study the influence of the coalescence of the bubbles on the variation in the bubble rise velocity, recorded through the Reynolds number based on the initial bubble diameter. Coalescence occurs due to a non-zero relative velocity of the lower bubble as it rises opposite the gravity. The upper bubble flows 'through' the quiescent liquid, while the lower one is traveling 'into' the wake left behind the upper bubble. Thus, the wake left behind by the upper bubble results in lower drag for the lower bubble. Since the relative velocity of the bubbles is non-zero, the distance between the two bubbles keeps decreasing with time. Eventually the

bubbles touch/collide (see insets of figure 24 & 25), and soon after form a larger bubble with twice the volume as the initial bubble. The shape of the intermediate larger bubble, at the time when the thin liquid film separating the two bubbles has just ruptured, is different for the two cases shown, thereby indicating that bubble coalescence and behavior is a function of the Eotvos number and is not the same for all situations. Eventually at steady state, the bubble shapes for the two cases are found to be much different as was expected.

Simulations were also done for cases with three bubbles of equal size that were initially placed in a staggered arrangement. This was done to study how the wakes behind the bubbles affect the motion of the downstream bubbles and the bubble rise velocity. The three bubbles were staggered by a lateral distance of the order of the initial diameter of the bubble with respect to the gravitational vector. The Eotvos number of the flow was set at Eo=4.02. It was observed that as the bubbles rise, the wake behind the upper bubble(s) creates an artificial lift force for the downstream bubble(s), thereby causing them to move in a helical path, as shown by the bubbles shapes in figure 26. The effect of the lift force is such that the bubble shapes are no more oblate elliptical, rather change to oval-like. These oval bubbles seem to follow each other, into the wake left by the upstream vapor. Eventually the bubbles coalesce and the shape of the coalesced bubble is shown (inset of figure 26). An observation common to all the cases discussed so far, as can be noticed from the plots of Reynolds number with time, is that the momentum associated with the dispersed phase reaches a maximum when the bubbles start to coalesce. To study the rise velocity characteristics of bubbles and to avoid coalescence (which is a numerical
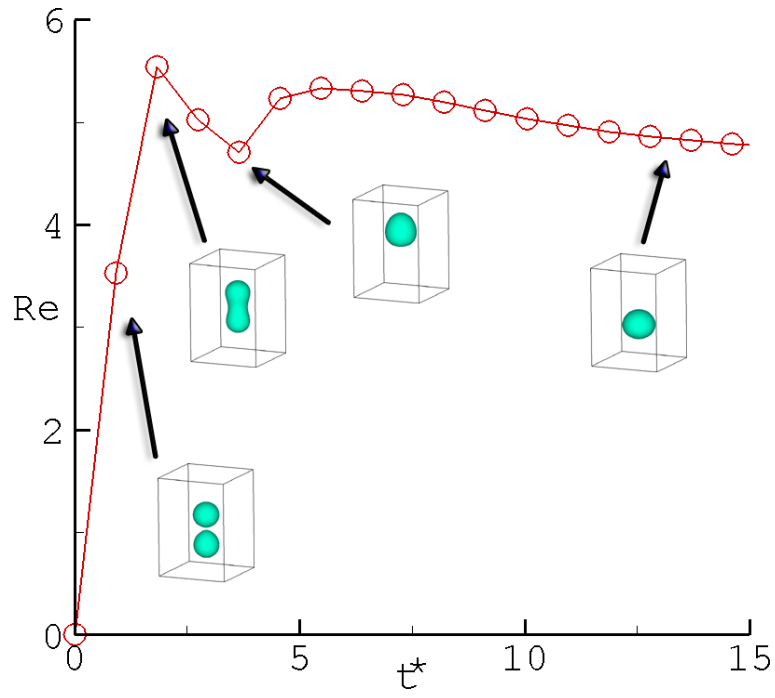
Figure 24: Simulation of two bubbles in a periodic domain for Eo=4.26.
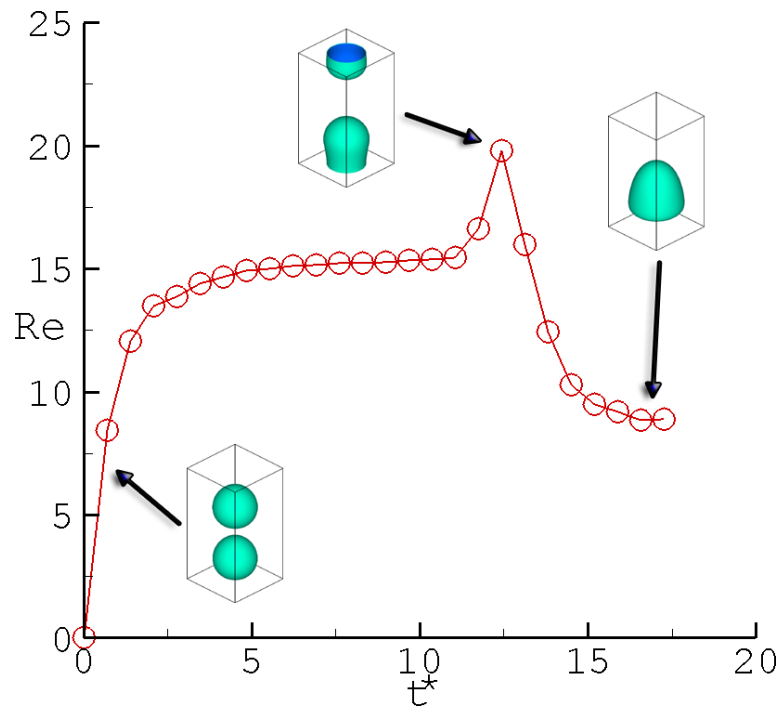
Figure 25: Simulation of two bubbles in a periodic domain for Eo=35.93.
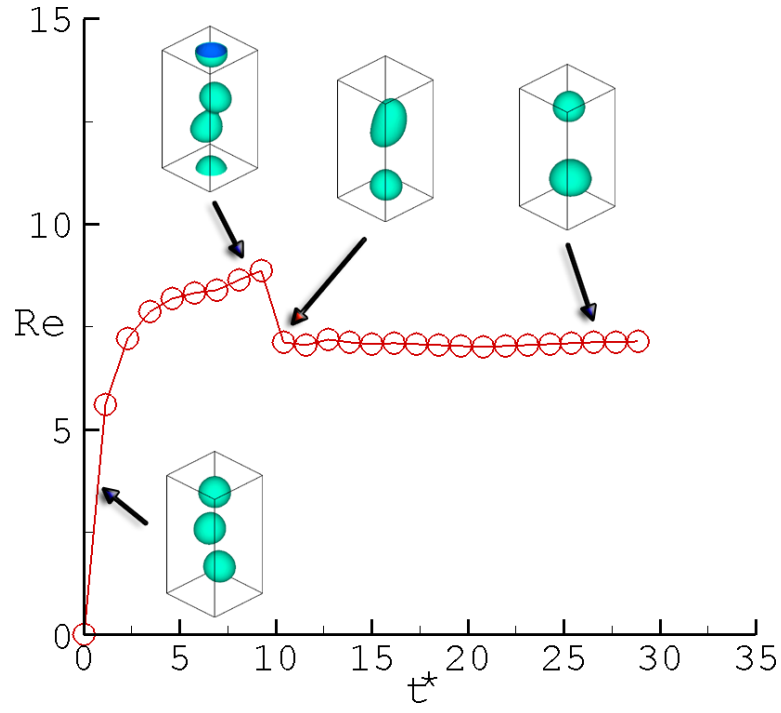
Figure 26: Simulation of three bubbles placed in a staggered arrangement for Eo=4.02.
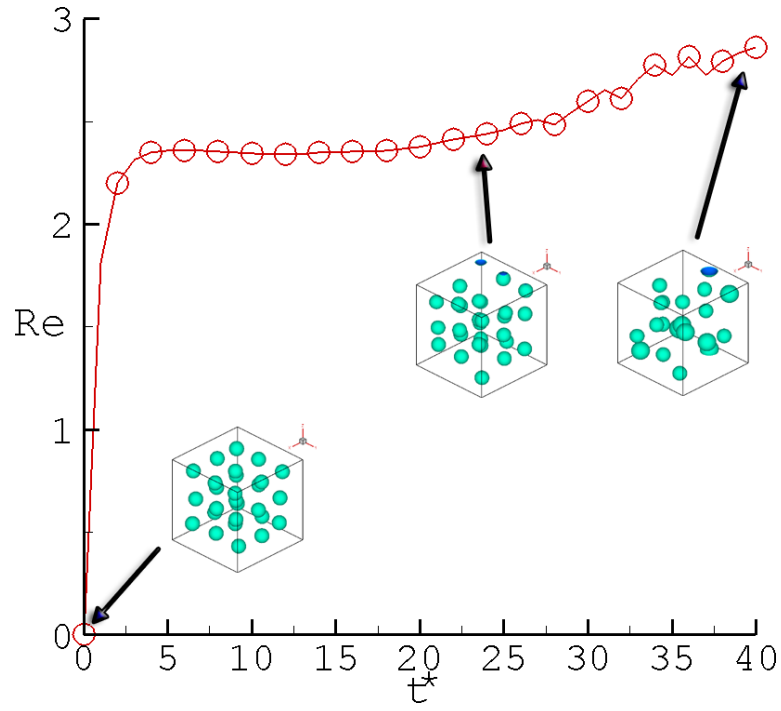
Figure 27: Simulation of 27 bubbles perturbed from the inline arrangement for Eo=1.37.

consequence and is unavoidable with the choice of the model used), a simulation with 27 bubbles of equal size but slightly perturbed from the inline arrangement was carried out, and the results are shown in figure 27. The Eotvos number was fixed at Eo=1.37, which was low enough to ensure that the bubbles remain nearly spherical for the duration of the simulation. It can be observed from the plot of Re vs time that the rise velocity attains a nearly steady value until $t^* \approx 25$, after which the instability caused by the motion of rapidly rising bubbles leads to a deviation from the plateau and the Reynolds number rises with large perturbations in the velocity of the bubbles.

5.4 Droplet Impingement on a Dry Surface

Collision of droplet(s) on solid or liquid surfaces is a phenomenon that occurs widely in nature. Droplet impact dynamics is an area which has long been an area of interest. Impact of drops on solid surfaces is a very common phenomenon in many modern engineering applications ranging from ink-jet printing to spray cooling, internal combustion engines to spray painting and plasma spraying, and more recently in microfabrication and microchannels (Yarin (2006)). In high pressure applications such as in nuclear reactors, the liquid to vapor density ratio is less than 10 at 2.4 MPa. When these liquid droplets hit a solid surface, the accompanying physical behavior is observed to be very different, depending upon whether the surface is hydrophobic or hydrophilic, rough or smooth and whether it is dry or wet. The final shape and spreading of the liquid drop also depends on a range of parameters, like the impact velocity, the size of the droplet, the angle of attack to the surface, the physical properties of the liquid drop and the surrounding pressure.

Experimental investigations have been carried out extensively to study the mechanism of droplet impact and the subsequent spreading process on a dry surface (Wachters and Westerling (1966), Stow and Hadfield (1981), Yarin and Weiss (1995)). These studies show the formation of a watersheet as well as the subsequent breakup into daughter droplets. The difference in the dynamics of a single drop impact with a dry wall as compared to that of a train of drops has also been demonstrated by Yarin and Weiss (1995). In a detailed experimental study by Rioboo et al (2002), it was shown that for the case of water drops impacting a wax surface, the perturbations during the receding process merge continuously leading to a rebound of the droplet from the surface. For the case where there is no rebound of the liquid film from the surface, the spreading diameter may stay constant or increase depending upon the wettability of the surface used. In a separate study by Scheller and Bousfield (1995), it was shown that the maximum spread factor follows the correlation given by $\xi_{max} = 0.61\left(\mathrm{Re}^2\,\mathrm{Oh}\right)^{0.166}$, and that the contact angle effect on the spreading diameter is negligible for droplet Re>10.

Simulations of droplet splashing phenomenon have mostly focused on impact dynamics on a wet surface with a thin liquid film (Morton et al (2000), Josserand and Zaleski (2003)), deposition/splashing behavior of impact of single drop on a wet surface (Mukherjee and Abraham (2007a,b), Lee and Lin (2005)) and the study of droplet spreading behavior for very low Oh and subsequent rebound on a dry surface for low density ratios (Mukherjee and Abraham (2007c)). However, an analytical investigation of the droplet spreading behavior in high pressure systems at early times of impact and droplet breakup at later times has not been carried out so far. Through lattice Boltzmann simulations, we illustrate the mechanism of droplet collision on a

dry surface during all phases of impact and to develop criteria for breakup. In addition, the effect of the interactions between the fluid and hydrophobic and hydrophilic surfaces and their influence on the breakup will be studied.

Since the proposed work is to understand the droplet interactions at high pressures and low density ratios, SC model has been used. The net force due to surface tension-based interactions at each lattice site is incorporated as

$$\mathbf{F}_{\text{int}}^{\sigma}(\mathbf{x}) = -\psi^{\sigma}(\mathbf{x}) \sum_{\bar{\sigma}=1}^{S} G_{\sigma\bar{\sigma}} \sum_{a=0}^{b} \psi^{\bar{\sigma}}(\mathbf{x} + \mathbf{e}_a) \mathbf{e}_a \tag{5.2}$$

Similarly, at the solid-fluid interface, a force as proposed by Martys and Chen (1996) can be incorporated. This form of the interaction can be written as

$$\mathbf{F}_{\text{wall}}^{\sigma}(\mathbf{x}) = -\rho^{\sigma}(\mathbf{x}) \sum_{a=0}^{b} G_{w,\sigma} \, \rho^{\bar{\sigma}}(\mathbf{x} + \mathbf{e}_a) \mathbf{e}_a \tag{5.3}$$

where the interaction parameter $G_{w,\sigma}$ denotes the intensity of interaction from the wall and the sign (positive/negative) indicates whether the interaction is repulsive/attractive (non-wetting/wetting). For the D3Q19 lattice used in this work,

$$G_{w,\sigma}(\mathbf{x}, \mathbf{x}') = \begin{cases} G_w & ; \; |\mathbf{x} - \mathbf{x}'| = 1 \\ G_w/2 & ; \; |\mathbf{x} - \mathbf{x}'| = \sqrt{2} \\ 0 & ; \; \text{otherwise.} \end{cases} \tag{5.4}$$

The external force is directed in the negative vertical direction as shown in equation 5.1. The total force on each component at each lattice site can thus be found as

$$\mathbf{F}_{tot}^{\sigma} = \mathbf{F}_{int}^{\sigma} + \mathbf{F}_{wall}^{\sigma} + \mathbf{F}_{ext}^{\sigma} \qquad (5.5)$$

This change in momentum is applied at each lattice site in the equilibrium distribution function before the collision.

Multiphase simulations of droplet impact on a wall were started by conducting static droplet tests to generate a good initial condition with one (or more) droplet in a channel in which the top and bottom boundaries are walls and the side boundaries are periodic. Changing the boundary condition criteria on the upper boundary of the domain to a free-slip layer from the no-slip condition did not yield significantly different results presented herein. The nearest neighbor SC model as explained by Yuan and Schaefer (2006) has been used in which the next-nearest neighbor is also used in the force discretization. This leads to a non-ideal equation of state for the liquid that is given as

$$p = c_S^2 \rho + 3g\Psi^2(\rho) \qquad (5.6)$$

It should be noted here that if there is no interaction amongst the same kind of fluid, then the equation of state would reduce to the ideal gas equation of state given by $p = c_S^2 \rho$. The 'effective mass' function, Ψ, is given by Shan and Chen (1993),

$$\Psi(\rho) = \rho_0 \left[1 - \exp(-\rho / \rho_0) \right] \qquad (5.7)$$

In this study, the values of this fluid-fluid interaction parameter are selected in a way that a particular density ratio and a specific Weber number can be achieved. A low value of the

interaction strength would result in a higher density ratio. In the simulation results described below, $\rho_0 = 10$. The computational domain is divided into $120 \times 120 \times 120$ lattice points which was tested to be adequate to resolve the thin films on the wall.

Droplet impact and the dynamics depend on Weber number, We, and Reynolds number, Re. One other parameter that is very important in drop impact on dry surfaces is the spreading film diameter. This quantity is usually represented in terms of the spread factor given by the ratio of the diameter of the film and the diameter of the droplet, ξ=d/D. The fluid-interaction parameter was varied between -0.024 to -0.027, and the corresponding density ratio in the simulations ranged from 4 and 10. The suspended droplet was equilibrated for a sufficient amount of time, after which it was allowed to fall in the downward direction towards the solid surface. The time evolution of the spread factor is provided in figure 28 for a ratio of 6 at Re=21.5 and We=20.4. The time evolution can be divided into four phases, (a) the kinematic phase, (b) the spreading phase, (c) relaxation phase, and (d) equilibrium phase. It has been shown previously by Rioboo et al (2002) that the film diameter increases as $\xi \propto \sqrt{t^*}$ in the kinematic phase. As the spreading phase begins, other parameters such as the diameter of the impacting droplet, the velocity, the surface tension and viscosity can start to influence the rate at which the lamella spreads. During the later stage of this phase, surface tension effects can play a prominent role in undermining the maximum spread the film can achieve. In the relaxation phase, the film diameter may begin to recede depending on the surface roughness and the impact velocity, before reaching the equilibrium phase where ξ reaches a constant. In the next few sections, the role of these physical

properties and their influence on the spreading and breakup behavior of liquid droplets in a low density environment are discussed.

5.4.1 Spreading of a Liquid Droplet

The spreading diameter was calculated based on the number of lattice points that are in contact with the heavier fluid at the wall. In the kinematic phase the contact line corresponds to the circumference of a horizontal cut through the drop moving with a downward velocity of V_0 (Rioboo et al (2002)). Assuming that the diameter of the drop after the impact is still the same, a simple expression can be obtained in the kinematic phase ($t^* \ll 1$) for the spread factor as $\xi = d/D = 2t^{*1/2}$ where $t^* = tV_0/D$. This expression was validated for different We and Re using LBM as shown in figure 29. A curve fit was generated to yield $d/D = 1.35t^{*0.5}$. A similar expression was also obtained in the experiments of Rioboo with a coefficient of 2.8. In the current simulation, it was also found that changing the wettability of the surface did not lead to different results in the kinematic phase of the spreading mechanism.

The kinematic phase is followed by the spreading phase in which the impact velocity, drop diameter and the surface tension determine the maximum spreading diameter. A comparison for the maximum spread factor from the 3D LBM simulations with experimental data of Scheller and Bousfield (1995) and Asai et al (1993) is shown in figure 30. The experimental results of Scheller and Bousfield show that the maximum spreading diameter is better correlated with the parameters, Reynolds number and Ohnesorge number. Ohnesorge number is given by $\mu/(\rho\sigma D)^{1/2} = We^{1/2}/\mathrm{Re}$ which is dependent on only the fluid properties.
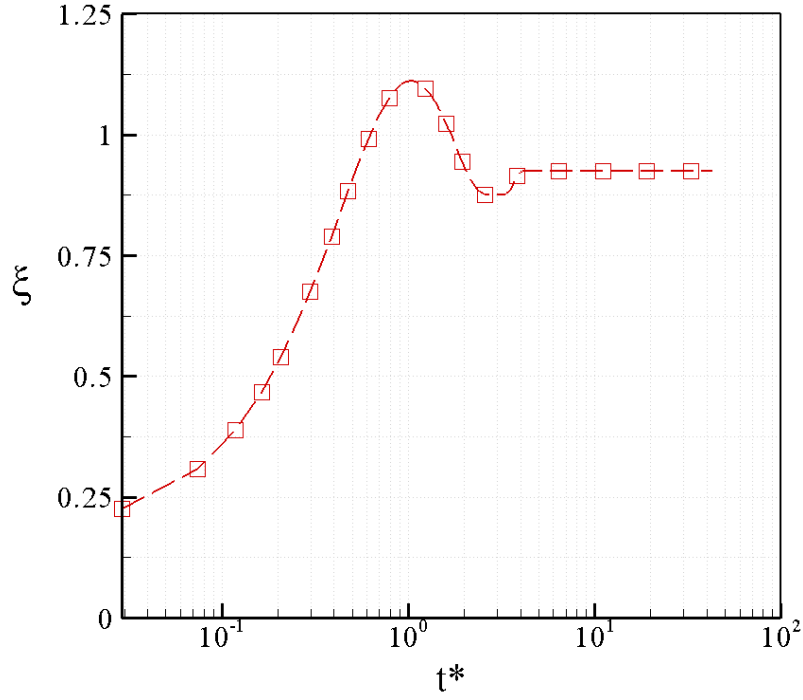
Figure 28: Spreading behavior from the the current LBM simulations showing the four phases of droplet impact dynamics at We=20.4 and Re=21.5 at a density ratio of 6.
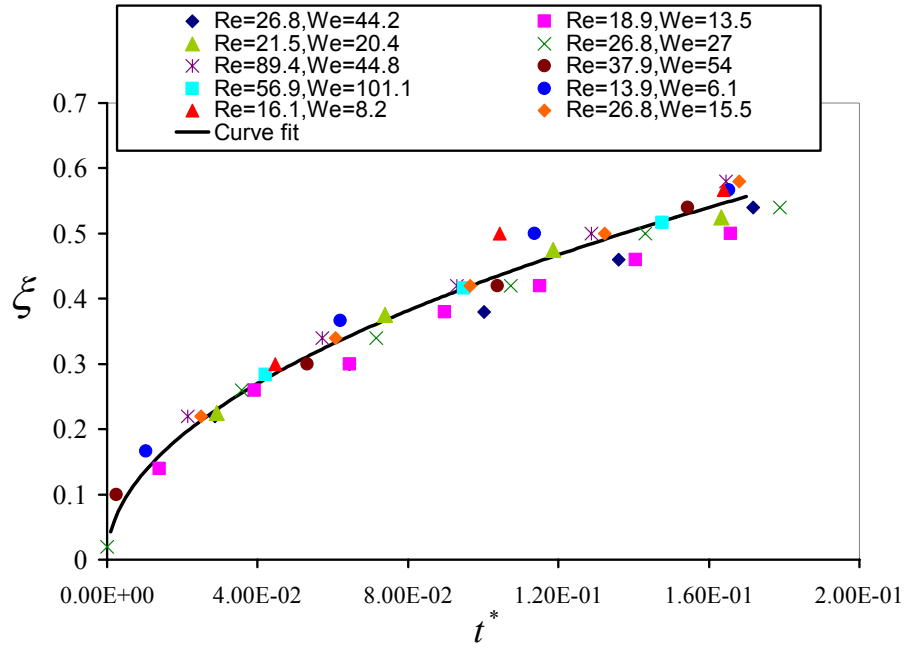
Figure 29: Variation of the instantaneous spread factor with time in the initial phase of a three-dimensional drop impact on the dry solid surface. The solid line indicates the curve fit $d/D=1.35t^{*0.5}$.
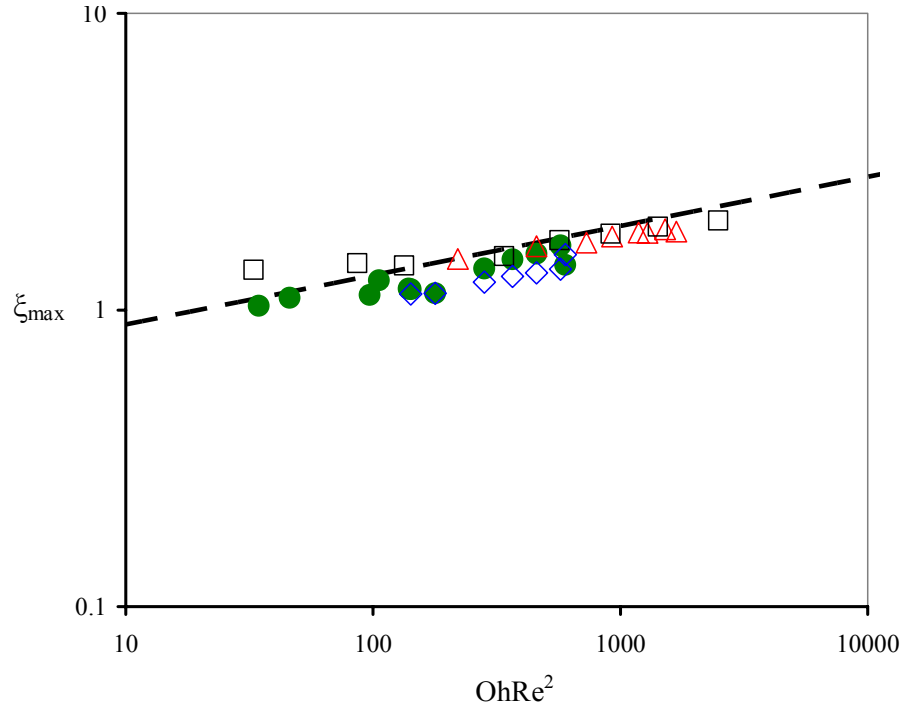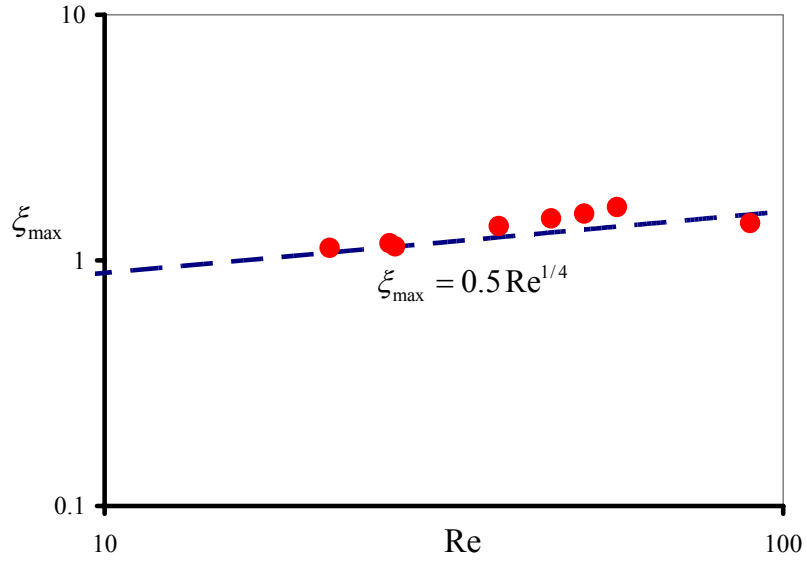
Figure 30: (a) Comparison of LBM simulation results (●) with (a) experiments and correlation of Scheller (---, Δ), Asai (□) and correlation of Pasandideh-Fard (◊). (b) Comparison of LBM (●) with the analytical solution of Pasandideh-Fard (--).

Current numerical results are also compared with the correlation proposed by Scheller (figure 30a), and with the analytical expression proposed by Pasandideh-Fard et al (1996), given as $\xi_{max} = 0.5\,\mathrm{Re}^{0.25}$ which is applicable for We>12 and $\mathrm{Re}^{1/2}$<<We (figure 30b). The simulation results from LBM match well with these studies.

5.4.2 Droplet Breakup Analysis

At higher Weber and Reynolds numbers, an impinging droplet can breakup into smaller drops. The dependence of this breakup behavior although may depend on the above mentioned parameters, its dependence on the surface wettability and the manner of the dissipation of the impact kinetic energy is not well understood. By the principle of conservation of energy of the liquid drop before and after impact, we can write

$$E_{KE}^{i} + E_{PE}^{i} + E_{SE}^{i} = E_{KE}^{f} + E_{PE}^{f} + E_{SE}^{f} + E_{D}^{f} \tag{5.8}$$

where E_{KE}^{i}, E_{PE}^{i} and E_{SE}^{i} are the kinetic, potential and surface energies before the impact of the liquid drop with the solid, and E_{KE}^{f}, E_{PE}^{f}, E_{SE}^{f} and E_{D}^{f} are the kinetic, potential, surface and dissipation energies after the impact (Mundo et al (1995)).

5.4.2.1 Three-dimensional Breakup Analysis

For a three-dimensional (spherical) drop falling on a solid surface, the kinetic energy of impact per unit length can be written as

$$E_{KE} = \frac{1}{2}\Delta\rho U^{2}\left(\frac{\pi}{6}D^{3}\right) \tag{5.9}$$

where $\Delta\rho = \rho_l - \rho_g$. If the drop spreads to a maximum diameter of D_{max} and a film thickness of h, then by conservation of mass

$$\frac{\pi}{6}D^3 = \frac{\pi}{4}D_{max}^2 h$$

$$\Rightarrow h = \frac{2}{3}\left(\frac{D}{d_{max}}\right)^2 D = \frac{2}{3}\frac{D}{\xi_{max}^2} \tag{5.10}$$

where ξ_{max} is the ratio of the maximum film diameter to the initial diameter of the drop.

The energy lost in dissipating the kinetic energy of the falling drop against viscosity has been shown by Chandra and Avedisian (1991) to follow

$$E_D \approx V\Phi t_e \tag{5.11a}$$

where Φ is the dissipation function given by

$$\Phi = \mu\left(\frac{\partial u_i}{\partial x_j} + \frac{\partial u_j}{\partial x_i}\right)\frac{\partial u_i}{\partial x_j}$$

$$\Rightarrow \Phi \approx \mu\left(\frac{U}{h}\right)^2 \tag{5.11b}$$

and $t_e = \dfrac{D}{U}$ is the time taken by the droplet height to go from D to 0.

Thus, the dissipation energy is given by

$$E_D = \frac{3\pi}{8}\mu U \xi_{max}^4 D^2 \tag{5.11c}$$

The surface energy is dependent on the surface tension. Before the impact, it is given by

$$E_{SE}^i = \pi D^2 \sigma \tag{5.12}$$

96

When the spreading film has stretched to a maximum diameter given by d_{max}, the surface energy can be written as

$$E_{SE}^f = \frac{\pi}{4} d_{max}^2 \sigma (1 - \cos\theta) = \frac{\pi}{4} \xi_{max}^2 D^2 \sigma (1 - \cos\theta) \tag{5.13}$$

The final surface energy is a function of the contact angle. In earlier studies, it has been found that the maximum spread factor has little dependence on the contact angles for Re>10 flows. Analytical work by Pasandideh-Fard et al (1996) has also shown that capillary effects can be ignored for flows with We>>Re$^{1/2}$. Thus, it is assumed that the final surface energy is not dependent on the contact angle, and by substitution of these expressions in equation 5.8, and on simplification, the energy equation can be reduced to

$$\frac{3(\xi_{max}^2 - 12)}{We} + \frac{9\xi_{max}^4}{2\,Re} = \frac{\Delta\rho}{\rho_l} \tag{5.14}$$

For large differences in density, the right hand side of equation 5.14 is 1.0. However, in the current study, $\Delta\rho/\rho_l$ is found to vary from 0.75 to 0.9.

At the instant when the spreading film diameter has reached a maximum, the interplay of the surface and kinetic energies can lead to a possible breakup of this liquid film into smaller daughter droplets. Equation 5.14 can be regarded as a criterion for predicting spreading or breakup outcomes of an impacting droplet. For a situation when

$\dfrac{\rho_l}{\Delta\rho}\left(\dfrac{3(\xi_{max}^2 - 12)}{We} + \dfrac{9\xi_{max}^4}{2\,Re} \right) > 1$, the spreading film will reach a maximum diameter without

breaking up into daughter droplets, whereas when $\dfrac{\rho_l}{\Delta\rho}\left(\dfrac{3\left(\xi_{max}^2-12\right)}{We}+\dfrac{9\xi_{max}^4}{2\,Re}\right)<1,$ the

spreading film will break into smaller drops when the maximum diameter has been reached.

For a water drop impinging a neutral surface and with air as the surrounding medium, i.e.,

$\Delta\rho/\rho_l=1$ in a three-dimensional system, the demarcation line can be defined. From different

experiments, the maximum spread factor at breakup has been found to be between 4 and 5 (Yarin

(2006)). Using these values in equation 5.14, for the maximum spread factor at breakup, the

analytical expression reduces to $12/We+1152/Re=1$ for $\xi_{max}=4$ and $39/We+2812/We=1$

for $\xi_{max}=5$. The map for all such outcomes is given in figure 31. The hatched portion between

the curves may be considered the region where the droplet may or may not break after reaching

the maximum spread factor. For low values of Re and We, i.e., on the left side of the region, the

drop will never break. On the right side of this region, the drop will always break. The two

limiting cases for the drop to break are given by (1) $Re\rightarrow\infty$ and hence We = 12-39, or (2)

$We\rightarrow\infty$ and Re = 1152-2812. Hence, in 3D, for two fluids with a high density ratio, an

impinging water drop will definitely not break into smaller drops only if the condition

$12/We+1152/Re>1$ is satisfied. The We=12 limit is well known from the literature.

5.4.2.2 Two-Dimensional Breakup Analysis and LBM Results

A similar analysis predicts that the corresponding expression in 2D for equation 5.8 reduces to

$$\frac{8}{\pi}\frac{\left(\xi_{max}-1\right)}{We}+\frac{32}{\pi^2}\frac{\xi_{max}^2}{Re}=\frac{\Delta\rho}{\rho_l} \tag{5.15}$$
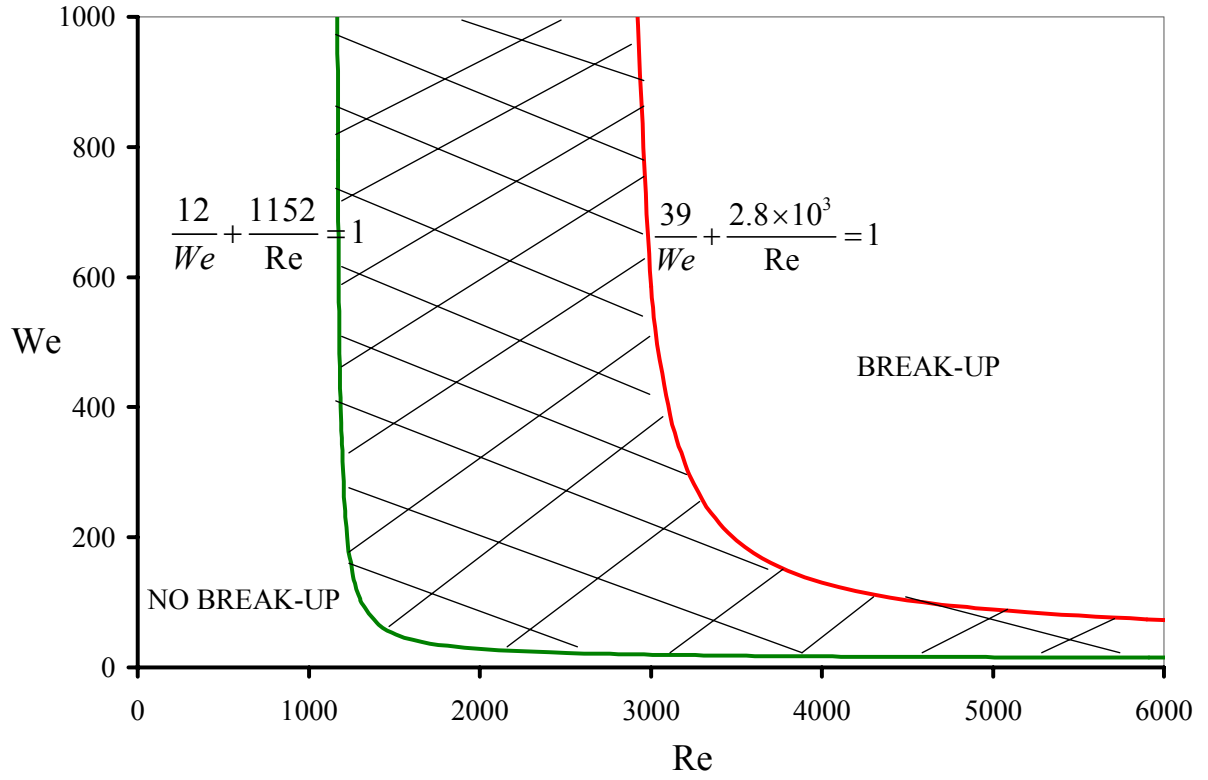
Figure 31: The hyperbolic curve shown with the regimes of droplet impingement with and without breakup for a three-dimensional droplet impingement. The curve on the left indicates the breakup criterion for an assumed value for the maximum spread factor of 4. The right curve represents the maximum spread factor of 5.

Thus, if $\dfrac{\rho_l}{\Delta\rho}\left(\dfrac{8}{\pi}\dfrac{\left(\xi_{\max}-1\right)}{We}+\dfrac{32}{\pi^2}\dfrac{\xi_{\max}^2}{\mathrm{Re}}\right)>1$, the 2D droplet deposits on the solid surface and

reaches a steady shape eventually. Otherwise, if $\dfrac{\rho_l}{\Delta\rho}\left(\dfrac{8}{\pi}\dfrac{\left(\xi_{\max}-1\right)}{We}+\dfrac{32}{\pi^2}\dfrac{\xi_{\max}^2}{\mathrm{Re}}\right)<1$, the

droplet can break. Using LBM results, an extensive analysis of the 2D droplet breakup can now

be performed for a range of We and Re at different density ratios to observe a possible breakup

of the parent drop into daughter droplets due to impact and surface interactions from the wall.

Such an extensive analysis is not possible for a 3D droplet breakup due to the instability that is

propagated for low viscosity solutions using the SC model.

For a fixed density ratio that ranged from 3 to 10, the Weber and Reynolds number were

increased linearly by increasing the diameter of the impacting drop without changing any of the

other variables. The size of the domain in the direction of spread was correspondingly increased

to between 8 and 10 times the diameter of the impinging drop to obtain grid independent

solutions. The current multiphase model precludes any changes in the surface tension parameter

once the interaction strength $G_{\sigma\bar{\sigma}}$ is fixed. As the diameter is increased, the maximum spreading

film diameter increases. At a critical value of Re and We, the drop breaks into daughter droplets

when the maximum spreading diameter of around 4 is reached. This process was repeated for

other density ratios as well, and the results for We_{crit} and Re_{crit} are listed in table 2. It can be

observed that as the density ratio increases, the maximum spread factor at breakup also increases,

reaching an asymptote at a density ratio of 10. Using the density ratio and the Re_{crit} and We_{crit}

values, the maximum spread factor at breakup can be back-calculated from the equation 5.15.

Table 2: LBM simulation results at breakup for different density ratios.

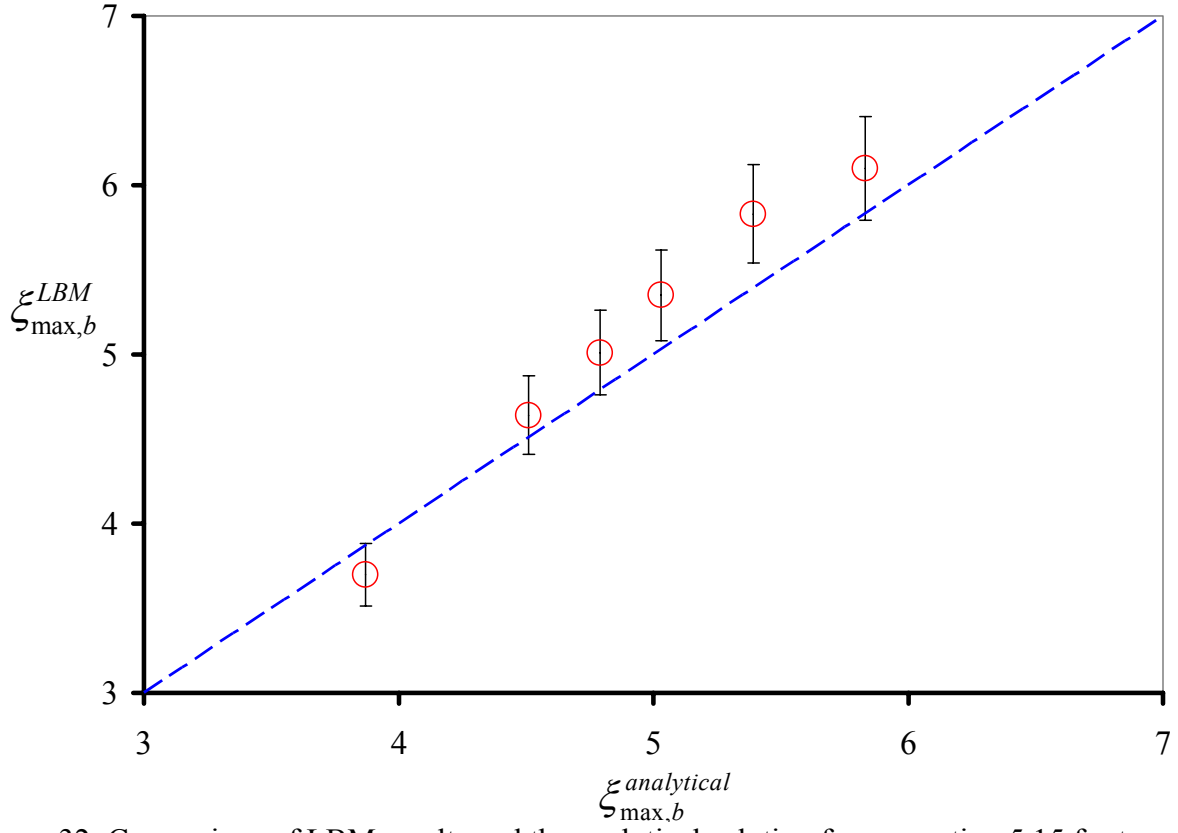| Case	ρ_l/ρ_g	We	Re	ξ_{max}
(a)	3	347.85	75.13	3.7
(b)	4	330	91.1	4.637
(c)	5	252.08	97.56	5.01
(d)	6	222.21	103.87	5.21
(e)	8	186.85	115.57	5.83
(f)	10	183.91	132.1	6.1

Figure 32: Comparison of LBM results and the analytical solution from equation 5.15 for two-dimensional droplets.

The ξ_{max} obtained was compared with the actual ξ_{max} obtained from the LBM simulation, and is plotted in figure 32. For comparison, a line at 45° is drawn that corresponds to an exact match of LBM with theory. The LBM results and the solution from the energy equation were found to be accurate within a $\pm 5\%$ error margin.

The results of increasing We and Re for different density ratios are shown in figure 11. First, Re and We are increased by increasing the drop diameter for each density ratio until breakup occurs. As done before, the Weber number and Reynolds number are recorded at the point of breakup and used in equation 5.15 to find the maximum spread factor. Through this point, the breakup curve for the given density ratio is drawn. For example, at a density ratio of 3 and $\xi_{max} = 3.7$ (see Table 1), a map of the possible outcomes is drawn for $11/We + 73/Re = 1$. Similarly, for $\rho_l/\rho_g{=}10$ and $\xi_{max} = 6.1$, the curve $14/We + 122/Re = 1$ is drawn. Now, all the critical points at which breakup would occur would fall in between these two curves. As the density ratio is increased, the critical point curve shifts to the right, decreasing the value of Weber number and increasing the value of Reynolds number for breakup. Several density ratios were run to generate We$_{crit}$ and Re$_{crit}$, and the locus of these points is drawn as the solid curve in figure 33. Below this critical line, droplet breakup would not occur, and above it, it would for any density ratio. Above We$_{crit}$ and Re$_{crit}$, the drop may break into two to three smaller droplets.

5.4.2.3 Surface Wetting Characteristics of a 2-D Droplet

Wetting characteristics play an important role in determining the mechanism of breakup. To compare how the wetting nature of the wall can affect a possible breakup of the spreading liquid
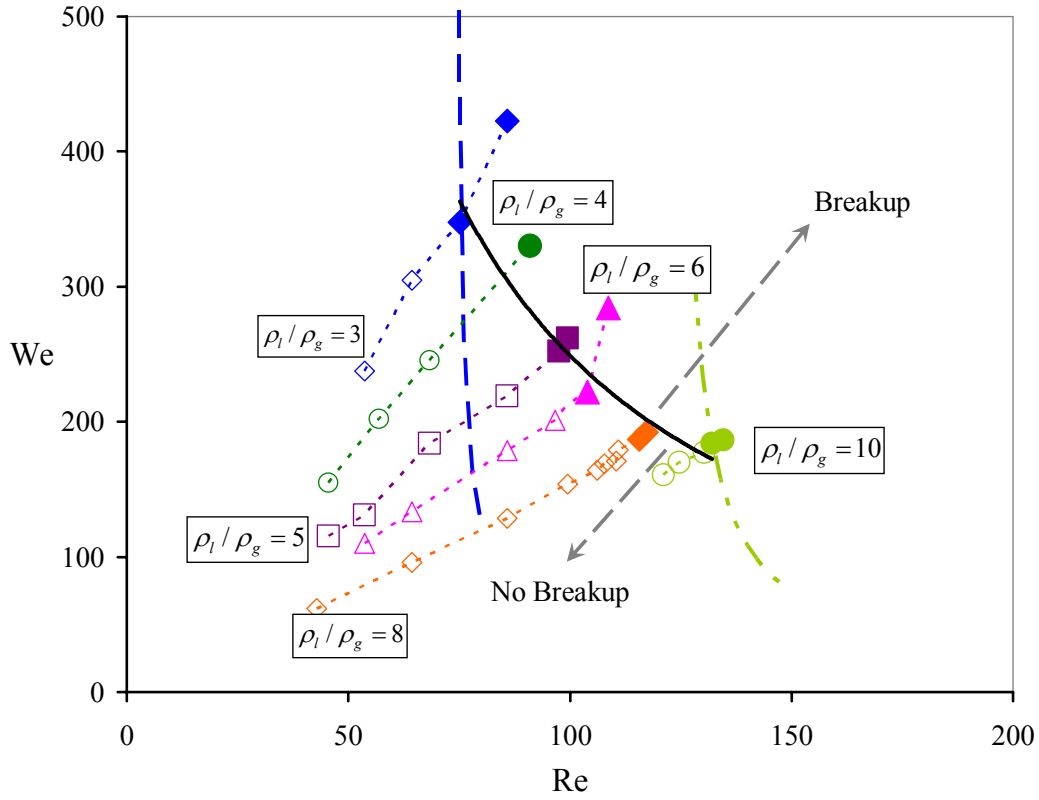
Figure 33: The spread/breakup regime map for impact of single droplet with a solid surface for neutral wetting conditions. The hollow symbols indicate that droplet spreads without breakup, and the filled circles indicate a breakup of the parent droplet. The demarcating curves (broken lines) that are shown are from the solution of the equation $\dfrac{\rho_l}{\Delta \rho}\left(\dfrac{8}{\pi} \dfrac{\left(\xi_{max} - 1 \right)}{We} + \dfrac{32}{\pi^2} \dfrac{\xi_{max}^2}{Re} \right) = 1$ for selected density ratios of 3 (— — —) and 10 (— ·· —). These curves move to the right as the density ratio is increased from 3 to 10. Also shown is the locus (solid line) of the critical parameters at breakup.
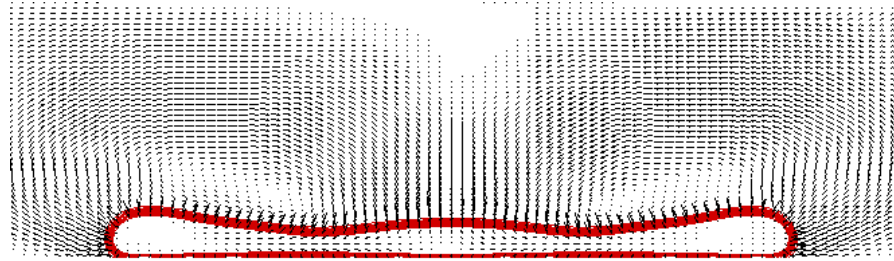
(a) Wetting
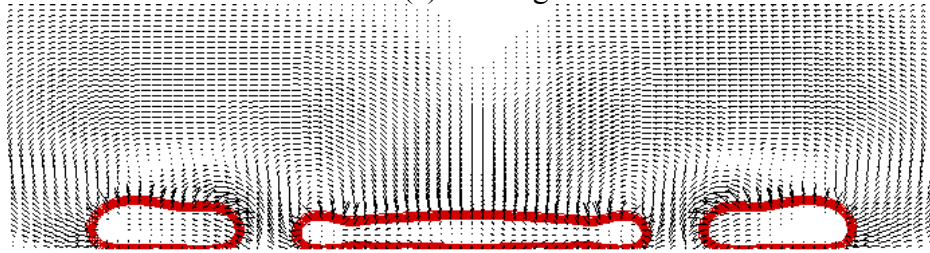
(b) Neutral
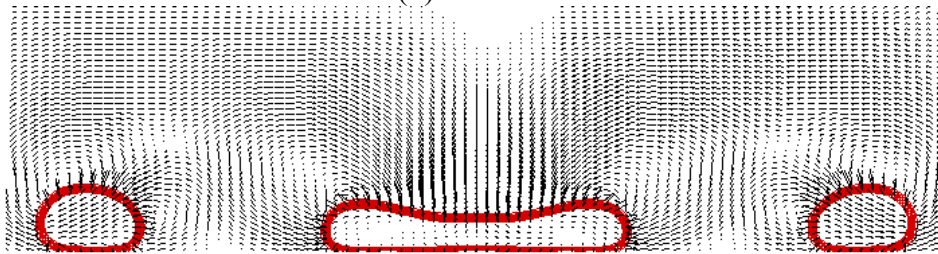
(c) Non-wetting

Figure 34: Different outcomes of a droplet splashing mechanism depending on the surface wetting characteristics at We=114 and Re=152. The domain size has been shown as truncated on the left and right boundaries and extends much further than as depicted.

film on the wall, simulations were conducted at different We and Re values, and the density ratio was also varied, one of which is shown in figure 34. For this case, We=114 and Re=152, and the surface was varied to be wetting, neutral and non-wetting, as is shown in the figure below. For a non-wetting surface (figure 34c), the impinging drop was observed to breakup readily upon impacting the solid surface. Since the surface is non-wetting, the drop fails to have an affinity for the solid wall, and in turn the surface interactions from the solid reduce the surface energy. This leads to a strong elongational flow and a high kinetic energy in the direction of spread, eventually leading to a breakup of the parent drop. In the case of a wetting surface, the surface energy is high, and thus plays a prominent role in reducing the kinetic energy in the transverse direction due to which the film spreads to a maximum diameter and yet does not break into daughter drops (figure 34a). A neutral surface can be described by equation 5.15, and for the We and Re case shown in figure 34b, the outcome lies on the right of this critical curve. It is also seen that the nature of the spreading film breakup is vastly different for the non-wetting and neutral cases. Hence, a possible breakup of the drop on a neutral or non-wetting surface can be averted by altering the surface and making it wetting in nature.

5.5 Summary

The lattice Boltzmann method has been used in the current study to simulate single- and two-phase fluids. Bubble coalescence was found to occur in a three stage process, namely collision, draining of the liquid film and eventually its rupture. The bubble dynamics is dictated by vortex pattern of the leading bubble, which allows the bubbles to coalesce. Such simulations have also been run for different configurations of the initial bubble distribution to show the effect of vortex

106

shedding on the oscillatory motion of the bubbles. Staggered bubbles yield a qualitative overview of the process of bubble coalescence in channels in which lift forces come into play because of the presence of walls.

In addition, LBM has been used to perform three-dimensional simulations of droplet impact dynamics using a model that allows two-phase interactions. The density ratio was varied between 3 to 10. The model was extended to study the spreading behavior of a single drop colliding with a solid dry surface for a range of Weber (5<We<100) and Reynolds (10<Re<100) number. The current LBM model is shown to be capable of capturing the four phases of droplet spreading on a solid surface, namely (a) kinematic phase, (b) spreading phase, (c) relaxation phase, and (d) equilibrium phase. In the kinematic phase, the wettability had no influence on the spreading diameter, which was found to obey the relationship, $d/D = 1.35t^{*0.5}$. In the spreading phase, it was found that the spread factor is higher for high inertia impacts, or high Weber number. The results are found to match well with existing experimental results and with the analytical expression given as $\xi_{max} = 0.5\,\text{Re}^{0.25}$ which is valid for We>12 and $\text{Re}^{1/2}$<<We.

Criteria for two-dimensional and three-dimensional droplet breakup have been developed, which depend on Re and We. Criteria for 3D are provided without results since droplet breakup occurs at higher Re and We, which can not be handled by the current model. However, in two-dimensions, for a wide range of Re and We, the LBM simulations obey the 2D droplet breakup criteria developed. The breakup of a 2D droplet is seen to occur only after a maximum spread factor is reached. This value increases with the density ratio, but reaches an asymptotic value at a

density ratio of 10. The LBM simulation results have been compared with an analytical solution for the spread factor based on the conservation of energy and are found to be within ± 5% error margin.

The spreading behavior of the drops is also found to be a strong function of the wetting characteristics of the wall, although for impacts with high inertia the role of the wall wetting characteristics is not very significant as for low inertia impacts. A droplet breaks up easier in cases where the wall is non-wetting or neutral as compared to a wetting surface. The wetting characteristics of the wall influence the geometric separation in such a drop when it eventually breaks up on the wall. Upon breakup, the distance between daughter droplets is much higher in cases with a non-wetting wall as compared to breakup at a wetting wall, which illustrates the role of the surface interactions in the outcome of the impact. In some cases, the breakup can be delayed/averted by suitably altering the wettability of the solid surface by making it hydrophilic.

CHAPTER SIX: DROPLET FORMATION AT A T-JUNCTION

6.1 Introduction

In recent years, microfluidic devices that generate emulsions of liquid droplets suspended in an outer immiscible liquid have found widespread applications in food processing, drug delivery, microanalysis, tumor destruction, as ultrasound agents and in chemical reactions at the micron level (Christopher and Anna (2007)). Many applications are found that involve multiphase transport through thin capillaries and microchannels. For instance, miniature evaporative and distillation units and bubble generators, flow cytometers and emulsions all use transport of two dissimilar fluids through a microchannel. Over the past few years, numerous experiments have highlighted the advances being made in the field of droplet generation using a variety of microfluidic devices, particularly using co-flowing fluids (Umbanhowar et al (2000), Cramer et al (2004)), passing dissimilar fluids through an orifice (Anna et al (2003), Garstecki et al (2005), Tan et al (2004)) and droplet formation at T-junctions (Thorsen et al (2001), Garstecki et al (2006), Van der Graaf (2006), Tice et al (2004), Guillot and Collin (2005), Husny and Cooper-White (2006), Christopher et al (2008)). Due to the length scales involved, the flow of the dissimilar fluids falls in the laminar regime, which enables a higher degree of human control on the injection process. The large surface-to-volume ratio of microchannel enhances the role of surface tension effects as well. In such situations, an understanding of the physical laws depends entirely on a sound knowledge of multiphase flows and a strong control of the fluid streams at the miniature level. The other aspects that influence such class of problems are the flow rates of

the continuous and dispersed phases, viscosities of the fluids, geometry of the device, and interplay of surface tension and viscous forces.

The important parameters that can influence the droplet formation process can be written in terms of the physical parameters that define the two-fluid flow. The three-dimensional geometry of the T-junction is shown in figure 35, where the top and side views depict the channel dimensions and the flow inlets for the continuous and dispersed phase to enter. It is assumed, for simplicity, that the two liquids have similar densities, which is given by ρ. Accordingly, the problem can be described in terms of the following dimensional and physical parameters: w_c, w_d, h, U_c, U_d, μ_c, μ_d, σ and ρ. Based on these nine parameters, we can define six independent dimensionless parameters, using the Buckingham Pi theorem (Buckingham (1914)). Selecting w_c, μ_c and U_c as the primary dimensions, the volume of the droplets that are formed can be written as a function of the following six dimensionless groups:

$$\overline{V} = f\left(Q, \lambda, \Lambda, \Gamma, Ca, \mathrm{Re}\right) \tag{6.1}$$

where $Q = \dfrac{U_d w_d h}{U_c w_c h} = \dfrac{U_d w_d}{U_c w_c}$, $Ca = \dfrac{\mu_c U_c}{\sigma}$, $\mathrm{Re} = \dfrac{\rho U_c w_c}{\mu_c}$, $\lambda = \dfrac{\mu_d}{\mu_c}$, $\Gamma = \dfrac{h}{w_c}$ and $\Lambda = \dfrac{w_d}{w_c}$.

de Menech et al (2008) argue that for low Reynolds number flows and fixed geometry, the number of parameters reduce to Q, Ca and λ. As the droplet formation process in microchannels is highly laminar in nature, the characteristic velocity of the flow would inherently be small. In such a case, a model that can successfully simulate two dissimilar fluids, and at the same time achieve numerical stability at low velocities is highly desirable.

(a)

(b)
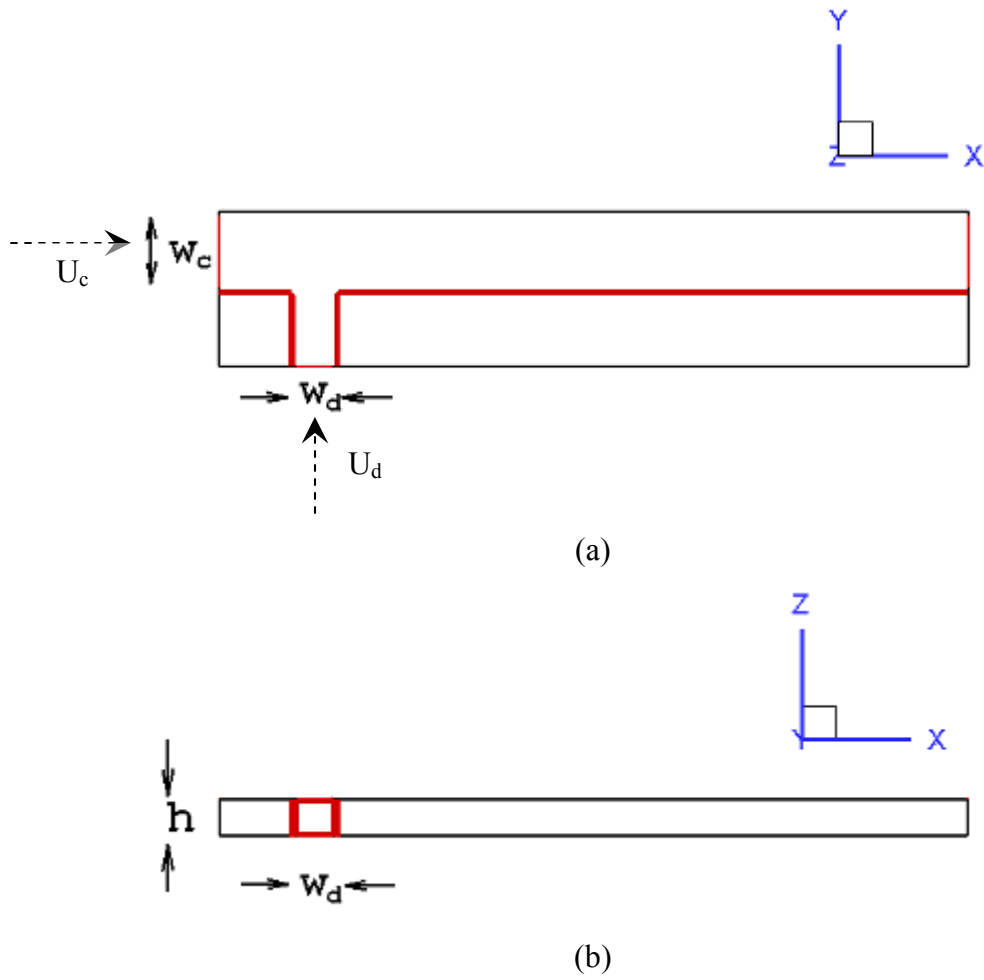
Figure 35: (a) Top and (b) side view of the T-junction microchannel used for modeling formation of droplets. The inlet channels are marked using velocities at the appropriate faces.
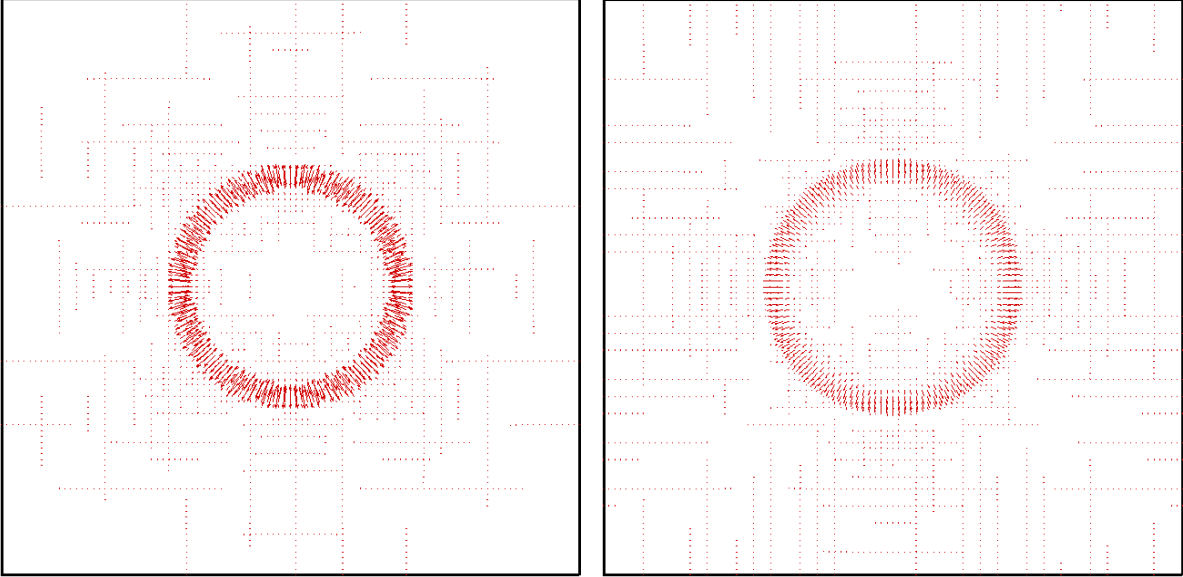
(a) (b)

Figure 36: Comparison of the spurious velocities at the interface of the two fluids with $\sigma = 0.01$ for (a) Shan-Chen's model and (b) Lishchuk et al (2003). The spurious velocities in (b) have been amplified by a factor of 2×10^4 for visual guideline only.

In the last Chapter, the Shan-Chen model was shown to be capable of simulating multiple phases in the scope of LBM. However, it was also found to have some shortcomings: velocity vectors were high at the interface; the model worked well for low density ratios. Figure 36 represents a benchmark case to illustrate this point. Two different simulations for equilibriating a static droplet were run, with the same initial diameter, such that the surrounding medium density is nearly the same as the liquid drop density. For the sake of comparison, the same surface tension parameter was chosen for both Shan-Chen's and Lishchuk's model, which was described in section 3.6.2, and the results at equilibrium are shown in figure 36. It was found that the ratio of the magnitude of spurious velocities for Shan-Chen and Lishchuk's model was of the order of 10,000. More so, the magnitude of spurious currents in terms of the droplet diameter and viscosities selected was found to be $\mathrm{Re}_{Spur} = 3.6$ for Shan-Chen, whereas for Lishchuk's model it was $\mathrm{Re}_{Spur} = 0.001$. Clearly for the problem where the flow Reynolds number is of order $O(1)$, the Shan-Chen model does not offer a viable option, and thus was discarded, and simulation results using the Lishchuk model are presented in the next few sections.

In addition, the color segregation step of the original Gunstensen model was replaced by a recent variant proposed by Latva-Kokko and Rothman (2005), which minimizes the spurious velocities even further, and at the same time removes lattice pinning. According to this method, the post-collision distributions of the two color fluids, red and blue, are computed as

$$f_i^R = \frac{\rho_R}{\rho_R + \rho_B} f_i + w_i \beta \frac{\rho_R \rho_B}{\left(\rho_R + \rho_B\right)} \cos\theta_f \left|\mathbf{e}_i\right| \tag{6.2a}$$

$$f_i^B = \frac{\rho_B}{\rho_R + \rho_B} f_i - w_i \beta \frac{\rho_R \rho_B}{(\rho_R + \rho_B)} \cos\theta_f |\mathbf{e}_i| \tag{6.2b}$$

where

$$\cos\theta_f = \frac{\mathbf{e}_i.\nabla C}{|\mathbf{e}_i||\nabla C|} \tag{6.3}$$

and β is the anti-diffusion parameter and is fixed at 0.7 to keep the spurious currents low and maintain a narrow interface thickness (Lishchuk et al (2008)).

In the following sections, Lishchuk's improved model has been used to conduct simulations of droplet formation for a range of Capillary numbers. It is known from earlier experimental work of Garstecki et al (2006) and Christopher and Anna (2007) that the dominant forces responsible for the formation of droplets vary depending upon the Capillary number of the continuous phase. At very low Ca, the break-up is dominated by a pressure build-up in the liquid upstream of the T-junction, that pushes the interface towards the downstream edge of the dispersed phase inlet channel, pinching-off the protruding dispersed phase and forming droplets that occupy nearly the whole width of the main channel. At slightly higher Ca, a transition regime begins where both pressure and shear stress are responsible for the formation of droplets. At even higher Ca, the formation of droplets is purely shear driven. Each of these regimes, based on the Capillary number of the flow, are described below with results obtained through lattice Boltzmann simulations.

6.2 Low Ca Regime

According to Christopher and Anna (2007), at low Capillary numbers ($Ca \ll 1$), droplet formation is a direct consequence of the pressure force exerted by the continuous fluid on the dispersed phase. At such low Capillary numbers, the drag force becomes negligible as compared to the surface tension forces that hold the interface together. In such a scenario, the viscous forces are not strong enough to overcome the interfacial force, and hence the droplets start to grow in the main channel and block the flow of the continuous liquid (Garstecki et al (2006)). The pressure gradient and the flow of the continuous liquid aid in the distortion of the droplet, and the interface moves towards the exit of the main channel. Due to the blockage of the available area for the continuous fluid to flow downstream, the pressure upstream of the expanding droplet increases, as a consequence of which the upstream interface is pushed towards the downstream edge of the junction. Eventually, the upstream interface is cut-off by the downstream edge of the dispersed phase channel, and a drop in the form of a 'plug' is formed. At this time, the interface retracts and a new droplet starts to penetrate the main channel. A time history of this movement of the interface is depicted in figure 37, where the upstream interface is shown to be pushed down as the pressure of the liquid builds up due to a blockage of the available area for the continuous phase to flow.

Invariably, plugs formed by such a process are found to have a length that is the same order as the width of the continuous phase channel. More so, the length depends on the flow rate of the dispersed phase at a fixed Capillary number of the continuous liquid. Figure 38 shows simulation results obtained in the current study for Ca=0.001 and $\lambda = 1/30$ for a range of flow rate ratios

Q. The number of lattice nodes chosen was $201 \times 41 \times 11$. The flow rate ratio was varied keeping the flow rate of the continuous liquid fixed and increasing the inlet velocity of the dispersed liquid. As can be observed, the length of the plugs formed was highest when $Q = Q_d/Q_c = 2$, and is much larger than the width of the continuous phase channel. As the flow ratio was decreased, plugs of reduced length were formed (figures 38b-f). Below a flow rate ratio given by $Q \leq 1/5$, the length of the plugs was not found to change appreciably, as can be observed from the figure.

Simulations were repeated at Ca=0.0028, with a similar viscosity ratio and the same geometry as used earlier for Ca=0.001, and results are shown in figure 39. For the same geometric and viscosity parameters, the length of the plugs formed at Ca=0.0028 was found to be slightly lower than those formed for Ca=0.001. As the Capillary number was increased based on the velocity of the continuous liquid stream, the decrease in the length indicates the minor role that the viscous forces start to play in the squeezing regime. Decreasing the area ratio Λ for Ca=0.0028 gives similar results, but with a slight change in the lengths of the droplets that were formed, as shown in figure 40. To compare the effect of geometry on the size and shapes of the droplets formed, a three-dimensional comparison of the droplet shapes formed for the two different flow situations described above is shown in figure 41. The figure indicates that the droplets formed are highly confined (i.e. non-spherical), and the lengths strongly depend on the flow rate of the dispersed phase liquid. The formation of plugs (at high Q) was replaced by formation of circular disk-shaped 'cobbles' as the flow rate ratio was decreased. This change in the shapes of the droplets

116
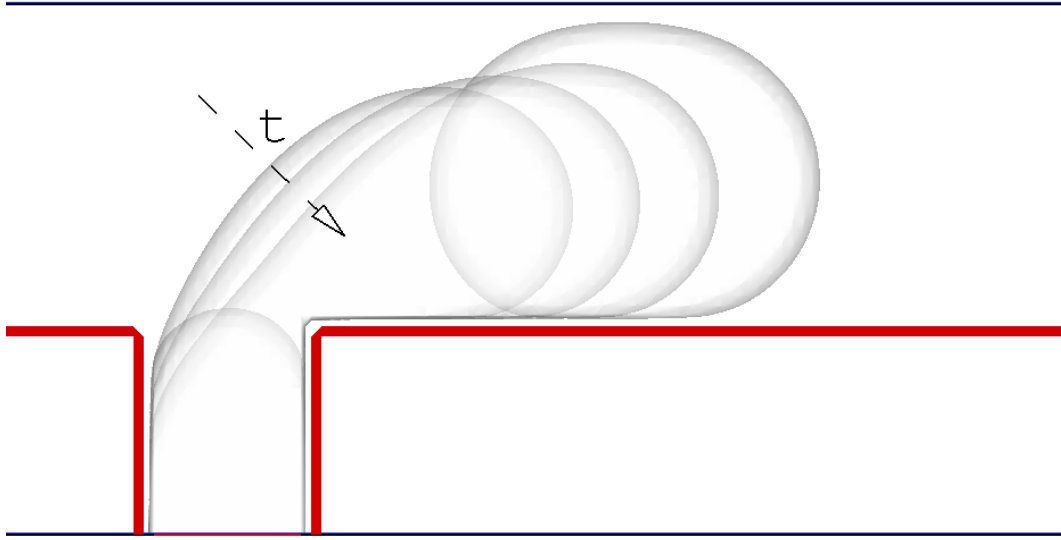
Figure 37: Formation of a plug for Ca=0.0028 and $\Lambda = 1/2$ using lattice Boltzmann simulations. It can be observed that the upstream interface moves towards the downstream edge of the dispersed phase channel with time, where the interface is pinched-off eventually.
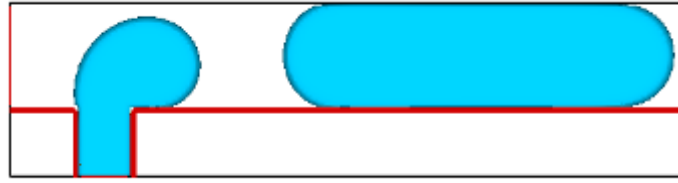
(a) $Q=2$
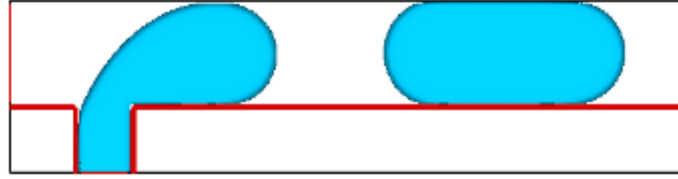
(b) $Q=1$
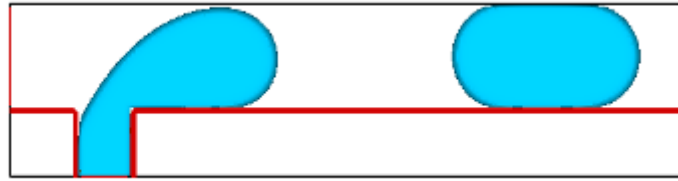
(c) $Q=1/2$
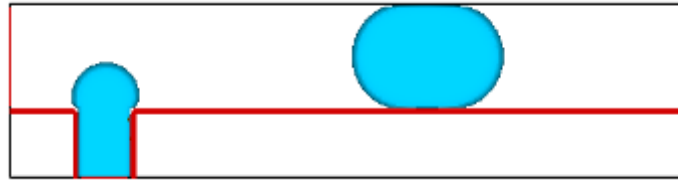
(d) $Q=1/5$

(e) $Q=1/10$
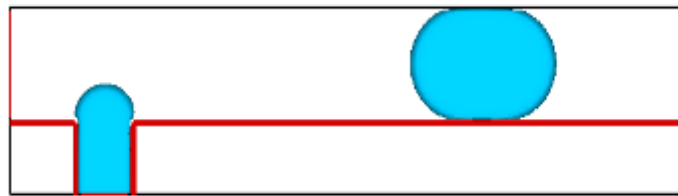
(f) $Q=1/20$

Figure 38: Variation in the droplet length as a function of flow rate ratio for Ca=0.001, $\lambda = 1/30$ and $\Lambda = 1/2$.

(a) $Q=1$
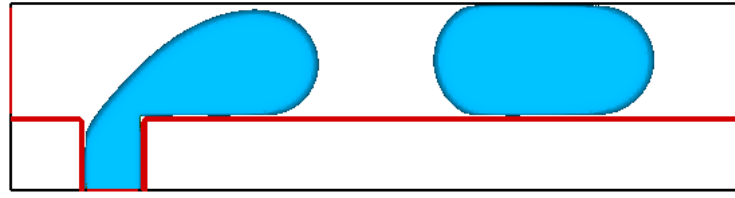
(b) $Q=1/5$

(c) $Q=1/10$

(d) $Q=1/20$

Figure 39: Plug shapes for Ca=0.0028, $\lambda = 1/28$ and $\Lambda = 1/2$.

(a) Q=1
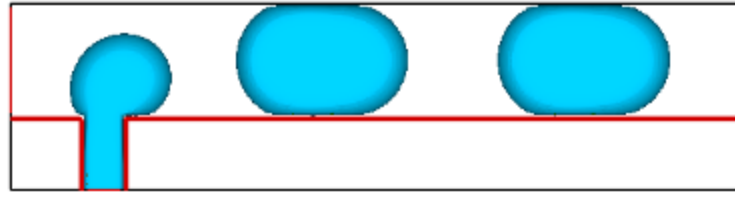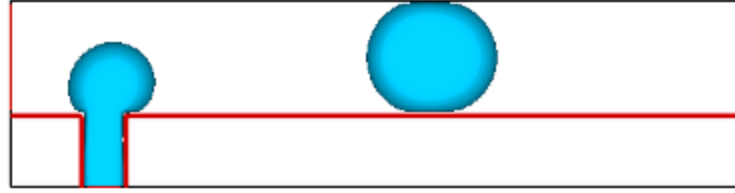
(b) Q=1/5
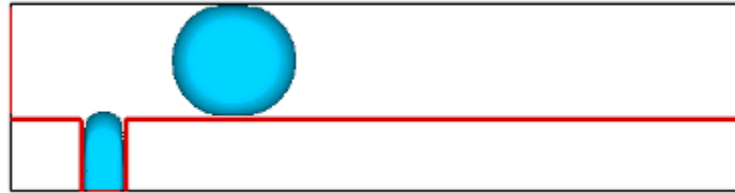
(c) Q=1/10
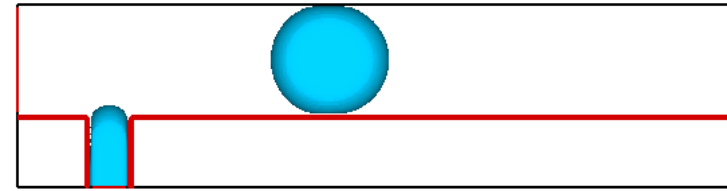
(d) Q=1/20

Figure 40: Plug shapes for Ca=0.0028 and $\Lambda = 1/3$, $\lambda = 1/28$, $\Gamma = 0.6$.

formed, i.e. plugs to cobbles, was again found to occur for Ca=0.006, as shown in figure 42, where the shapes as a function of the flow rate ratio is demonstrated.

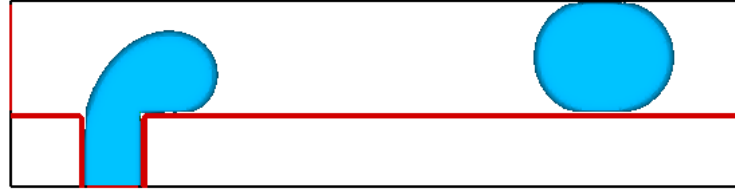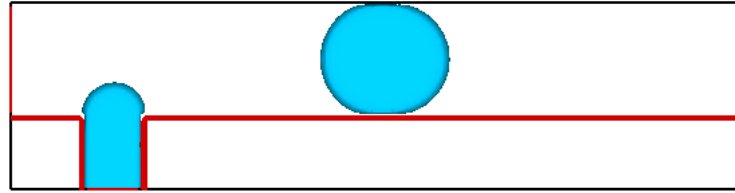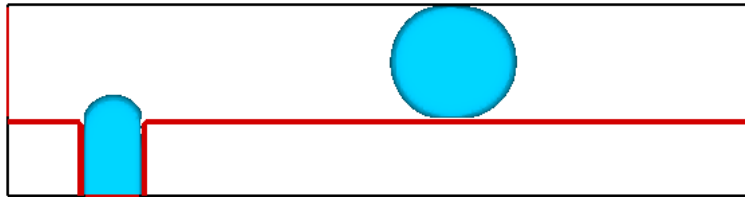For the range of Ca simulated in the squeezing regime, a common picture emerges. The droplet lengths are found to increase drastically for flow rate ratios given by $Q \geq 0.5$. For all flow rate ratios less than 0.2, the droplet lengths change little and seem to reach an asymptotic value, which depends on the Capillary number of the continuous liquid. These are summarized in figure 43 in terms of the dimensionless length of droplets formed in this regime as a function of Q. For the sake of comparison, the droplet lengths as predicted by Christopher et al (2008) for $\bar{b} \simeq 1$ in equation 2.7, and the droplet length as predicted by equation 2.1 by Garstecki et al (2006) are shown by dotted lines. Although the results predict droplet lengths of the same order as those predicted by the data fitted equation of Garstecki and an approximate force analysis of Christopher et al (2008), these analyses do not take into account the Capillary number effect on the size of the droplets formed, and on comparison with numerical simulations, are observed to be too simplistic in nature. More so, the analytical expression of Christopher et al (2008) is found to deviate the most from LBM results, as the maximum droplet length predicted by equation 2.7 is highly under-predicted as compared to the drop lengths measured in the current study. It is worth noting that Christopher et al (2008) have also observed that droplet lengths decrease with an increase in the Capillary number, and that the proposed model under-predicts this length measured in their experiments for a range of flow parameters.
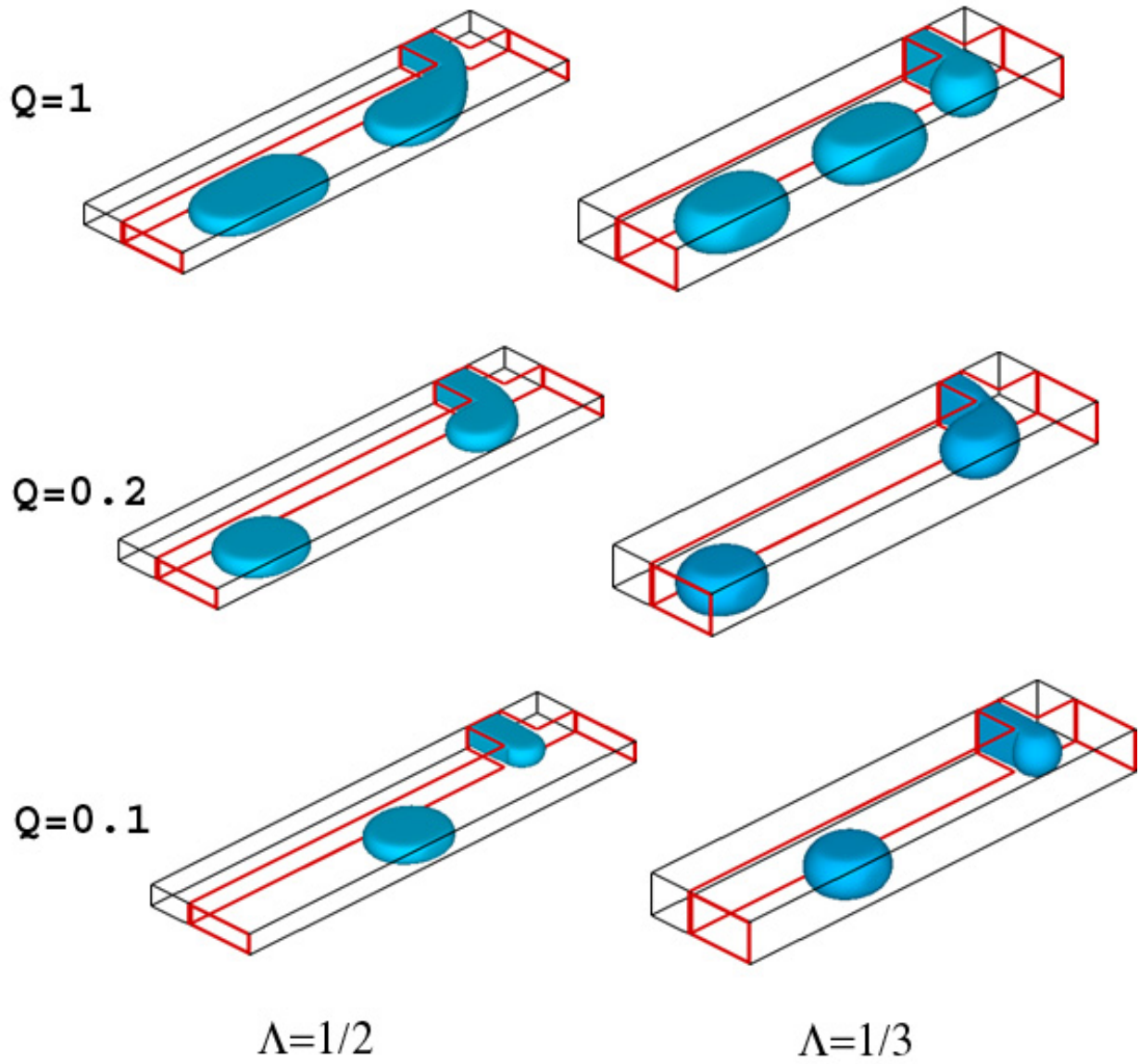
Figure 41: Outcomes for Ca=0.0028 and two different geometries shown as a function of the flow rate ratio.

Q=2   Q=1

Q=0.2   Q=0.1

Q=0.05
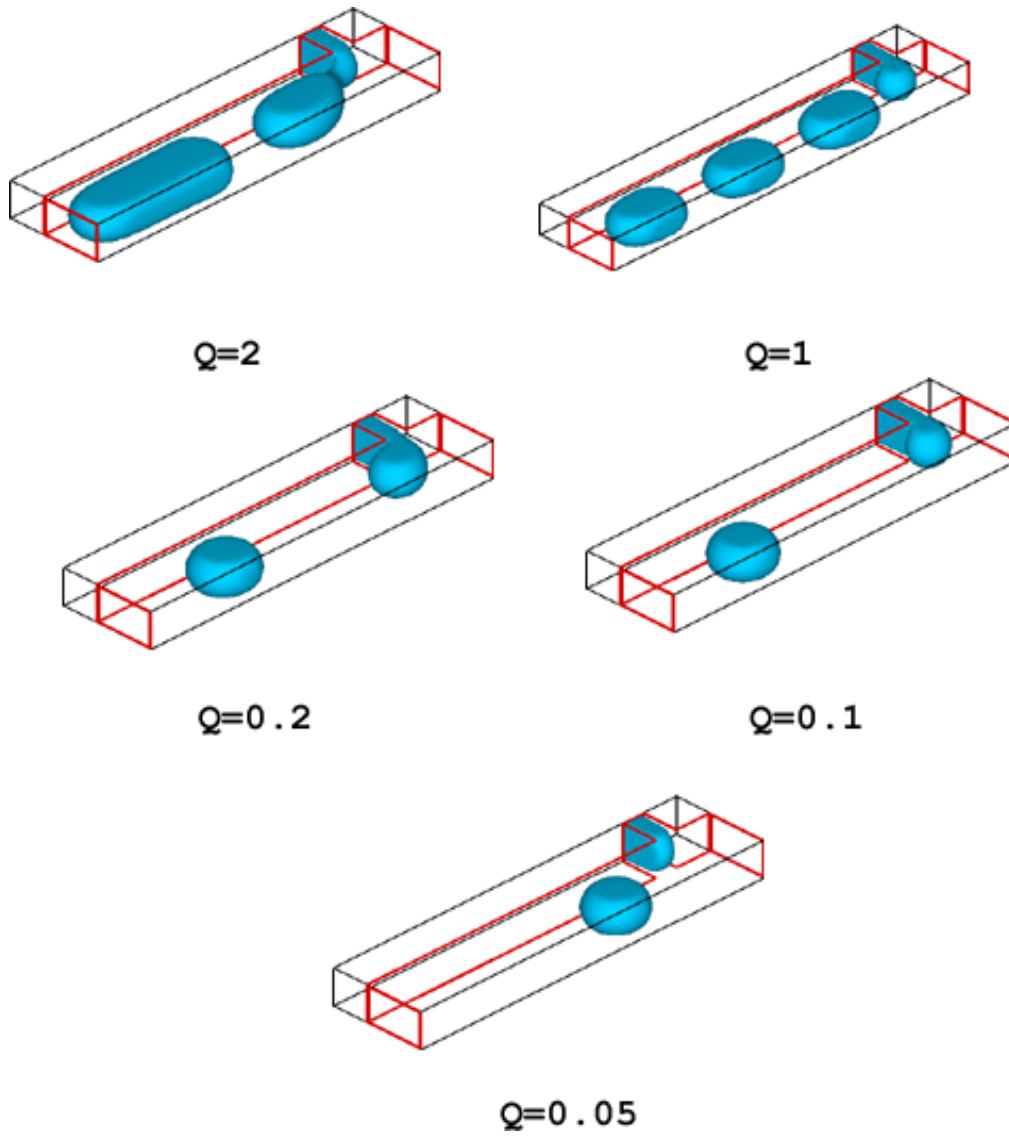
Figure 42: Formation of plugs and cobbles as a function of flow rate ratio for Ca=0.006.
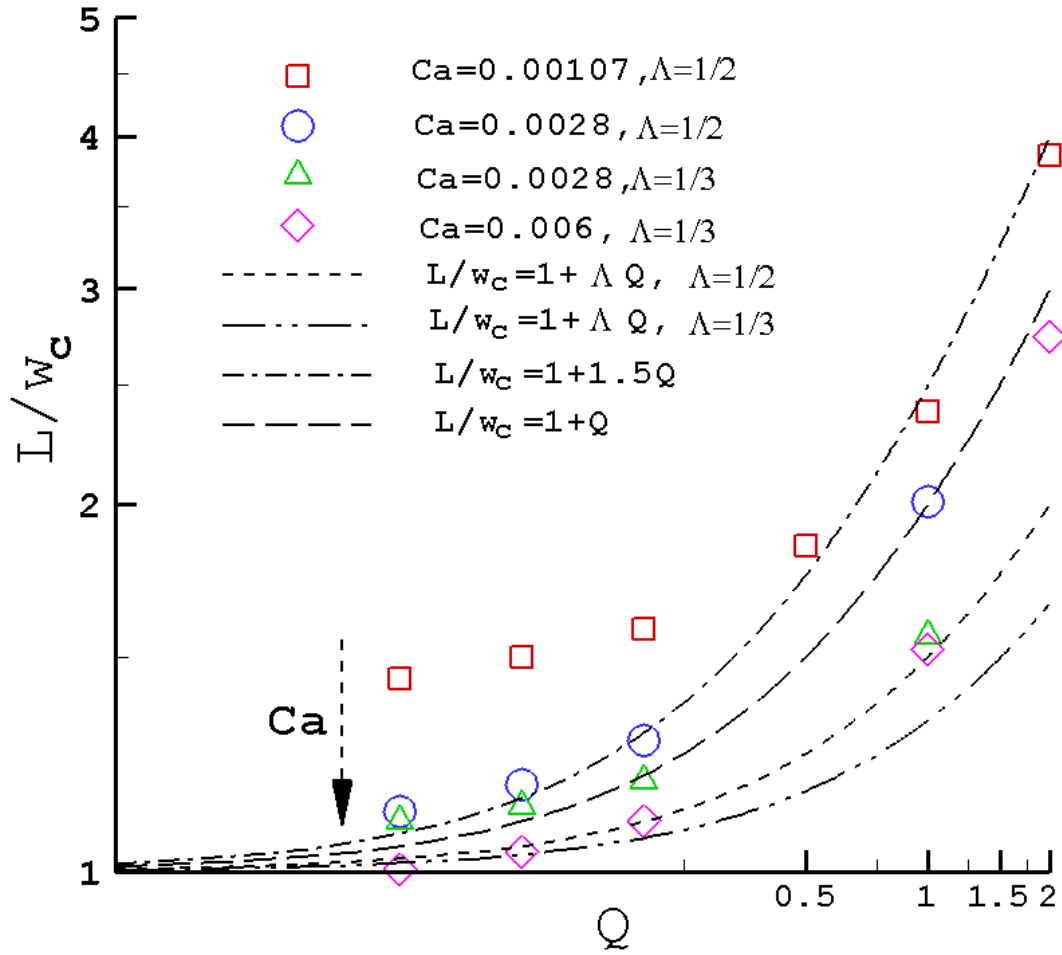
Figure 43: Non-dimensional length of drops formed vs. flow rate ratio for Capillary numbers in the squeezing regime.

6.3 Transition Regime

Between the squeezing and dripping regimes, the droplet formation could be envisaged as a consequence of both pressure and shear forces competing against interfacial tension in deciding the final outcome. De Menech et al (2008) have shown through numerical simulations that the pressure fluctuations decrease remarkably as the Capillary number is increased from 0.004 to 0.045 for a flow rate ratio of $Q = 0.25$ and viscosity ratio of $\lambda = 1$. In the current study, to incorporate the effect of the viscosity ratio in conjunction with the pressure build-up mechanism, pressure profiles upstream of the T-junction were recorded and the fluctuations noted. These are shown in figure 44 for the squeezing regime, and in figure 45 for the Capillary numbers until $Ca = 0.1$. The interfacial tension, viscosities of the fluids and the geometry are fixed such that $\Lambda = 1/2$ and $\Gamma = 1/3$ for $0.01 < Ca < 0.1$, and the Capillary number was increased by changing the average inlet flow velocity. Clearly, holding the flow rate ratio constant requires that the flow rates of the two fluids be increased for the corresponding increase in Ca. The pressure fluctuations for the squeezing regime show that the frequency of oscillations increases considerably as the Capillary number is increased from 0.001 to 0.0028. When the Capillary number is further increased to 0.006, the relative pressure change or consequently the amplitude of oscillations decreases by ~75% and 50% for Ca=0.0028 and 0.006 respectively. The frequency of oscillations is also seen to increase with Ca. The pressure fluctuations for $Ca > 0.01$ are minimal and found to settle down completely, corroborating the theory that pressure forces do not play a role for high Capillary number flows.

According to de Menech et al (2008), the transition regime is also marked with a sharp decrease in the volume of the droplets formed at the T-junction, and is also dependent on the viscosity ratio. To test the hypothesis, simulations were conducted and droplet volumes and frequency measured for the range of Capillary numbers given by $0.01 \leq Ca \leq 0.1$ and $\lambda = 1/10$. For a fixed flow rate ratio, the droplet volume in this regime was found to decrease sharply between Ca=0.01 and Ca=0.04, beyond which the change was more gradual, as is shown in figure 46. The droplet volumes were normalized using $\overline{V} = V/V_0$, where $V_0 = w_c^2 h$ has been used as a characteristic volume based on the width and depth of the continuous liquid channel. From LBM results, it can be observed that although increasing the flow rate ratio increased the droplet volumes, as is evident from the figure, the change was dominant for Ca<0.05. It was also found that the equivalent droplet diameter, calculated based on the diameter for a spherical droplet that would fit the same volume as the volume of the droplets formed at the T-junction, depends on the Capillary number, and was found to obey the following relationship

$$d_{sph}/w_c \propto Ca^{-\alpha} \tag{6.4}$$

where $\alpha = 0.2,\ 0.24$ and 0.25 corresponding to $Q = 1/5,\ 1/10$ and $1/20$ respectively. Clearly, the exponent is α is a function of the flow rate ratio, and does not change appreciably as the flow ratio is decreased. This is similar to the observation of Van der Graaf et al (2006), who observed the exponent to be equal to 0.25, but did not discuss the effect of the flow rate ratio.

In addition to the droplet sizes, the frequency of formation is also calculated, and shown in figure 47. Again, the Capillary number was increased by increasing the flow velocity of the continuous liquid, keeping all other physical properties the same. At a fixed Ca, the flow rate ratio was increased by increasing the flow velocity of the discontinuous liquid. From figure 47, it can be observed that for a constant Ca, the frequency of formation of these drops increases as the flow rate ratio increases. The frequency has been scaled with the capillary break-up time, such that $\overline{f} = f.t_{cap}$, where $t_{cap} = \mu_c w_c / \sigma$, as used earlier by Christopher et al (2008). A higher flow rate ratio would mean that a larger mass of the discontinuous liquid can be pushed into the expanding drop for the same continuous liquid flow rate and viscosity. By conservation of mass, the product of the frequency and the volume of droplets formed should be equal to the mass flow rate of the dispersed phase, i.e., $Q_d = fV$. Thus, a higher flow rate Q_d would translate to higher frequency of the formation of droplets. More so, the dimensionless volume and frequency are related as (Christopher et al (2008))

$$\overline{f} = QCa / \overline{V} \tag{6.5}$$

As a consequence, the frequency and volume are inversely related. Thus simulation results presented in figures 46 and 47 are consistent, as for a fixed flow rate ratio and Capillary number, a decrease in the volume of the droplets should lead to an increase in the frequency of their formation, which was observed to be true, and corroborates with equation 6.5. In addition, from figure 47, it is clear that the frequency of formation increases as the Capillary number increases.
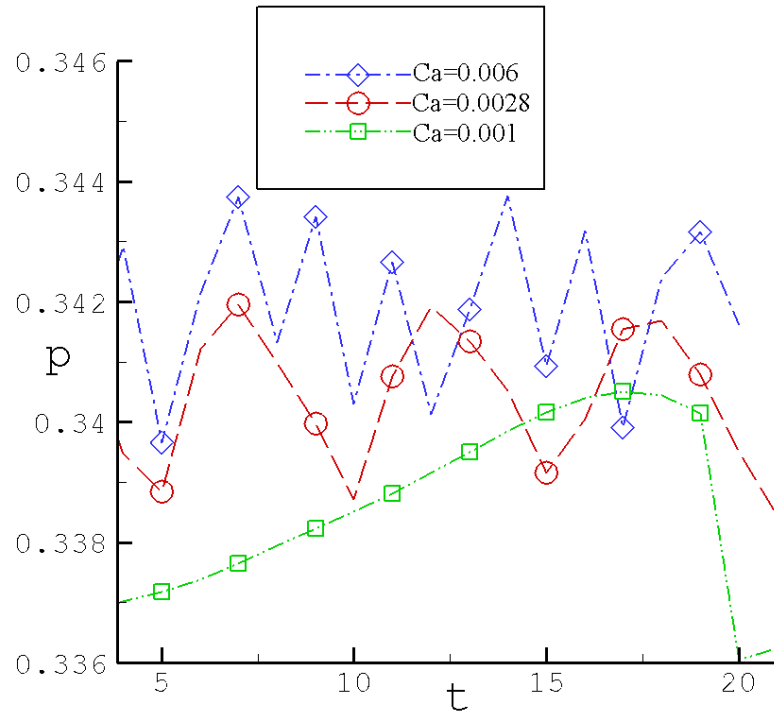
Figure 44: Pressure fluctuation measured upstream of the T-junction for different Capillary numbers.
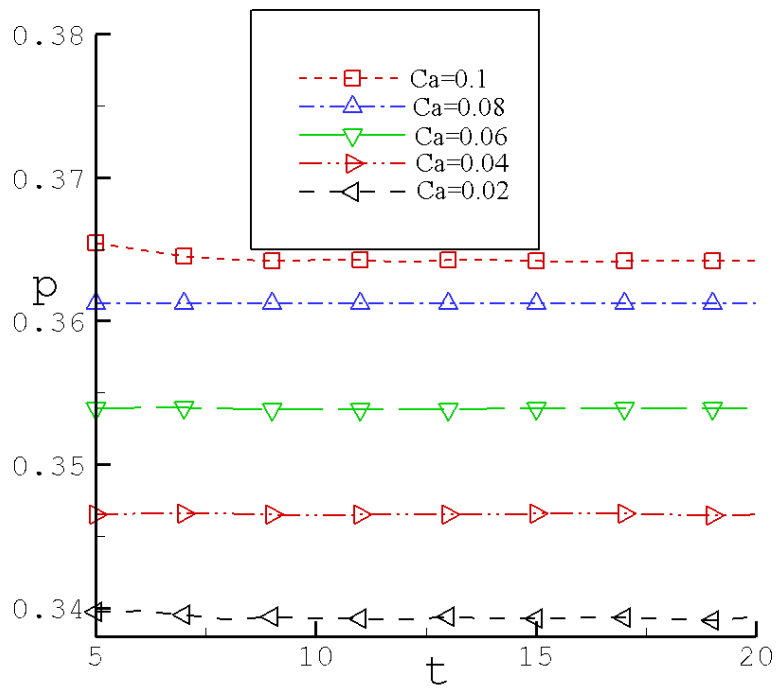
Figure 45: Pressure fluctuation measured upstream of the T-junction for different Capillary numbers in the transition regime.

128
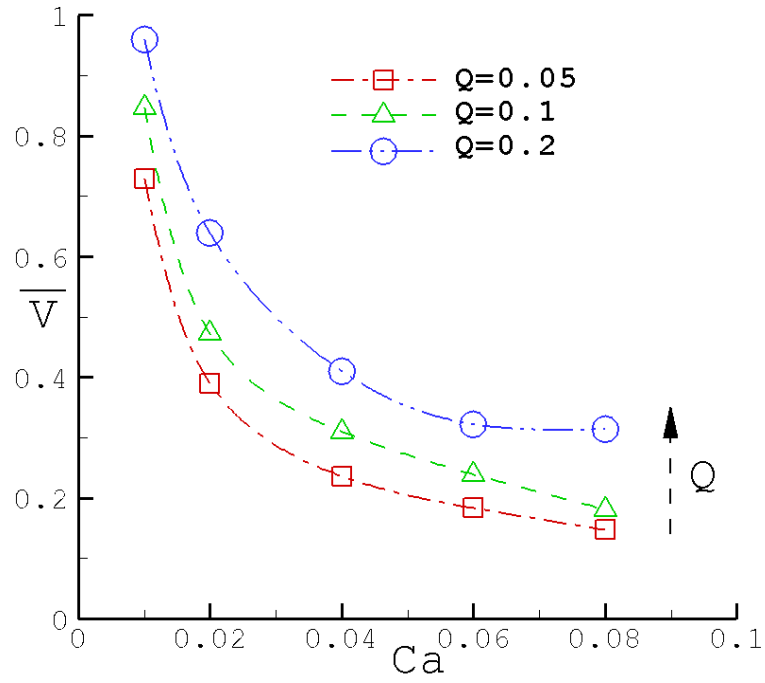
Figure 46: Normalized drop volume as a function of Capillary number for different flow rate ratios in the transition regime for $\lambda = 1/10$.
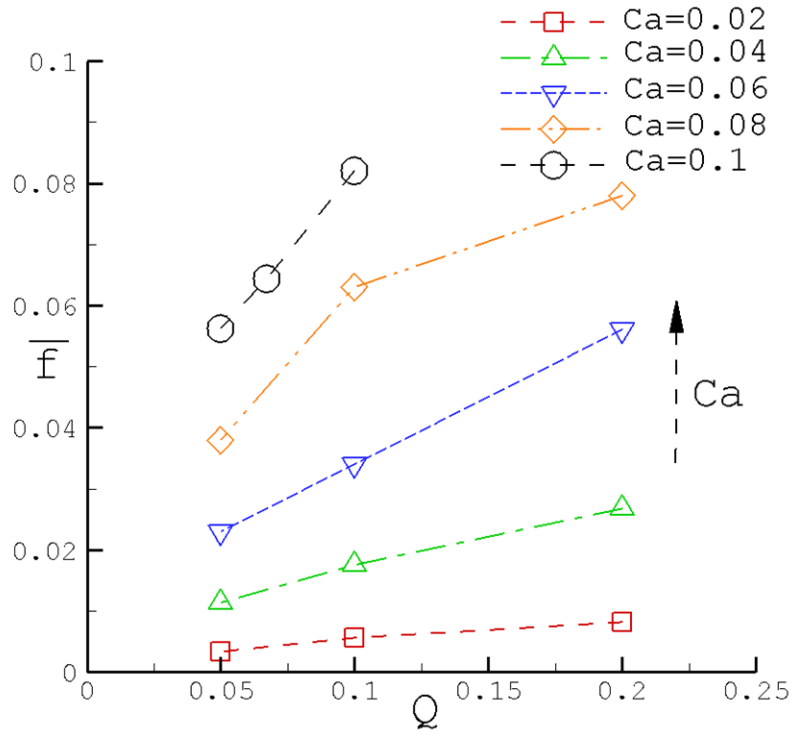
Figure 47: Dimensionless frequency of droplet formation for various Capillary numbers in the transition regime.

129

6.4 High Ca Regime

Succeeding the transition regime is the dripping mode, in which droplets are formed by interplay of viscous and interfacial forces on the expanding discontinuous phase. Earlier studies by de Menech et al (2008) and Van der Graaf et al (2006) have only focused on the simulation of dissimilar liquids with similar viscosities and a simplistic microchannel geometry in which $\Lambda = 1$ and $\Gamma = 1$. Also, it is not clear whether and how the viscosities of the liquids and the channel geometry influence the droplet formation frequency. In this section, the dependence of the droplet formation frequency on the geometry and viscosity of the continuous and discontinuous liquids for flows in which the Capillary number follows $Ca \geq 0.1$ is investigated, followed by an analysis on the stability of formation of droplets for high Capillary numbers.

6.4.1 Effect of Geometry

In the current study, the effect of the width of the continuous phase channel is investigated in context of the formation of droplets in the dripping regime. Figure 48 shows the modes and shapes of droplets formed at Ca=0.1 and $\lambda = 1/10$. The droplets formed are perfectly spherical (figure 48) for a low flow rate ratio given by $Q = 1/20$. As the flow rate ratio is gradually increased by increasing the dispersed phase flow rate (and keeping the continuous flow rate fixed), the frequency of formation of droplets increases, and so does their size. The droplets remain nearly spherical in shape until $Q = 1/5$. At this value, a thread appears that penetrates deep into the main channel, and droplet formation occurs some distance from the T-junction.

Such a situation is commonly known as droplet formed in the channel (DC) and is explained in more depth in section 6.5.

At this point, tests were repeated for the same flow rate ratios but by varying the width of the continuous phase channel. In this study, these widths have been chosen such that $\Lambda = 1/2,\ 1/3, 1/4$ and $1/5$ for simulating the immiscible liquids.

Results for $\Lambda = 1/3$ are shown in figure 49. Similar to the earlier case, spherical droplets are formed at the T-junction for flow rate ratios up to $Q = 1/15$. As the dispersed phase flow rate, Q_d, is further increased such that $Q = 1/10$, the formation of a thread that penetrates into the main channel was evident and droplets similar to the shape of a truncated sphere were formed, as is shown in the figure. At higher Q_d, the dispersed phase forms a stable jet that remains parallel to the continuous outer liquid.

For higher widths w_c, a similar observation can be made. In figure 50, droplet formation for $\Lambda = 1/4$ for Ca=0.1 is shown. For the range of flow ratios studied, the droplets formed are found to be non-spherical and highly confined due to the finite depth of the microfluidic assembly. More so, the thread formed at $Q = 1/10$ is found to penetrate deeper into the main channel, and turns into a jet for higher flow rate ratios. For $\Lambda = 1/5$, shown in figure 51, the thread appears at $Q = 1/15$ and is found to be transformed in to stable jet at $Q = 1/10$.

These observations can be explained as follows. For a fixed Capillary number and the choice of the fluids, the interfacial tension and viscosities remain unchanged, and so does the velocity of the continuous liquid, U_c. For a fixed flow rate ratio, Q, increasing the width w_c results in an increase in the flow rate, Q_c. To account for $Q = \text{constant}$, the flow rate of the dispersed phase has to increase, and since the dispersed phase width is not increased, the flow velocity of the dispersed phase increases. This would result in more volume of the dispersed liquid to be pushed into the expanding droplet. Intuitively, for the same velocity and higher width of the continuous phase channel, the continuous liquid velocity profile would be less steep and the gradient of velocity near the dispersed phase channel inlet would be smaller. This can result in a longer time for the droplet to expand and fill the continuous phase channel, and for higher flow rates of the discontinuous phase may even result in insufficient shear to break the liquid stream into droplets. Borrowing from the definition of Christopher et al (2008), the shear force on the expanding drop is written as

$$F_{shear} \propto \frac{1}{w_c(1-\bar{\bar{b}})} \qquad (6.6)$$

As the shear force is inversely proportional to the width of the continuous liquid channel, an increase in the latter would lead to a decrease in the former. This results in a decrease in the dimensionless frequency of formation of droplets as Λ increases, as shown in figure 52, where the dimensionless frequency obtained using LBM simulations is plotted as a function of the flow rate ratio Q. As Q increases, the frequency increases. The frequency also increases with an increase in the width of the continuous phase channel, w_c.

132

Q=1/5   Q=1/10

Q=1/15   Q=1/20
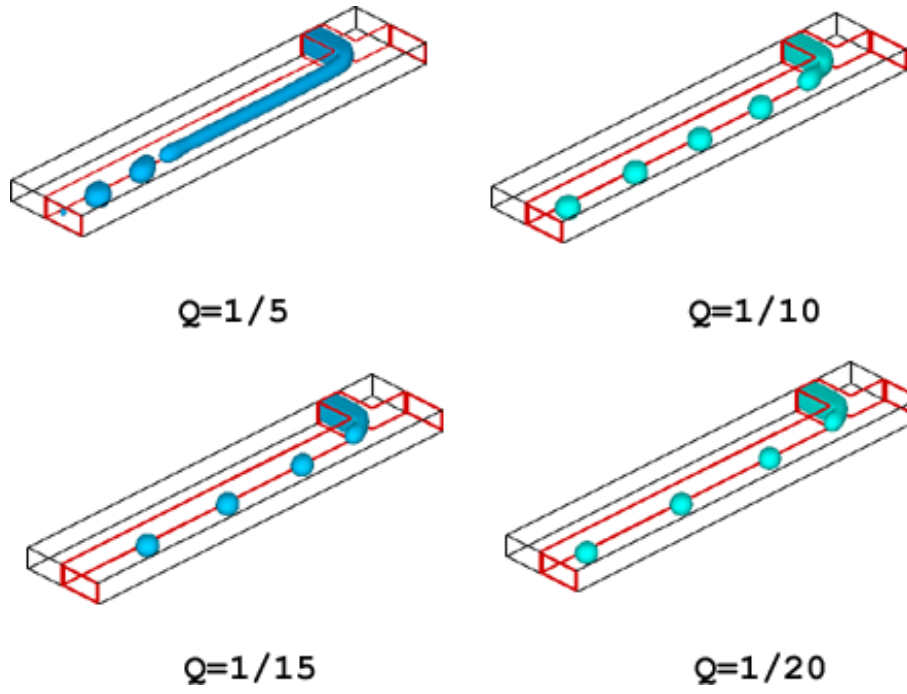
Figure 48: Flow regimes for $\Lambda = 1/2$ and Ca=0.1 at different flow rate ratios.

Q=1/5   Q=1/10

Q=1/15   Q=1/20
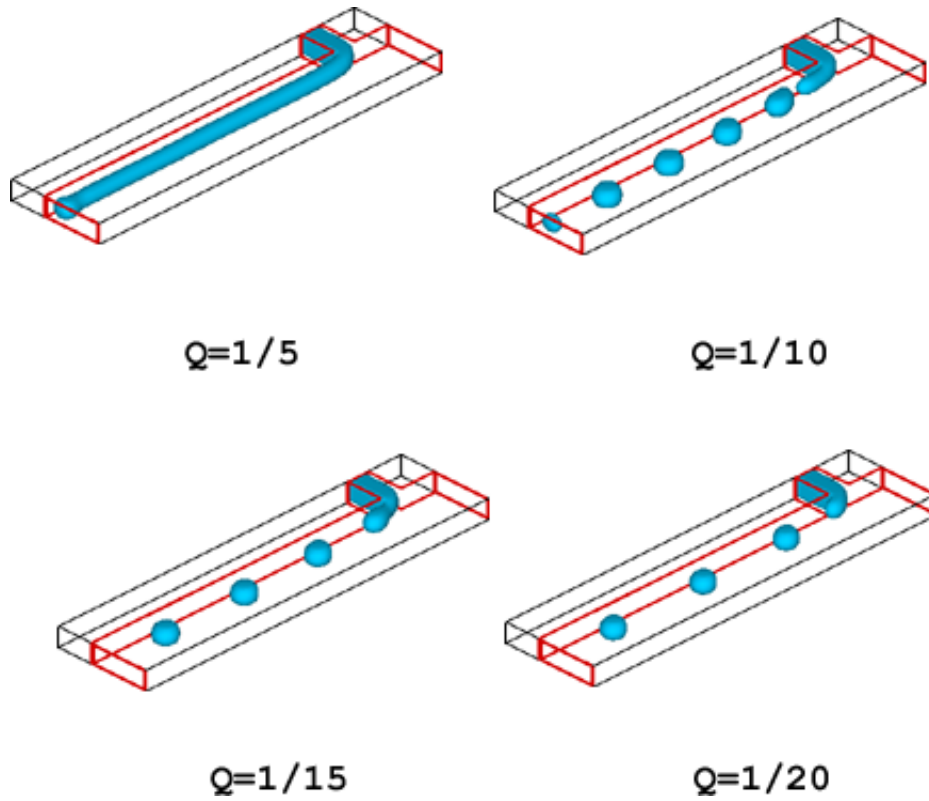
Figure 49: Flow regimes for $\Lambda = 1/3$ and Ca=0.1 at different flow rate ratios.

Q=1/5   Q=1/10

Q=1/15   Q=1/20
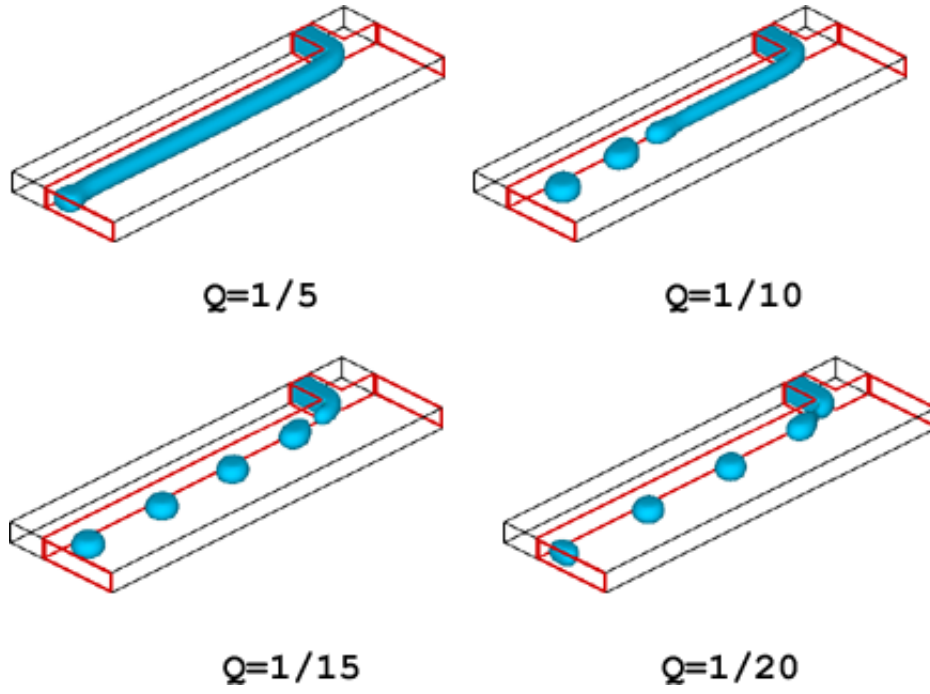
Figure 50: Flow regimes for $\Lambda = 1/4$ and Ca=0.1 at different flow rate ratios.

Q=1/5   Q=1/10

Q=1/15   Q=1/20
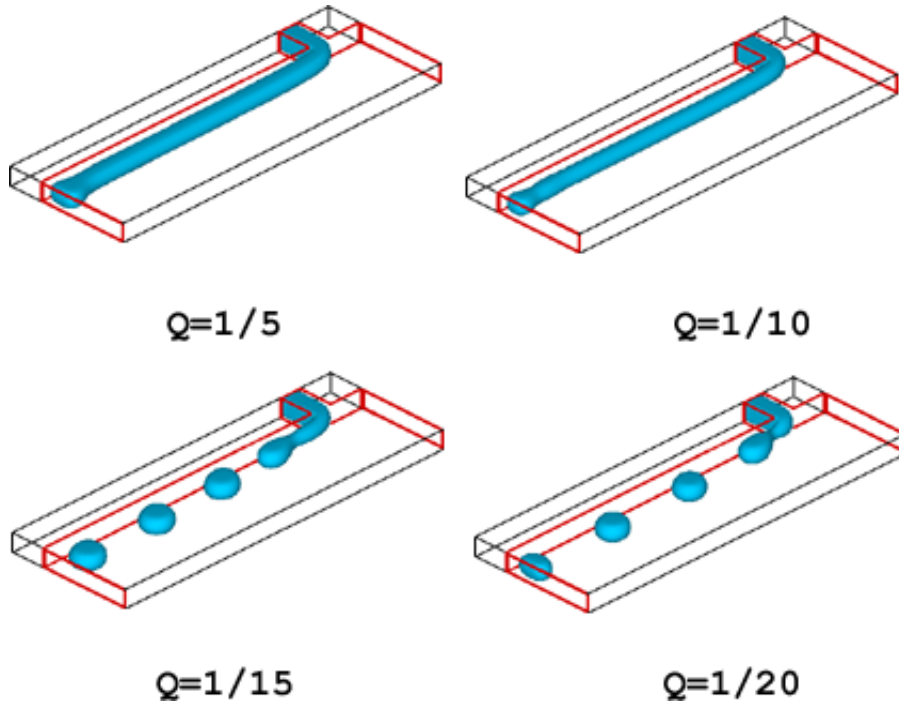
Figure 51: Flow regimes for $\Lambda = 1/5$ and Ca=0.1 at different flow rate ratios.
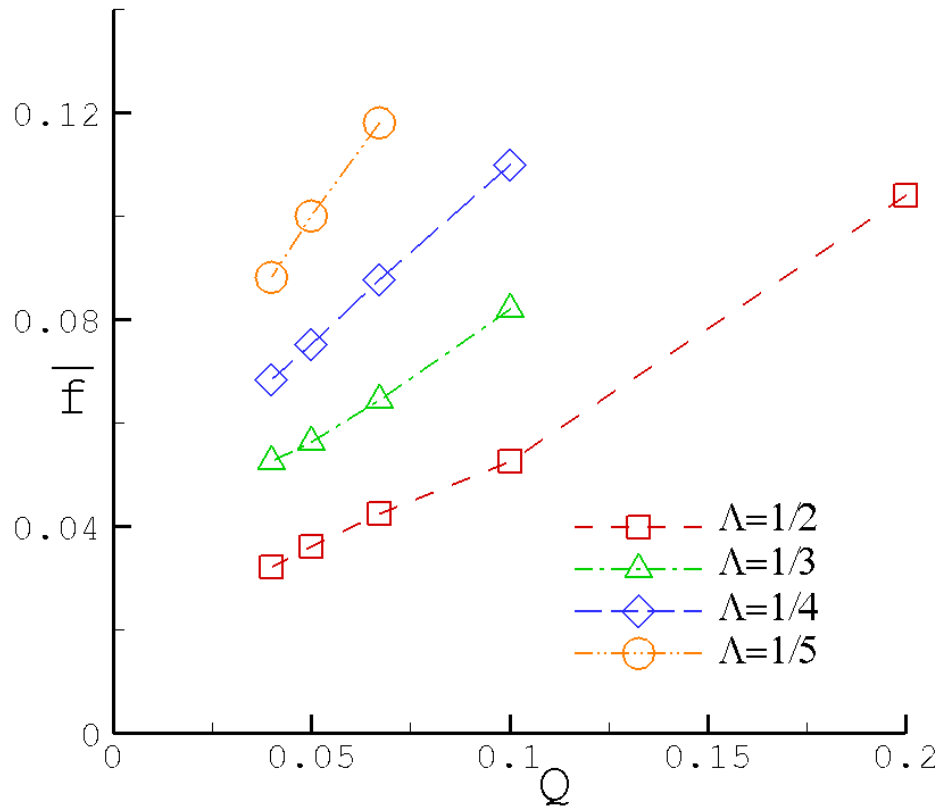
Figure 52: Dimensionless frequency as a function of flow rate ratio for different Λ for Ca=0.1 and $\lambda = 1/10$.

6.4.2 Effect of Viscosity

According to a recent review by Christopher and Anna (2007), the critical Capillary number where the transition from droplet to parallel flow can occur is a function of the viscosity ratio. A high viscosity ratio (i.e. $\text{small } \mu_c$) would indicate a relatively smaller shear force on the penetrating discontinuous phase, and hence a higher likelihood of the thread remaining stable and forming a long jet. In the current work, the effect of viscosity has been studied in the context of flow regimes that emanate for different viscosities of the continuous phase. For the sake of comparison, the Capillary number is fixed at $Ca = 0.1$, and the other parameters are fixed at $\Lambda = 1/2$ and $\Gamma = 1/2$. Comparisons have been made for the viscosity ratios given by $\lambda = 1/10,\ 1/30,\ 1/50 \text{ and } 1/100$. Since the Capillary number and the interfacial tension are held constant, an increase in the continuous liquid viscosity (and a corresponding decrease in the flow velocity) is the method adopted in this work. Results for the range of viscosity ratios in terms of regimes observed are shown in figures 48, 53, 54 and 55 for viscosity ratios of 1/10, 1/30, 1/50 and 1/100 respectively. Based on these, a common theme emerges. The size of the droplets can be observed to increase as the flow ratio increases at a constant viscosity ratio. For a fixed flow rate ratio Q, the droplets can be found to become more confined and resemble truncated spheres as the continuous phase viscosity was increased. More so, formation of droplets becomes easier as the viscosity is increased, as the dispersed phase flow goes from parallel to droplets-in-channel to droplets-at-the-T-junction with an increase in μ_c. This indicates that the droplet sizes and frequency could be controlled by suitable addition of surfactants that may alter the viscosity of the continuous liquid.

The dependence of frequency on the flow rate ratio for the range of viscosities is shown in figure 56. As can be observed, the frequency increases as the flow rate ratio increases. Furthermore, the frequency increased with an increase in the viscosity ratio (or decreasing μ_c). This is against common perception, as an increase in the viscosity of the outer fluid would surmount to a higher shear force, and hence faster breakup of drops and higher frequency. The behavior observed in current simulations can be explained in conjunction with figure 57, where the frequency is plotted as a function of the flow rate ratio for various values of the continuous phase Reynolds number. Going by the argument presented in the earlier paragraph, an increase in μ_c would decrease U_c for the Capillary number to be a constant. This results in a lower volumetric flow rate for the continuous liquid (and hence $\mathrm{Re}_c \downarrow$). At the same time, to keep the flow rate ratio $Q = Q_d / Q_c$ fixed, the dispersed phase flow rate would also need to be decreased by the same factor. This results in a lower overall shear drag on the penetrating discontinuous liquid, and hence a longer residence time in the main channel. A longer residence time results in lower frequency, as well as a higher volumetric flow of the dispersed phase into the main channel, and therefore, droplet with a higher volume is formed. Clearly, for a fixed flow rate ratio, if Q_c increases, then the shear on the penetrating droplet would also be higher, and hence the frequency of formation would increase, as shown in figures 56 and 57 where the dimensionless frequency is found to increase as the continuous liquid flow rate increases.

Q=1/5   Q=1/10

Q=1/15   Q=1/20
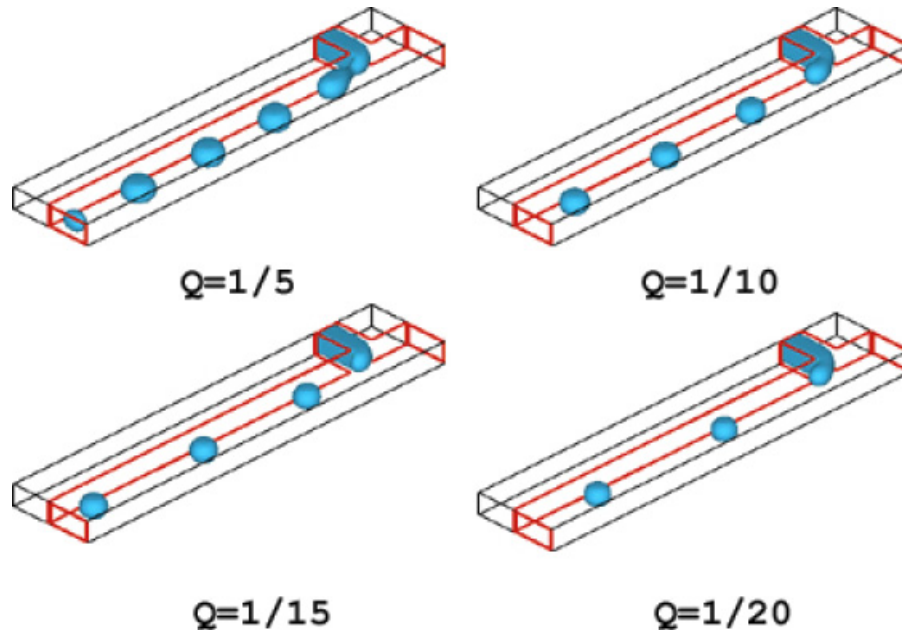
Figure 53: Droplet formation for Ca=0.1 and $\lambda = 1/30$.

Q=1/5   Q=1/10

Q=1/15   Q=1/20
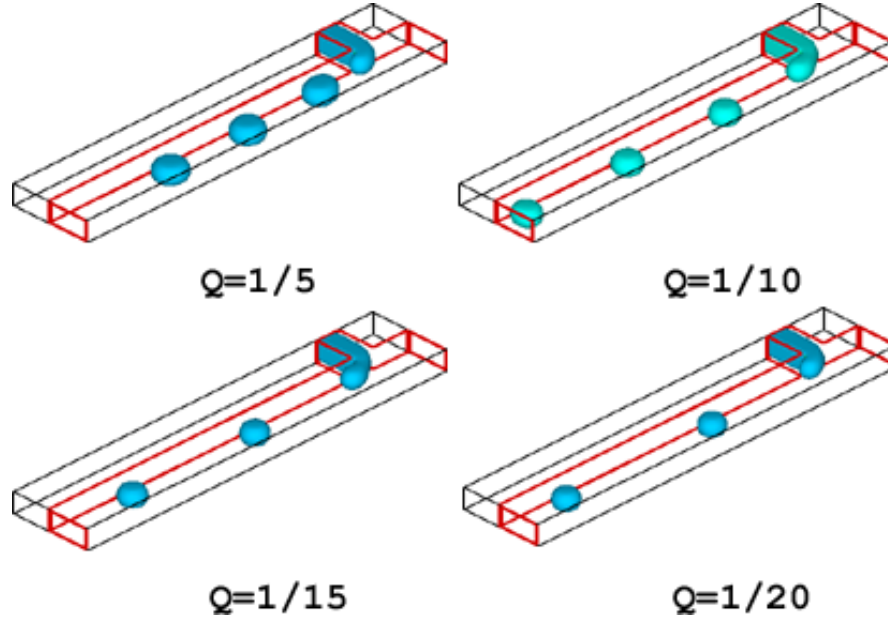
Figure 54: Droplet formation for Ca=0.1 and $\lambda = 1/50$.

Q=1/5

Q=1/10

Q=1/15

Q=1/20
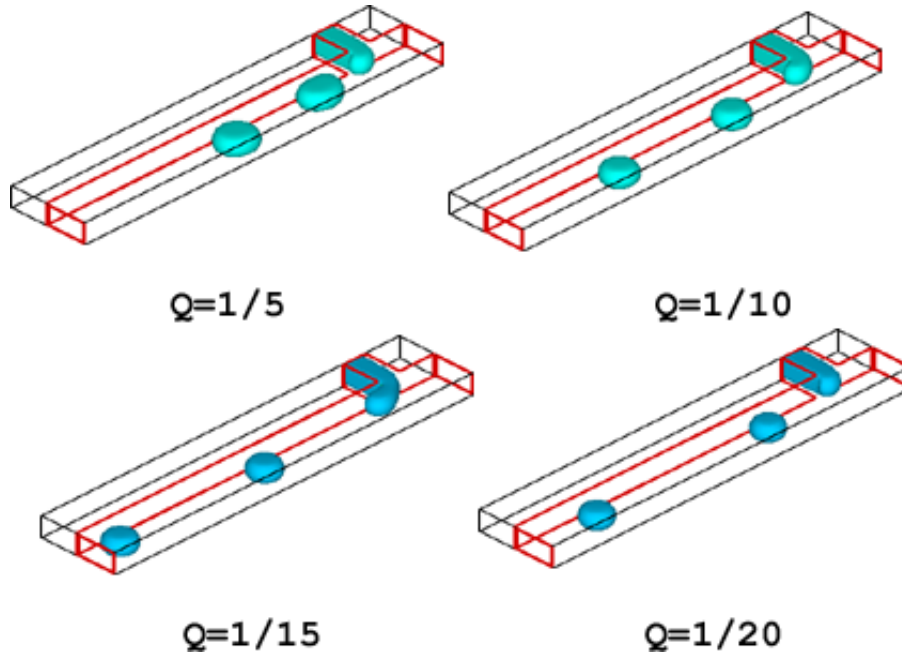
Figure 55: Droplet formation for Ca=0.1 and $\lambda = 1/100$.
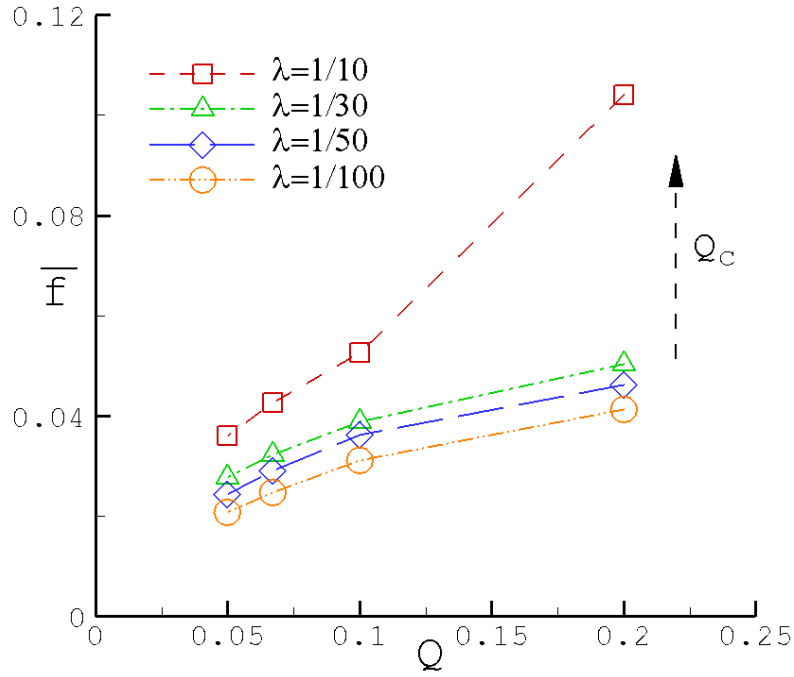
Figure 56: Dimensionless frequency as a function of flow rate ratio for different viscosity ratios at Ca=0.1.
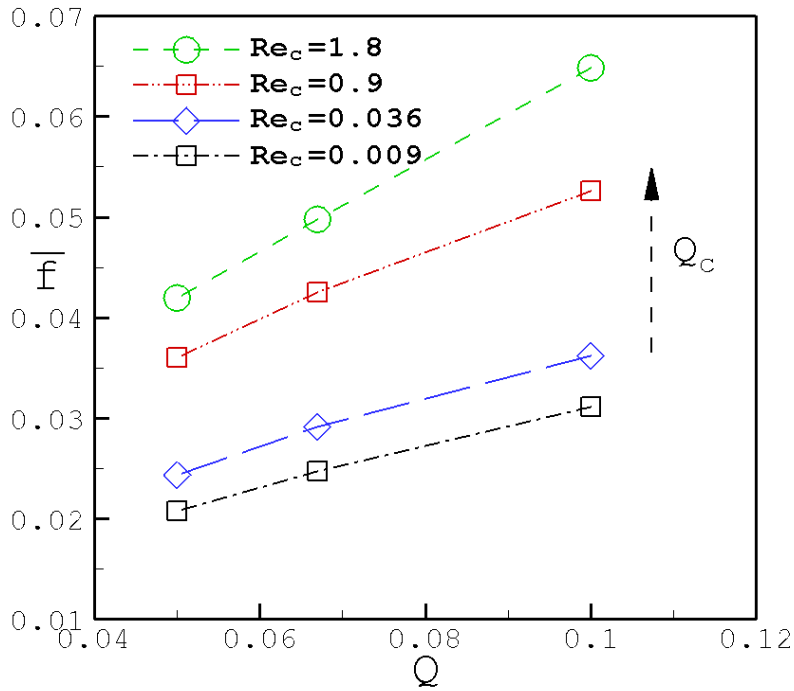
Figure 57: Dimensionless frequency as a function of flow rate ratio for different flow rates of the continuous fluid at Ca=0.1.

For the range of Capillary numbers simulated in the 'dripping regime' in the current work, frequency measurements were made and are shown in figure 58. The abscissa is taken as a product of the flow rate ratio and Capillary number, as it represents an inverse relationship between volume and frequency (see equation 6.5). It was observed, and can be proved intuitively, that with an increase in Capillary number the frequency of the droplets formed increased. An increase in the Capillary number represents a higher viscous force in comparison to interfacial tension forces that hold the dispersed phase thread together. A higher viscous force (or a lower interfacial force) would indicate that the shear force can overcome the interfacial forces for much smaller drop lengths penetrating into the main channel. Also, the inertia associated with the continuous flow can be higher (one method to increase Ca), and therefore, a higher drag induced on the discontinuous liquid, and the shear associated with the form drag would be higher.

In addition, it was observed that the slope of the dimensionless frequency ($\bar{f}$) versus the product of flow rate ratio and Capillary number (QCa) decreases as the Capillary number is increased. This is shown in figure 58. Another point to elucidate from such a behavior is that the frequency of formation of droplets does not increase in the manner as it does for lower Capillary numbers. In fact, droplet formation at higher Capillary number seems to show less dependence on the flow rate ratio. As frequency does not change much with a change in QCa, the volume would be expected to decrease only slightly at such high Capillary number flows. This point has been further discussed in the next section.

141
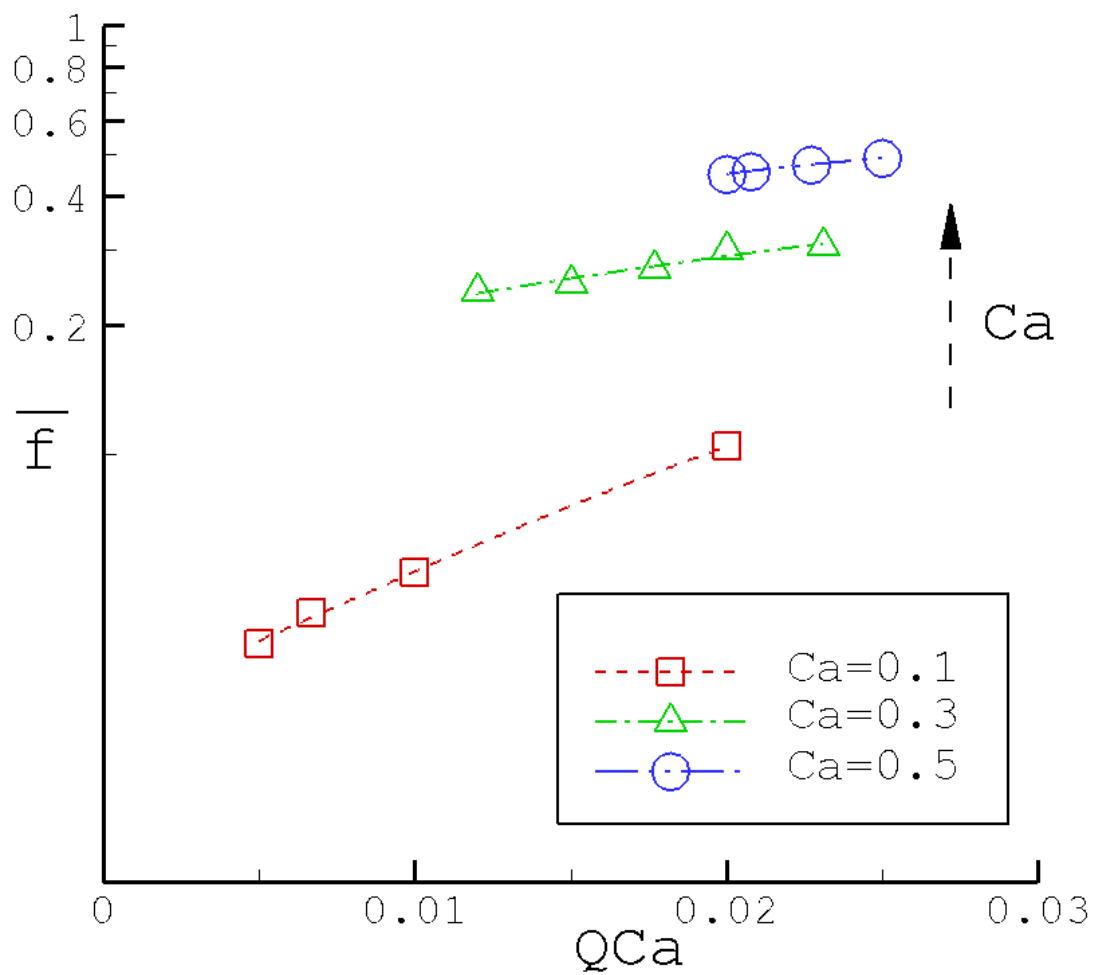
Figure 58: Frequency of the droplets as a function of *QCa* for various Capillary numbers in the dripping to jetting regime.

6.5 Stability of Droplet Formation in Dripping Regime

Existing experiments of Guillot and Colin (2005) show that when for a given continuous phase flow rate, if the dispersed flow is increased, the flow pattern changes from DTJ (Droplets at T-junction) to DC (Droplets in Channel). This indicates that for a given Capillary number ($Ca = \mu_c U_c / \sigma$), when the flow rate ratio $Q(= Q_d / Q_c)$ in increased, such a regime change happens. With further increase of Q, the flow regime changes to PF (parallel flow). These regimes appear to be established mostly for low Capillary number. The experimental findings of Guillot and Colin (2005) further reveal that the stability of parallel flows in a funneled T-junction is linked to the flow rates, wetting behavior, viscosity contrast and aspect ratio of the inlet channel for the two liquids. The geometry of the microchannel chosen by them was different from the conventional T-junction microchannels commonly encountered, and the droplet formation was a consequence of the competing nature of two fluid streams colliding head-on, and subsequently guided through a funnel into the main channel. Although theoretical work on exploring the interplay of surface tension and viscous forces for such devices has gained attention (Van der Graaf et al (2006), de Menech et al (2008)), these have primarily focused on viscosity ratios $\lambda = \mu_d / \mu_c > 1/8$, and aspect ratios $w_c / h = 1$ and $\Lambda = w_d / w_c = 1$. A theoretical treatment of the problem of stability of flows has not been carried out for $Ca > 0.1$, where squeezing pressure is not the dominant mechanism for droplet formation, and for low values of the viscosity ratios and dissimilar widths w_c and w_d. Through LBM simulations, we aim to establish the dependence of the shear and surface tension forces for Capillary numbers that

define flows in the dripping to jetting regime and quantify the results in terms of the 'stable' droplet formation regime in a T-junction microchannel, which is yet to be understood.

In the current study, simulations have been carried out for a range of Capillary numbers given by $0.1 \leq Ca \leq 0.7$. At each Ca, the continuous phase flow rate was held constant while the dispersed phase flow rate was gradually increased. For $\lambda = 1/10$ and starting from a low value of the flow rate ratio Q, droplets were found to form at the entrance of dispersed channel through a dripping mechanism. As Q_d was increased, droplets were found to pinch-off downstream of the T-junction, forming a thread that became unstable after a distance from the dispersed channel entrance. For even higher flow rate Q_d, the protruding thread was found to be stable and filled up the whole length of the channel. The three flow patterns of DTJ, DC, and PF evolve respectively. For a fixed $\lambda = 1/10$, with an increase in flow rate ratio the droplet formation process (figure 59c,f) transforms to formation of a thread (figure 59b) and subsequently a stable jet (figure59a) or parallel flow (figure 59d,e). For the same geometry and viscosity ratio, the threshold value of flow ratio, $Q_{threshold}$, at which a stable parallel flow appears for the first time is found to decrease as the Capillary number increases. The presence of the parallel flow is marked by shedding of a few droplets (<5) before the jet fills the entire length of the main channel. A similar behavior at higher Capillary numbers corresponding to $Ca = 0.5$ and 0.7 is shown in figure 60, where the formation of a thread is observed to happen for $Q = 1/15$ and $Q = 1/20$ for $Ca = 0.5$ and 0.7 respectively, with a reduction in droplet size observable as well.

144
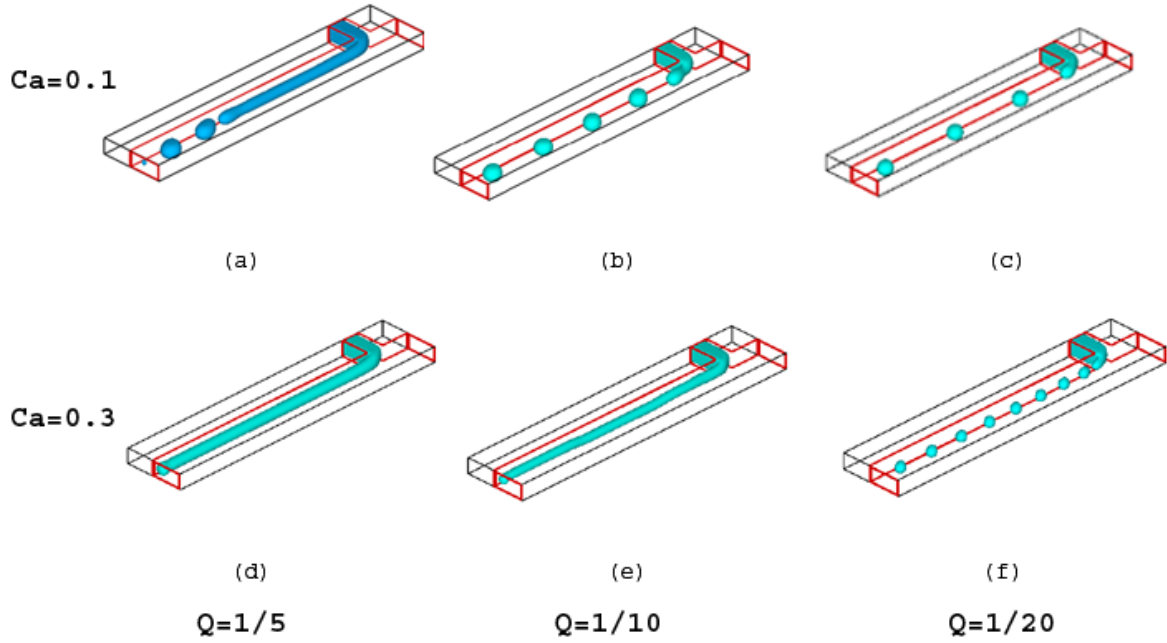
Figure 59: Regime map of droplet formation and flow pattern in the channel for two different capillary numbers and three different flow rate ratios at fixed $\lambda = 1/10$: (a) jetting, (b) droplet formation with necking or thread, (c and f) droplet formation, and (d and e) parallel flow.
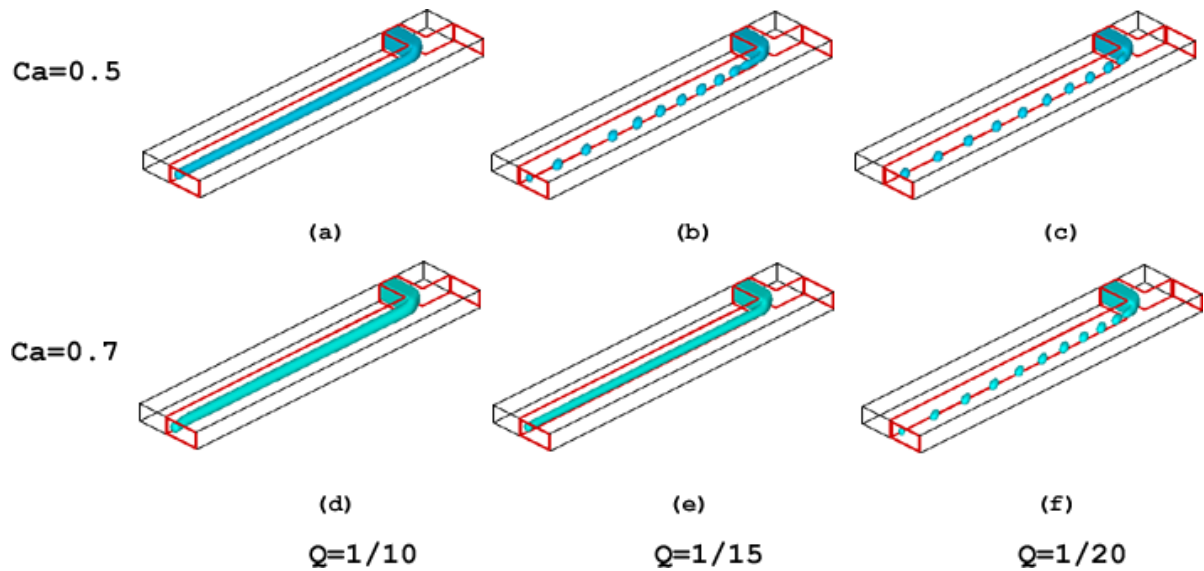
Figure 60: Regime map of droplet formation and flow pattern in the channel for higher Capillary numbers and three different flow rate ratios at fixed $\lambda = 1/10$.

The interplay of flow rate ratio and viscosity ratio is important in determining whether the flow regime is continuous or droplet-laden. When the continuous flow viscosity is increased, i.e., for a lower $\lambda = 1/30$, a slightly different trend emerges. For example, at Ca=0.5, the threshold value of flow rate ratio at which a jet becomes unstable is 1/10. For λ=1/10 for the same Capillary number, the threshold occurs at a lower Q_d, i.e., $Q_{threshold} = 1/20$. The transition from DC to DTJ is also influenced by the viscosities of the two fluids. For $\lambda = 1/30$, this transition to dripping occurs at $Q = 1/12$, whereas for $\lambda = 1/10$, the corresponding flow rate ratio is $Q = 1/24$. Similar to an earlier observation (Guillot and Colin (2005)), current results show that the viscosity ratio influences the width of the DC regime. With a decrease in λ, this zone is limited to $Q \in [1/11, 1/10]$ as compared to $Q \in [1/24, 1/19]$, indicating ~20% reduction in the flow rate of the continuous phase. In contrast, Guillot and Colin's (2005) experimental findings have been reported for $\lambda = 0.35$ and 0.07. The width of the transition zone DC was found to increase as the Capillary number was lowered till Ca=0.1 (figure 61). Results at an even lower Capillary number i.e., Ca=0.01, show that the width of the two extreme cases shown by the curves in figure 61 corresponds to $Q \in [1/2, 1]$. At higher Ca, the width of the DC regime decreases until after Ca~0.7, the DC regime ceases to exist.

Figure 62 shows the normalized droplet volume as a function of Capillary number for different flow rate ratios and at fixed $\lambda = 1/10$. At a fixed Ca, the flow rate ratio was varied by changing the dispersed phase velocity. The droplet volume was normalized using $V_0 = w_c^2 h$. A force analysis is used in the present study adapted from Christopher et al (2008), where pressure and

146
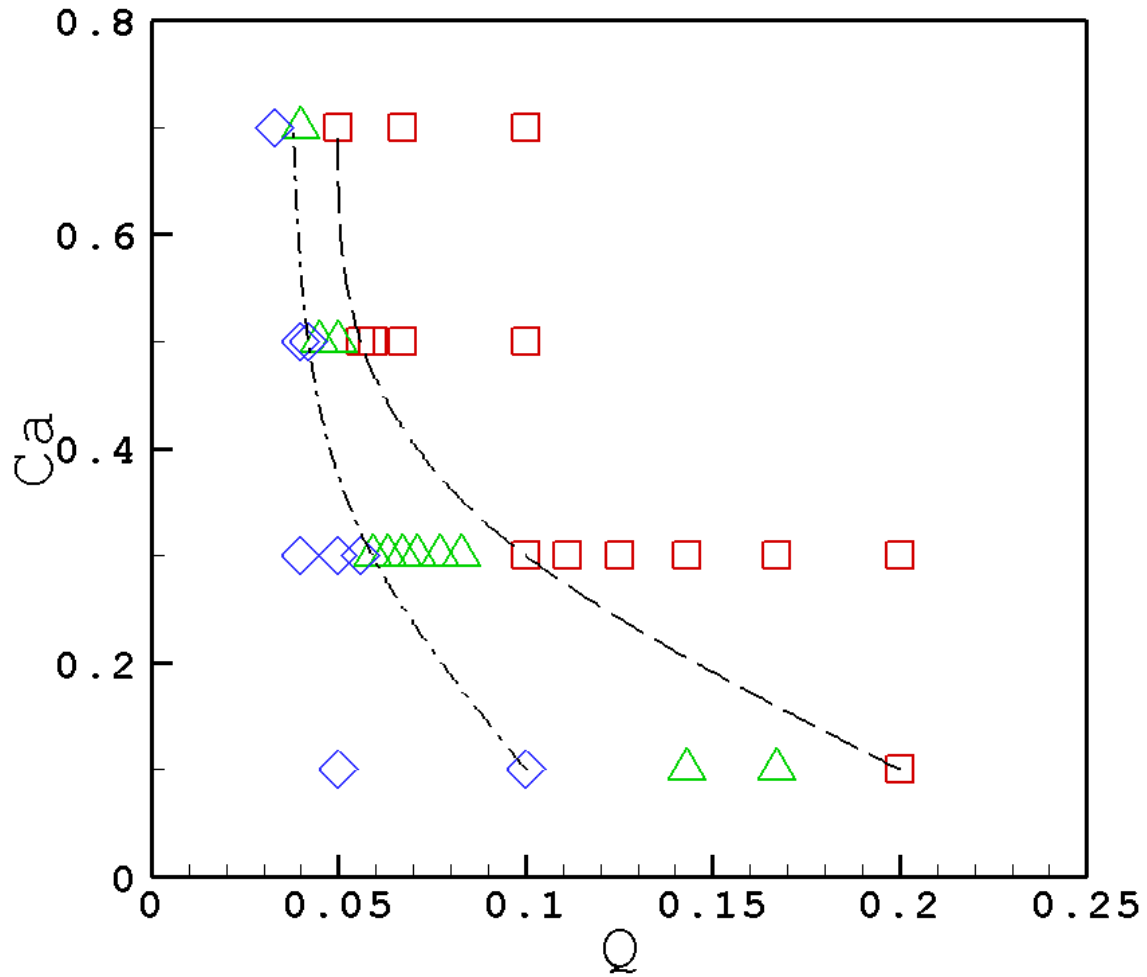
Figure 61: Droplet flow regimes as a function of flow rate ratio (Q) and capillary number (Ca) at viscosity ratio $\lambda = 1/10$. Symbols indicate (□): parallel flow, PF, (Δ): droplet formed in the main channel, DC, and (◊): droplet formed at the T-junction, DTJ. Data at different regimes are shown in different colors only for visual guidelines.
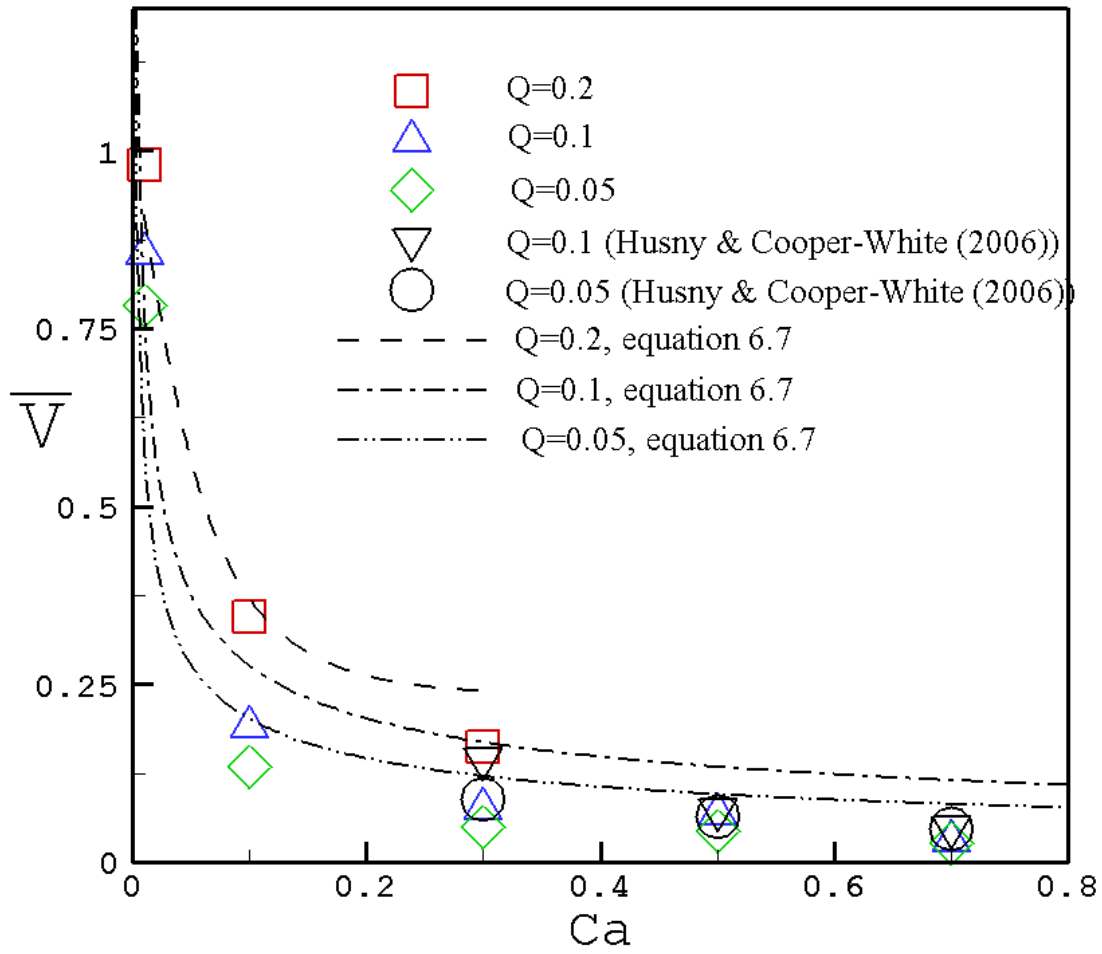
Figure 62: Normalized droplet volume as a function of capillary number for different flow rate ratios.

shear forces are assumed to be the same and the interfacial force is scaled down by a factor k, ($k<1$), such that $F_\sigma = k\sigma h$. This is to account for the case when the curvature in the depth direction is greater than $2/h$. On balancing the interfacial, shear and pressure forces, the modified form of the cubic polynomial for $\bar{b}(=b/w_c)$, where b is the length of the drop before it pinches, becomes $k(1-\bar{b})^3 = \bar{b}Ca$. Based on this, the volume of the droplet in the original work of Christopher was computed as

$$\bar{V} \approx \bar{b}^2 + \Lambda Q \tag{6.7}$$

A comparison of current results with their force analysis and a fourth order polynomial given by Husny and Cooper-White (2006) obtained at pinch off shows reasonable agreement in the order and dependence of droplet volume on Ca.

The droplet volume decreases as Ca is increased, as shown in figure 62. The non-dimensional volume decreases from 1.0 to nearly 0.2 from $Ca=0.01$ and 0.1. At Ca=0.5, the droplet volume for $Q = 0.05$, 0.1 and 0.2 is the same, reaching an asymptotic , beyond which the drop it seems to reach an asymptotic value of nearly 0.1 at Capillary numbers greater than 0.5. Carrying forward the same argument from section 6.4.2, the negligible change in the droplet volumes for $Ca \geq 0.5$ goes forward with the observation that the frequency does not change with flow rate ratio beyond a certain Capillary number, as shown in figure 58.

For the same Ca, the droplet volume was observed to increase with the flow ratio, a trend seen by Christopher et al (2008) and Husny and Cooper-White (2006). This is due to the reason that

the dispersed flow increases as the flow rate ratio is increased. Since the time to shear the droplet is inversely proportional to the continuous phase flow rate, any increase in Q does not increase the shear drag induced on the emerging dispersed phase. Hence, a higher volume of the dispersed phase is pushed into the main channel, and thus, forming a droplet with a higher volume as compared to those formed at lower flow rate ratios.

In order to determine the influence of continuous phase viscosity on droplet volume, simulation results were compared for a range of viscosity ratios at a fixed Ca=0.1 (figure 63). Different viscosity ratios of $\lambda = 1/30$, $1/50$ and $1/100$ were chosen by keeping the dispersed phase viscosity the same value as that used for $\lambda = 1/10$, and the continuous phase viscosity was increased. This results in a lower average velocity of the continuous phase, and hence a lower flow rate Q_c. For the same geometric variables w_c and w_d, Re_c decreased by factors of 1/9, 1/25 and 1/100 corresponding to $\lambda = 1/30$, $1/50$ and $1/100$, respectively, as compared to Re_c for $\lambda = 1/10$. In the shear dominated regime, the drag force due to viscous effects is dominant as compared to the pressure force due to blockage in the main channel. The drag force ($\mathbf{D}$) is $D \propto C_D U_c^2 A$, and can be written in terms of stress as $\tau_D \propto C_D U_c^2$. With an increase in the continuous phase viscosity, the increase in the drag coefficient (C_D) does not match the corresponding decrease in U_c^2, resulting in an induced shear drag that is lower as compared to that of a lower continuous phase viscosity fluid. Thus, a smaller drag force would act on the expanding droplet. This will enable the protuberant dispersed phase to expand in the main channel for a longer time before it is pinched off and hence an increase in droplet volume. This analysis agrees with current results shown in figure 63, where the normalized droplet volume is

shown to increase as the continuous phase viscosity increases (i.e. $\lambda \downarrow$). A power-law curve was fitted to the experimental data of Christopher et al (2008) for low Ca as $\bar{V} = QCa^{-0.3}/\bar{\beta}$, where $\bar{\beta}$ is a measure of the capillary breakup frequency. They reported $\bar{\beta}$ to be 1.13 for $\lambda = 1/50$. In figure 63, $\bar{\beta} = 1.37$ for the same viscosity ratio, and is 1.12 for $\lambda = 1/100$, where $\bar{\beta}$ was estimated from the slope of normalized volume vs. flow rate ratio. Thus, the droplet volume increases when the dispersed flow rate or the continuous flow viscosity increases.
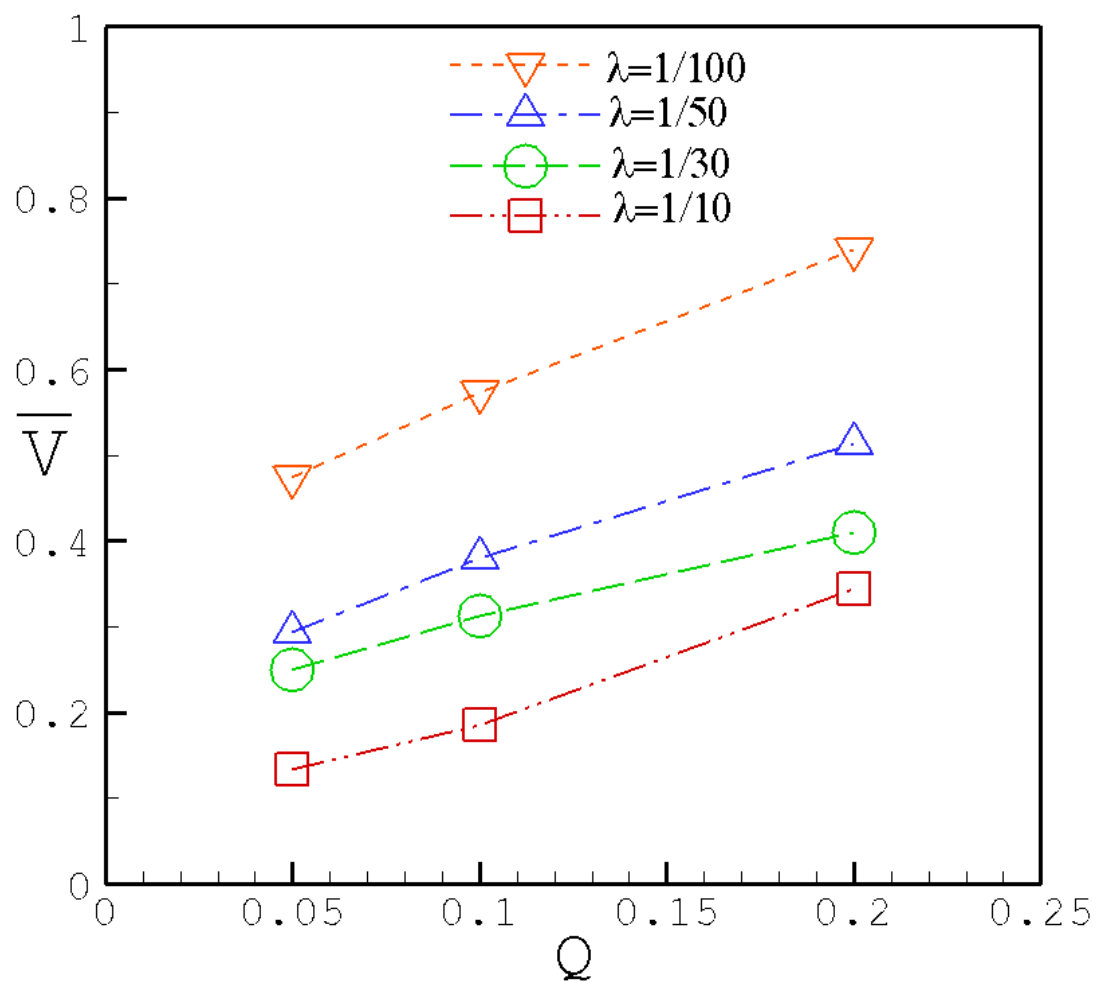
Figure 63: Normalized droplet volume as a function of the flow rate ratio Q for different viscosity ratios at Ca=0.1.

CHAPTER SEVEN: CONCLUSION

It is shown that the lattice Boltzmann method can be used to study fluid flows that occur in a variety of applications. These problems include ranging from internal combustion engines, spray cooling, ink-jet printing to microfluidic devices for food processing, drug delivery, microanalysis, tumor destruction, as ultrasound agents and in chemical reactions. In this work, through both single- and two-phase simulations, ranging from pressure-driven flow between parallel plates, two-phase flow of single and multiple bubbles rising under buoyancy in a periodic domain, droplet impingement and break-up on a smooth dry surface, and formation of dispersions in a microfluidic T-junction, the applicability and advantages of using LBM over conventional techniques is established.

The important non-dimensional parameters that describe the problem of two dissimilar liquids in a T-junction microchannel are: the flow rate ratio (Q), Capillary number (Ca), Reynolds number (Re), viscosity ratio (λ), width ratio (Λ) and the dimensionless depth of the channel (Γ). In the current work, the effect of varying these parameters is studied in the context of measuring and recording the droplet volumes and frequency for various flow conditions. The flow regimes emanating as a consequence of the combination of these parameters is also illustrated.

At low Capillary numbers ($Ca < 0.01$), it was found that 'plugs' of dispersed phase are formed, which occupy the whole width of the continuous phase channel. The length of these plugs was

153

found to be a strong function of the flow rate ratio of the two liquids. A higher flow rate ratio resulted in longer droplets, and the dependence follows a variation that can be best described to be linear. The formation of these plugs was also shown to be a consequence of the pressure build-up that occurs as the flow of the continuous liquid past the T-junction is slowed down due to a blockage created by the expanding discontinuous drop, as shown by the pressure fluctuations at a point upstream of the T-junction. Changing the width and height of the channels resulted in different shapes of droplets, which indicates that the geometry plays a role in the overall formation of these micron-sized droplets. Droplets formed in this regime are highly confined, and their lengths decrease slightly as the Capillary number increases.

For slightly higher Capillary numbers, a different trend emerges. The volume of the droplets decreases rapidly as Ca is increased. The pressure fluctuations present in the low Ca regime disappear, and the pressure upstream of the T-junction shows negligible variation as a function of time. The frequency of formation of droplets is found to increase significantly as Ca increases. The equivalent spherical diameter of a drop with the same volume as that of the droplets formed at the T-junction was found to obey a relationship given as $d_{sph}/w_c \sim Ca^{-\alpha}$, where the exponent α was found to be a function of the flow rate ratio, and lies between 0.2 and 0.25 for flow rate ratios corresponding to 1/5 and 1/20 respectively.

At even higher Capillary numbers, the dripping regime begins, in which the droplets are unconfined for a viscosity ratio of $\lambda = 1/10$ and low flow rate ratios. The effect of the continuous fluid viscosity and the geometry of the channel were investigated in the same context.

154

It was found that increasing the width of the continuous liquid channel, keeping the flow rate ratio constant, results in the formation of droplets that are confined and resemble truncated spheres, as opposed to spherical for lower widths, and the dispersed phase flow quickly transforms into a parallel jet for slightly lower values of the flow rate ratio. The frequency of formation was found to increase; although it could not be measured for flow rate ratios $Q > 1/10$ as a stable jet appeared. On the other hand, increasing the viscosity of the continuous liquid resulted in a behavior which was in contrast to that observed with the change in geometry. Increasing μ_c resulted in the formation of larger non-spherical droplets, and the droplet flow was stable for the range of flow rate ratios simulated. More so, an increase in the viscosity led to a decrease in the frequency of droplets. This was explained on the basis of a resident time for the penetrating dispersed phase, which is more when the surrounding viscosity is higher (as the flow rate Q_c is lower for the same Ca and higher viscosity). In addition, the frequency was found to increase as the flow rate of the continuous liquid was increased. The frequency was found to increase as the Capillary number was increased, although the increase in frequency with an increase in flow rate ratio was not appreciable for $Ca \geq 0.5$, which indicates that the volume of the droplets may not change beyond a certain critical Capillary number. This hypothesis was found to be consistent with volume measurements made for Capillary numbers as high as 0.7, and the change in the former was minimal beyond $Ca = 0.3$.

Finally, a regime map was created that listed the possible outcomes when two dissimilar liquids interact at a T-junction. These are classified as: droplet at the T-junction (DTJ), droplet in the channel (DC), and parallel flow (PF). Based on numerical simulations conducted at various

Capillary numbers, it was found that as the flow rate was increased, the flow transformed from droplet-laden to parallel flow. The transition from droplets formed at the T-junction to parallel flows was found to depend on the Capillary number of the continuous phase. As the Capillary number was increased, the transition occurred earlier for a fixed viscosity ratio, indicating that the width of the DC regime decreases with an increase in Ca. For higher viscosities of the continuous phase, the transition zone was found to become narrower. The volume of the droplets was a function of the viscosity ratio as well. As a result of a lower shear on the emerging discontinuous liquid into the main channel, the droplet volume increased when the dispersed flow rate or the continuous flow viscosity was increased.

CHAPTER EIGHT: FUTURE WORK

Droplet impingement on a dry surface is a problem that is commonly encountered for dissimilar fluids with large density contrast, such as water drops surrounded by air, or in internal combustion engines, where micron-sized droplets of the fuel are released into the combustion chamber. Lattice Boltzmann modeling of such class of problems is not possible with the multiphase model adopted in the current work. Thus, future work could be directed towards the droplet break-up mechanism in three-dimensions using a model that can simulate high Reynolds and Weber numbers. Another problem that can be investigated using a similar methodology includes the study of the splashing behavior of drops falling onto wet surfaces for high density ratio fluids.

In microfluidic devices, such as the one pursued in the current work, the role of the continuous liquid viscosity on the squeezing regime needs to be examined in greater detail, as it is not clear when the viscous forces begin to play a prominent role in determining the formation of plus or droplets. In addition, significant modeling is required to predict a universal rule that could predict the length of droplets formed for flows at very low Capillary numbers. As is evident, the empirical correlation proposed by Garstecki et al (2006) is valid only for flow geometries where $w_d / w_c \geq 1/2$, and also involves an empirical parameter whose value is unknown and must depend on the physical properties of the fluids, geometry of the device or viscosity ratio chosen. A mechanistic model needs to be developed which would be based on the interfacial physics of the two liquids involved, and could help in predicting the performance and output of such

microfluidic devices. The model has to be such that it does not rely on empirical correlations whose applicability may become questionable. In addition, the effect of liquid viscosities on the stability of droplet formation needs to be investigated further for flows that fall under the dripping regime. A regime map could be developed, similar to the one obtained in the current study, which could predict the stability of flows for a range of Capillary numbers and flow rate ratios. Finally, the role of viscosity on the width of the transition regime should be studied. Moreover, the viscosity of the continuous liquid may influence the critical capillary number where the transition region begins. Future work can be directed towards modification of the multiphase model to account for the effect of surfactants on the droplet formation mechanism.

A major challenge with the current model of LBM that has been used in this work is its inability in handling fluid mixtures which have very high density contrast (like an air-water system in which density ratios are of the order of 1000). Recently, a new variant of the model used in this work has been proposed by Lishchuk et al (2008), and could be implemented to study the formation of vapor bubbles in microfluidic devices.

LIST OF REFERENCES

Anderson D.M., McFadden G.B. and Wheeler A.A., "Diffuse-interface methods in fluid mechanics", Ann. Rev. Fluid Mech. 30, 139-165 (1998)

Anna S.L., Bontouz N. and Stone H.A., "Formation of dispersions using 'flow focusing' in microchannels", Appl. Phys. Lett. 82 (3), 364-366 (2003)

Anna S.L. and Mayer H.C., "Microscale tipstreaming in a microfluidic flow focusing device", Phys. Fluids 18, 121512 (2006)

Asai A., Makoto S., Hirasawa S. and Okazaki T., "Impact of an ink drop on paper", J. Imag. Sci. Tech. 37, 205-207 (1993)

Bhaga D. and Weber M.E., "Bubbles in viscous liquids" shapes, wakes and velocities", J. Fluid Mech. 105, 61-85 (1981)

Bhatnagar P., Gross E. and Krook M., "A model for collisional process in gases 1: Small Amplitude processes in charged and neutral one-component system", Phys. Rev. 94, 511-525 (1954)

Buckingham E., "Physically similar systems: Illustrations of the use of dimensional equations", Phys. Rev. 4, 345-376 (1914)

Buick J.M. and Greated C.A., "Gravity in a lattice Boltzmann model", Phys. Rev. E 61, 5307-5320 (2000)

Chandra S. and Avedisian C.T., "On the collision of a droplet with a solid surface", Proc. R. Soc. Lond. A 432, 13-41 (1991)

Chang H-C., "Bubble/Drop Transport in Microchannels", in The MEMS Handbook, ed. Gad-el-Hak M., CRC Press, Boca Raton (2002)

Chen S. and Doolen G.D., "Lattice Boltzmann method for fluid flows", Ann. Rev. Fluid Mech. 30, 329-364, (1998)

Chen S., Martinez D. and Mei R., "On boundary conditions in lattice Boltzmann methods", Phys. Fluids 8, 2527-2536 (1996)

Christopher G.F. and Anna S.L., "Microfluidic methods for generating droplet streams", J. Phys. D: Appl. Phys. 40, R319-R336 (2007)

Christopher G.F., Noharuddin N.N., Taylor J.A. and Anna S.L., "Experimental observations of the squeezing-to-dripping transition in T-shaped microfluidic junctions", Phys. Rev. E 78, 036317 (2008)

Cornubert R.,d'Humies D. and Levermore D., "A Knudsen layer theory for lattice gases", Proc. NATO Adv. Res. Workshop on Lattice Gas Methods for PDE's, 241-259 (1991)

Cramer C., Fischer P. and Windhab E.J., "Drop formation in a co-flowing ambient fluid", Chem. Engg. Sci. 59, 3045-3058 (2004)

Cristini V. and Tan Y-C., "Theory and numerical simulation of droplet dynamics in complex flows-a review", Lab Chip 4, 257-264 (2004)

Cristobal G., Benoit J-P., Joanicot M. and Ajdari A., "Microfluidic bypass for efficient regulation of droplet traffic at a junction", Appl. Phys. Lett. 89, 034104 (2006)

de Menech M., "Modeling of droplet breakup in a microfluidic T-shaped junction with a phase-field model", Phys. Rev. E 73, 031505 (2006)

de Menech M., Garstecki P., Jousse F. and Stone H.A., "Transition from squeezing to dripping in a microfluidic T-shaped junction", J. Fluid Mech. 595, 141-161 (2008)

Dupin M.M., Halliday I. and Care C.M., "Simulation of a microfluidic flow-focusing device", Phys. Rev. E 73, 055701 (2006)

Engl W., Roche M., Colin A. and Panizza P., "Droplet traffic at a simple junction at low Capillary numbers", Phys. Rev. Lett. 95, 208304 (2005)

Esmaeeli A. and Tryggvason G., "Direct numerical simulations of bubbly flows. Part 1. Low Reynolds number arrays", J. Fluid Mech. 377, 313-345 (1998)

Esmaeeli A. and Tryggvason G., "Direct numerical simulations of bubbly flows. Part 2. Moderate Reynolds number arrays", J. Fluid Mech. 385, 325-358 (1999)

Fan L-S. and Tsuchiya K., "Bubble wake dynamics in liquids and liquid-solid suspensions", Butterworth-Heinemann, Stoneham, MA (1990)

Gad el Hak M., "The MEMS Handbook", CRC Press, Boca Raton (2002)

Garstecki P., Gitlin I., DiLuzio W., Whitesides G.M., Kumacheva E. and Stone H.A., "Formation of monodisperse bubbles in a microfluidic flow-focusing device", Appl. Phys. Lett. 85, 2649-2651 (2004)

Garstecki P., Fuerstman M.J., Stone H.A. and Whitesides G.M., "Formation of droplets and bubbles in a microfluidic T-junction—scaling and mechanism of break-up", Lab Chip, 6, 437-446 (2006)

Ginzbourg I. and Adler P.M., "Boundary flow condition analysis for the three-dimensional lattice Boltzmann model", J. Physics II 4, 191-214 (1994)

Grace J.R., "Shapes and velocities of bubbles rising in infinite liquids", Trans. Inst. Chem. Engg. 51, 116-120 (1973)

Grunau D., Chen S. and Eggert K., "A Lattice Boltzmann Model for Multiphase Fluid Flows", Phys. Fluids A 5, 2557-2562 (1993)

Guillot P. and Colin A., "Stability of parallel flows in a microchannel after a T-junction", Phys. Rev. E 72, 066301 (2005)

Guillot P., Colin A., Utata A.S. and Ajdari A., "Stability of a jet in confined pressure-driven biphasic flows at low Reynolds numbers", Phys. Rev. Lett. 99, 104502 (2007)

Gupta A., "Lattice Boltzmann Simulation to study single and multi bubble dynamics", M.S. Thesis (2007)

Gupta A. and Kumar R., "Lattice Boltzmann simulation to study multiple bubble dynamics", Int. J. Heat Mass Trans. 51, 5192-5203 (2008)

Hamouda T., Hayes M.M., Cao Z., Tonda R., Johnson K., Wright D.C., Brisker J., and Baker Jr. J.R., "A Novel Surfactant Nanoemulsion with Broad-Spectrum Sporicidal Activity against Bacillus species", J. Infect. Dis. 180, 1939-1949 (1999)

Harvie D.J.E., Davidson M.R., Cooper-White J.J. and Rudman M., "A parametric study of droplet deformation through a microfluidic contraction: low viscositu Newtonian droplets", Chem. Engg. Sci. 61, 5149-5158 (2006)

He X. and Luo L.S., "Lattice Boltzmann model for the incompressible Navier-Stokes equation", J. Stat. Phys. 88, 927-944 (1997)

Higuera F. and Jiminez J., "Boltzmann approach to lattice gas simulations", Europhys. Lett. 9, 663-668 (1989)

Hou S., Shan X., Zou Q., Doolen G.D. and Soll W.E., "Evaluation of two lattice Boltzmann models for multiphase flows", J. Comp. Phys. 138, 695-713 (1997)

Huang S-H., Tan W-H., Tseng F-G. and Takeuchi S., "A monolithically three-dimensional flow-focusing device for formation of single/double emulsions in closed/open microfluidic systems", J. Micromech. Microengg. 16, 2336-2344 (2006)

Huh D., Tung Y.C., Wei H.H., Grotberg J.B., Skerlos S.J., Kurabayashi K. and Takayama S., "Use of air-liquid two-phase flow in hydrophobic microfluidic channels for disposable flow cytometers", Biomed. Microdevices 4, 141-149 (2002)

Husny J. and Cooper-White J.J., "The effect of elasticity on drop creation in T-shaped microchannels", J. Non-Newtonian Fluid Mech. 137, 121-136 (2006)

Inamuro T, Yoshino M. and Ogino F., "A non-slip boundary condition for lattice Boltzmann simulations", Phys. Fluids 7, 2928-2930 (1995)

Inamuro T., Ogata T. and Ogino F., "Numerical simulation of bubble flows by the lattice Boltzmann method", Fut. Gen. Comp. Sys., 20, 959-964 (2004a)

Inamuro T., Ogata T., Tajima S. and Konishi N., "A lattice Boltzmann method for incompressible two-phase flows with large density differences", J. Comp. Phys. 198, 628-644 (2004b)

Inamuro T., Tajima S. and Ogino F., "Lattice Boltzmann simulation of droplet collision dynamics", Int. J. Heat Mass Trans., 47, 4649-4657 (2004c)

Jensen M.J., Stone H.A. and Bruus H., "A numerical study of two-phase Stokes flow in an axisymmetric flow-focusing device", Phys. Fluids 18, 077103 (2006)

Joanicot M. and Ajdari A., "Droplet control for microfluidics", Science 309, 887-888 (2005)

163

Joseph D.D., "Rise velocity of a spherical cap bubble", J. Fluid Mech. 488, 213-223 (2003)

Josserand C. and Zaleski S., "Droplet splashing on a thin liquid film", Phys. Fluids 15, 1650-1657 (2003)

Kandlikar S.G., "Fundamental issues related to flow boiling in minichannels and microchannels" Exp. Thermal Fluid Sci. 26, 389-407 (2002)

Kataoka D.E. and Troian S.M., "Patterning liquid flow on the microscopic scale", Nature 402, 794-797 (1999)

Kumar R., "Two-phase flow microstructures in thin geometries: Multi-field modeling", Heat and Fluid Flow in Microscale and Nanoscale Structures, Faghri M. and Sunden B. (eds.), WIT Press, Boston, 173-224 (2004)

Kurtoglo I.O. and Lin C.L. "Lattice Boltzmann study of bubble dynamics", Num. Heat Trans. B 50, 333-351 (2006)

Latva-Kokko M. and Rothman D.H., "Diffusion properties of gradient-based lattice Boltzmann models of immiscible fluids", Phys. Rev. E 71, 056702 (2005)

Lavallée P, Boon J.P. and Noullez A., "Boundaries in lattice gas flows", Physica D 47, 233-240 (1991)

Lee T. and Lin C-L., "A stable discretization of the lattice Boltzmann equation for simulation of incompressible two-phase flows at high density ratio", J. Comp. Phys. 206, 16-47 (2005)

Link D.R., Anna S.L., Weitz D.A. and Stone H.A., "Geometrically mediated breakup of drops in microfluidic devices", Phys. Rev. Lett. 92(5), 054503 (2004)

Lishchuk S.V., Care C.M. and Halliday I., "Lattice Boltzmann algorithm for surface tension with greatly reduced microcurrents", Phys. Rev. E 67, 036701 (2003)

Lishchuk S.V., Halliday I. and Care C.M., "Multicomponent lattice Boltzmann method for fluids with a density contrast", Phys. Rev. E 77, 036702 (2008)

Madou M., "Fundamentals of Microfabrication", CRC Press, Boca Raton, Florida (1997)

Maier R.S., Bernard R.S. and Grunau D.W., "Boundary conditions for the lattice Boltzmann method", Phys. Fluids 8, 1788-1801 (1996)

Martys N.S. and Chen H., "Simulation of Multicomponent Fluids in complex three-dimensional geometries by the Lattice Boltzmann Method", Phys. Rev. E. 53, 743-750 (1996)

Mei R., Luo L.S. and Shyy W., "An accurate curved boundary treatment in the lattice Boltzmann method", J. Comp. Phys. 155, 307-330 (1999)

Mei R., Shyy W., Yu D. and Luo L.S., "Lattice Boltzmann method for 3-D flows with curved boundaries", J. Comp. Phys. 161, 680-699 (2000)

Morton D., Rudman M. and Jong-Leng L., "An investigation of the flow regimes resulting from splashing drops", Phys. Fluids 12, 747-763 (2000)

Mukherjee S. and Abraham J., "Lattice Boltzmann simulations of two-phase flow with high density ratio in axially symmetric geometry", Phys. Rev. E 75, 026701 (2007a)

Mukherjee S. and Abraham J., "Crown behavior in drop impact on wet walls", Phys. Fluids 19, 052103 (2007b)

Mukherjee S. and Abraham J., "Investigations of drop impact on dry walls with a lattice-Boltzmann model", J. Coll. Inter. Sci. 312, 341-354 (2007c)

Mundo C., Sommerfeld M. and Tropea C., "Droplet-wall collisions: experimental studies of the deformation and breakup process", Int. J. Multiphase Flow 21, 151-173 (1995)

Murshed S.M.S., Tan S.H. and Nguyen N.T., "Temperature dependence of interfacial properties and viscosity of nanofluids for droplet-based microfluidics", J. Phys. D: Appl. Phys. 41, 085502 (2008)

Murshed S.M.S., Tan S.H., Nguyen N.T., Wong T.N. and Yobas L., "Microdroplet formation of water and nanofluids in heat-induced microfluidic T-junction", Microfluid Nanofluid 6, 253-259 (2009)

Naik N., Courcimault C., Hunter H., Berg J., Lee J., Naeli K., Wright T., Allen M., Brand O., Glezer A. and King W., "Microfluidics for generation and characterization of liquid and gaseous micro- and nanojets", Sens. Actuators 134, 119-127 (2007)

Nie Z., Seo M.S., Xu S., Lewis P.C., Mok M., Kumacheva E., Whitesides G.M., Garstecki P. and Stone H.A., "Emulsification in a microfluidic flow-focusing device: effect of the viscosities of the liquids", Microfluid Nanofluid 5, 585-594 (2008)

Noble D.R., Chen S., Georgiadis J.G. and Buckius R.O., "A consistent hydrodynamic boundary condition for the lattice Boltzmann method", Phys. Fluids 7, 203-209 (1995)

Okushima S., Nisisako T., Torii T. and Higuchi T., "Controlled production of monodisperse double emulsions by two-step droplet breakup in microfluidic devices", Langmuir 20, 9905-9908 (2004)

Pasandideh-Fard M., Qiao Y.M., Chandra S. and Mostaghimi J., "Capillary effects during droplet impact on a solid surface", Phys. Fluids 8, 650-659 (1996)

Ramsey J.M., Alarie J.P., Jacobson S.C. and Peterson N.J., "Molecular transport through nanometer confined channels" in: Micro Total Analysis, eds. Baba Y., Shoji S., van der Berg A., 1, 314-216, Dordrecht, Kluwer (2002)

Rioboo R., Marengo M. and Tropea C., "Time evolution of liquid drop impact onto solid, dry surfaces", Expts. Fluids 33, 112-124 (2002)

Rothman D.H. and Keller J.M., "Immiscible cellular-automaton fluids", J. Stat. Phys. 52, 1119-1127 (1988)

Sanakaranarayanan K., Shan X., Kevrekidis I.G. and Sundaresan S., "Analysis of drag and virtual mass forces in bubbly suspensions using an implicit formulation of the lattice Boltzmann method", J. Fluid Mech. 452, 61-96 (2002)

Scheller B.L. and Bousfield D.W., "Newtonian drop impact with a solid surface", AIChE J. 41, 1357-1367 (1995)

Shan X. and Chen H., "Lattice Boltzmann Model for simulating flows with multiple phases and components", Phys. Rev. E. 47, 1815-1819 (1993)

Skordos P.A., "Initial and boundary conditions for the lattice Boltzmann method", Phys. Rev. E 48, 4823-4842 (1993)

Smith G.D., http://www.mse.utah.edu/~gdsmith/tutorials/tutorial1.ppt (1999)

Song H., Tice J.D. and Ismagilov R.F., "A microfluidic system for controlling reaction networks in time", Angew. Chem. Int. 42(7), 768-772(2003)

Stone H.A., Stroock A.D. and Ajdari A., "Engineering Flows in Small Devices: Microfluidics toward a Lab-on-a-Chip", Ann. Rev. Fluid Mech. 36, 381-411 (2004)

Stow C.D. and Hadfield M.G., "An experimental investigation of fluid flow resulting from the impact of a water drop with an unyielding dry surface", Proc. R. Soc. Lond. A 373, 419-441 (1981)

Sugiura S., Nakajima M., Iwamoto S. and Seki M., "Interfacial tension driven monodispersed droplet formation from microfabricated channel array", Langmuir 17, 5562-5566 (2001)

Suryo R. and Basaran O.A., "Tip streaming from a liquid drop forming from a tube in a co-flowing outer fluid", Phys. Fluids 18, 082102 (2006)

Swift M., Orlandini S., Osborn W. and Yeomans J., "Lattice Boltzmann simulations of liquid-gas and binary fluid systems", Phys. Rev. E. 54, 5041-5052 (1996)

Takada M., Misawa M., Tomiyama A. and Hosokawa S., "Simulation of bubble motion under gravity by lattice Boltzmann method", J. Nuc. Sci. Tech., 38, 330-341 (2001)

Takeuchi S., Garstecki P., Weibel D.B. and Whitesides G.M., "An axisymmetric flow-focusing microfluidic device", Adv. Mater. 17, 1067-1072 (2005)

Thorsen T., Roberts R.W., Arnold F.H. and Quake S.R., "Dynamic pattern formation in a vesicle-generating microfluidic device", Phys. Rev. Lett. 86(18), 4163-4166 (2001)

Tice J.D., Lyon A.D. and Ismagilov R.F., "Effects of viscosity on droplet formation and mixing in microfluidic channels", Anal. Chim. Acta 507, 73-77 (2004)

Tomiyama A., "Struggle with Computational Bubble Dynamics", Proc. Int. Conf. on Multiphase Flow, ICMF'98, Lyon, June 8-12, 1-18 (1998)

Trimmer W.S.N., "Microrobots and Micromechanical Systems", Sensors Actuators, 19(3), 267-287 (1989)

Trimmer W.S.N. and Stroud R.H., "Scaling of Micromechanical Devices", in The MEMS Handbook, ed. Gad-el-Hak M., CRC Press, Boca Raton (2002)

Umbanhowar P.B., Prasad V. and Weitz D.A., "Monodisperse emulsion generation via drop break off in a coflowing stream", Langmuir 16, 347-351 (2000)

Van der Graaf S., Nisisako T., Schroën C.G.P.H., van der Sman R.G.M. and Boom R.M., "Lattice Boltzmann simulations of droplet formation in a T-shaped microchannel", Langmuir, 22, 4144-4152 (2006)

Wachters L.H.J. and Westerling N.A.J., " The heat transfer from a hot wall to impinging water drops in the spheroidal state", Chem. Eng. Sci. 21, 1047-1056 (1966)

Ward T. and Humsy G.M., "Electrodynamically driven chaotic mixing in a translating drop", Phys. Fluids 13, 3521-3525 (2001)

Wolfram S., "Cellular automaton fluids 1: Basic theory", J. Stat. Phys. 45, 471-526 (1986)

Wu L., Tsutahara M., Kim L.S. and Ha M.Y., "Three-dimensional lattice Boltzmann simulations of droplet formation in a cross-junction microchannel", Int. J. Multiphase Flow 34, 852-864 (2008)

Xu J.H., Li S.W., Chen G.G and Luo G.S., "Formation of monodisperse microbubbles in a microfluidic device", AIChE J. 52, 2254-2259 (2006a)

Xu J.H., Li S.W., Tan J., Wang Y.J. and Luo G.S., "Preparation of highly monodisperse droplet in a T-junction microfluidic device", AIChE J. 52, 3005-3010 (2006b)

Xu J.H., Li S.W., Tan J. and Luo G.S., "Correlations of droplet formation in T-junction microfluidic devices: from squeezing to dripping", Microfluid Nanofluid 5, 711-717 (2008)

Yang Z.L., Dinh T.N., Nourgaliev R.R. and Sehgal B.R., "Numerical investigation of bubble growth and detachment by the lattice Boltzmann method", Int. J. Heat Mass Trans. 44, 195-206 (2001)

Yarin A.L., "Drop impact dynamics: splashing, spreading, receding, bouncing …", Ann. Rev. Fluid Mech. 38, 159-192(2006)

Yarin A.L. and Weiss D.A., "Impact of drops on solid surfaces: self-similar capillary waves, and splashing as a new type of kinematic discontinuity", J. Fluid Mech. 283, 141-173 (1995)

Yobas L., Martens S., Ong W-L. and Ranganathan N., "High performance flow-focusing geometry for spontaneous generation of monodispersed droplets", Lab Chip 6, 1073-1079 (2006)

Yu Z., Hemminger O. and Fan L-S., "Experiment and lattice Boltzmann simulation of two-phase gas-liquid flows in microchannels", Chem. Engg. Sci. 62, 7172-7183 (2007)

Yuan P. and Schaefer L., "Equations of state in a lattice Boltzmann model", Phys. Fluids, 18, 042101 (2006)

Zhang D.F. and Stone H.A., "Drop formation in viscous flows at a vertical capillary tube", Phys. Fluids 9, 2234-2242 (1997)

Zhou C., Yue P. and Feng J.J., "Formation of simple and compound drops in microfluidic devices", Phys. Fluids 18, 092105 (2006)

Ziegler D.P., "Boundary conditions for the lattice Boltzmann simulations", J. Stat. Phys. 71, 1171-1177 (1993)

Zou Q. and He X., "On pressure and velocity boundary conditions for the lattice Boltzmann BGK model", Phys. Fluids 9, 1591-1598 (1997)